National Library of Canada
Bibliothèque nationale du Canada

Canadian Theses Service
Service des thèses canadiennes

Ottawa, Canada
K1A 0N4

NOTICE

The quality of this microform is heavily dependent upon the quality of the original thesis submitted for microfilming. Every effort has been made to ensure the highest quality of reproduction possible.

If pages are missing, contact the university which granted the degree.

Some pages may have indistinct print especially if the original pages were typed with a poor typewriter ribbon or if the university sent us an inferior photocopy.

Reproduction in full or in part of this microform is governed by the Canadian Copyright Act, R.S.C. 1970, c. C-30, and subsequent amendments.

AVIS

La qualité de cette microforme dépend grandement de la qualité de la thèse soumise au microfilmage. Nous avons tout fait pour assurer une qualité supérieure de reproduction.

S'il manque des pages, veuillez communiquer avec l'université qui a conféré le grade.

La qualité d'impression de certaines pages peut laisser à désirer, surtout si les pages originales ont été dactylographiées à l'aide d'un ruban usé ou si l'université nous a fait parvenir une photocopie de qualité inférieure.

La reproduction, même partielle, de cette microforme est soumise à la Loi canadienne sur le droit d'auteur, SRC 1970, c. C-30, et ses amendements subséquents.

NL-339 (r. 88/04) c

Canada

UNIVERSITY OF ALBERTA

Geostrophic Scatter Diagrams and the Application of Free Mode Theory to a Northeast Pacific Blocking Episode

BY

Nils Robert Ek

A THESIS SUBMITTED TO THE FACULTY OF GRADUATE STUDIES AND RESEARCH IN PARTIAL FULFILLMENT OF THE REQUIREMENTS FOR THE DEGREE OF MASTER OF SCIENCE

IN

METEOROLOGY

DEPARTMENT OF GEOGRAPHY

EDMONTON, ALBERTA

SPRING 1992

National Library of Canada
Bibliothèque nationale du Canada

Canadian Theses Service
Service des thèses canadiennes

Ottawa, Canada
K1A 0N4

The author has granted an irrevocable non-exclusive licence allowing the National Library of Canada to reproduce, loan, distribute or sell copies of his/her thesis by any means and in any form or format, making this thesis available to interested persons.

L'auteur a accordé une licence irrévocable et non exclusive permettant à la Bibliothèque nationale du Canada de reproduire, prêter, distribuer ou vendre des copies de sa thèse de quelque manière et sous quelque forme que ce soit pour mettre des exemplaires de cette thèse à la disposition des personnes intéressées.

The author retains ownership of the copyright in his/her thesis. Neither the thesis nor substantial extracts from it may be printed or otherwise reproduced without his/her permission.

L'auteur conserve la propriété du droit d'auteur qui protège sa thèse. Ni la thèse ni des extraits substantiels de celle-ci ne doivent être imprimés ou autrement reproduits sans son autorisation.

ISBN 0-315-73251-2

Canada

UNIVERSITY OF ALBERTA

RELEASE FORM

NAME OF AUTHOR Nils Robert Ek

TITLE OF THESIS Geostrophic Scatter Diagrams and the Application of Free Mode Theory to a Northeast Pacific Blocking Episode

DEGREE Master of Science in Meteorology

YEAR THIS DEGREE GRANTED 1992

Permission is hereby granted to the University of Alberta Library to reproduce single copies of this thesis and to lend or sell such copies for private, scholarly or scientific research purposes only.

The author reserves all other publication and other rights in association with the copyright in the thesis, and except as hereinbefore provided neither the thesis nor any substantial portion thereof may be printed or otherwise reproduced in any material form whatever without the author's prior written permission.

Nils Robert Ek

6203 - 140 Avenue,
Edmonton, Alberta
T5A 1G7

March 2, 1992

Date

UNIVERSITY OF ALBERTA

FACULTY OF GRADUATE STUDIES AND RESEARCH

The undersigned certify that they have read, and recommend to the Faculty of Graduate Studies and Research for acceptance, a thesis entitled Geostrophic Scatter Diagrams and the Application of Free Mode Theory to a Northeast Pacific Blocking Episode, submitted by Nils Robert Ek in partial fulfillment of the requirements for the degree of Master of Science in Meteorology.

G.E. Swaters

R.B. Charlton

J.D. Wilson

March 2 1992

Date

Abstract

A time series of scatter-diagrams of 500 mb geostrophic stream-function, ψ, versus quasi-geostrophic potential vorticity, q, is derived during an episode of Northeast Pacific blocking in January and February 1989. The use of the diagrams as a diagnostic tool together with conventional isobaric charts has been previously employed for Northeast Atlantic blocking. This is the first known application of this technique to a Northeast Pacific block.

Visual inspection of the diagrams suggests that blocking can be modelled by localized free mode solutions of the governing equations, characterized by potential vorticity and stream-function of the form $q = q(\psi)$. Our diagrams show a roughly linear $q(\psi)$ relationship that is particularly well-correlated during stages of the block in which the vorticity contours are closed, or nearly closed.

We are able to *quantitatively* detect free mode tendencies of this block using an equation that relates the area of scatter plots to the departure of a stationary system from any free-mode of the quasi-geostrophic equations. The $q(\psi)$ plot area is equivalent to the net geostrophic vorticity flux across the boundary of the blocking region. We have computed both these quantities, and our results are in very good agreement with the theory.

We suggest that the block approaches two different free modes during its lifetime. The first stage is an Omega-block, which persists during the first two weeks of February 1989. During the second stage, between February 18-22, the 500 mb stream-function displays a dipolar form, and the scatter plots are quite similar to $q(\psi)$ plots for a geostationary, equivalent barotropic modon in a westerly flow. We examine the applicability of the modon free mode in modelling the block by using the slopes of least-squares-fit $q(\psi)$ lines to formally compute a modon radius. This is found to correspond reasonably to the actual block dimensions, for the period in which the block has a dipolar structure. A comparison of the theoretical and observed spacing of the potential vorticity extrema is inconclusive. These tests are quite sensitive to the degree of vertical static stability; the modon existence condition is not satisified if the static stability is too high. An application of Arnol'd's theorem suggests that a sufficient condition for Liapunov stability is more likely to be satisfied by the Omega-block, than by the dipole form of the block. This may help to explain why the Omega-block lasts longer than the dipole block.

The initial formation of the block coincides with the emergence of an intense synoptic-scale cyclonic disturbance over North America. This feature is clearly distinguished by a strong increase in the $q(\psi)$ plot area, and by a steepening of the scatter plots. The latter effect has also been observed before the onset of blocking over the North Atlantic, and is consistent with the idea that blocking appears to be preceded by intense synoptic-scale activity, in which non-linear forcing of the planetary-scale flow, by synoptic-scale systems, leads to rapid block formation. We

suggest that the time series of $q(\psi)$ plot area, together with the scatter plots, may be useful in identifying such synoptic-scale disturbances in advance.

Within the quasi-geostrophic framework, we model the block as a superposition of a stationary blocking eddy and a zonal flow having no meridional shear. A separation of variables leads to the equivalent barotropic modon solution, and a vertical structure equation. The latter is solved analytically through the use of a power law for the tropospheric static stability, yielding a set of vertical normal modes. We use the first four modes to examine the evolution of the baroclinicity of the block. We find that the 'blocking eddy' component of the stream-function is dominated by the gravest mode. The dipole form of the block appears to have the same degree of barotropicity as the Omega-block. A small but abrupt increase in baroclinicity immediately prior to the formation of the dipole could be evidence of the so-called eddy-straining mechanism, in which synoptic-scale eddies can generate a dipole block.

Acknowledgements

I would like to thank my co-supervisors, Dr. R.B. Charlton and Dr. Gordon Swaters, for their assistance, as well as Dr. J.D. Wilson for serving on my examining committee. The many intense and fruitful discussions with Dr. Swaters are particularly appreciated. I also wish to thank Dr. E.P. Lozowski for reading an earlier version of this thesis and making numerous helpful comments and suggestions. The cooperation of the Canadian Meteorological Centre in supplying several magnetic tapes of data is gratefully acknowledged. I also wish to express my thanks to Dan Hemenway of the University of Alberta Geography Department, who assisted me in learning to use the graphics software and other computer facilities.

The support of my family during the course of this work has been a tremendous help and comfort.

This thesis and the work described therein were completed while I was on educational leave from the Atmospheric Environment Service.

N.R.E.

Contents

Abstract iv

Acknowledgements vi

List of Figures ix

List of Symbols x

Introduction **1**

Theoretical Background **8**

2.1 Regional blocking theories 8

2.2 Baroclinic modon solutions to the quasi-geostrophic equations ... 11

2.2.1 Steadily-travelling equivalent barotropic modon solution 11

2.2.2 Derivation of the governing baroclinic equations 14

2.2.3 Geostationary modon embedded in a stratified zonal flow 19

2.3 The solution to the vertical structure problem 29

2.4 Scatter diagrams 36

2.5 Slope and area of the $q(\psi)$ plot 37

Computations **40**

3.1 Data Preparation 40

3.2 Calculation of stream-function and vorticity 40

3.3 Smoothing 45

3.4 Least-squares $q(\psi)$ lines 47

3.5 Vorticity flux and the area of the $q(\psi)$ plots 48

3.6 Vertical structure eigenvalues and eigenfunctions 50

Results and Discussion **56**

4.1 Synopsis 56

4.2 Scatter diagrams and the evolving block 58

4.3 The slope $dq/d\psi$: hydrodynamic stability, modon existence condition, and the modon radius 62

4.4 Vorticity flux and the area of the $q(\psi)$ plots 67

4.5 The baroclinicity of the block 70

Conclusions **74**

5.1 The modon free mode 74

5.2 The baroclinicity 75

5.3 Forecasting the block 76

5.4 Suggestions for further study 77

References **79**

Appendix A1 ..... **84**

Vorticity flux, $q(\psi)$ plot area, and least squares $q(\psi)$ slope-intercept values 84

Root-Mean-Square Values of the Vertical Normal Modes Fourier Coefficients 86

Appendix A2 ..... **88**

500 mb vorticity-stream-function scatter plots, and stream-function and vorticity contour charts 88

List of Figures

Figure 1.1 Mean 500 mb geopotential height for February 1989 2

Figure 1.2 Co-moving stream-function and potential vorticity for an equivalent barotropic modon embedded in a westerly flow 4

Figure 3.1.1 The region covered by the data grid 40

Figure 3.2.1 Portion of the lat-long grid with variable zonal grid-spacing 41

Figure 3.2.2 Vertical differencing scheme 44

Figure 3.5.1 Evaluating the (ψ,q) area integral. 49

Figure 3.6.1 Evaluation of $U'(p_t)/U(p_t)$, showing the region over which the term is averaged. 50

Figure 4.2.1 q(ψ) plots showing the difference in curvature between intense-jet anomaly, and split-jet anomaly. 60

Figure 4.2.2 Scatter diagrams of 500 mb geostrophic stream-function versus potential vorticity, highlighting values from within the region over Northeast Asia. 61

Figure 4.3.1 Illustration of Arnold's second stability theorem. 63

Figure 4.3.2 The slopes of the least-squares 500 mb q(ψ) lines, with the estimated minimum slope for stability 64

Figure 4.4.1 Time series of the area of 500 mb q(ψ) scatter plots, and the net vorticity flux (smaller region) 68

Figure 4.4.2 Time series of the area of 500 mb q(ψ) scatter plots, and the net vorticity flux (larger region) 69

Figure 4.5.1 Profiles of vertical normal modes. 71

Figure 4.5.2 Time series of normalized RMS Fourier coefficients of the four gravest vertical normal modes. 72

List of Symbols

A coefficient in the power law for $\sigma_r = Ap^{-2+\epsilon}$

a modon radius

a_n n^{th} Fourier coefficient in vertical normal mode expansion

c phase speed

D equivalent depth

f Coriolis parameter

F rotational Froude number = $(R_d/L)^2$

g gravitational acceleration constant = 9.80665 ms^{-2}

i northward grid index

j eastward grid index

$\hat{k}$ unit vector in local (Cartesian) vertical direction

k_n n^{th} eigenvalue of the vertical structure equation

L horizontal length scale

$\hat{n}$ unit outward normal vector

p pressure (vertical coordinate)

p_0 reference pressure (for scaling)

Q equivalent barotropic potential vorticity

q baroclinic potential vorticity

R_d Rossby deformation radius

U background zonal wind speed

U_* horizontal wind speed scale

x zonal horizontal coordinate (increasing eastward)

y meridional horizontal coordinate (increasing northward)

Z geopotential height of an isobaric surface

β northward gradient of Coriolis parameter

Γ $\equiv -dT/dz$, atmospheric lapse rate

γ modon exterior wavenumber

ϵ Rossby number $\equiv U_*/(f_0 L)$

ϵ small parameter ($0 < \epsilon \ll 1$) in power law for σ_r

ζ_a vertical component of absolute vorticity

θ potential temperature

ϑ plane polar angle, $= \tan^{-1} y/x$

$\Lambda = dq/d\psi$: slope of $q(\psi)$ plot

λ modon interior wavenumber

ρ air density

$\sigma_r = (\rho_r \theta_r)^{-1} d\theta_r/dp$: static stability

ϕ geopotential

φ non-dimensional stream-function

Ψ vertical structure function

ψ geostrophic stream-function $\equiv \phi/f_0$

∇^2 two-dimensional (horizontal) Laplacian operator

$\partial \mathbf{C}$ boundary of the region $\mathbf{C}$

$\langle \bullet \rangle_5$ centred 5-day average of $\bullet$

Chapter 1

Introduction

The term 'blocking' is used by both theoreticians and weather forecasters to mean large atmospheric flow disturbances or pressure cells, most often in mid-latitudes, which are nearly stationary, and long-lasting compared to synoptic-scale systems. An early, widely-used set of criteria for blocks was given by Rex (1950). Using his definition, 'blocking' implies that: the upper tropospheric flow splits abruptly into two jet streams, each of which extends over at least 45 degrees of longitude, and this condition lasts for at least ten days. The usual westerly flow of smaller, weather-bearing disturbances is diverted or blocked, hence the term block. During its lifetime, the block is not dislodged by even the most energetic synoptic systems.

Blocks occur often enough to affect year-to-year climate, and they tend to re-occur over the same regions, with some seasonal variation. In the northern hemisphere, the two main areas are the Northeast Atlantic and Northeast Pacific, at the end of the storm tracks (Chang, 1972). A third area of slightly less frequent blocking lies over the northern Soviet Union. For the entire hemisphere, Quiroz (1987) found an average of 16 blocks per year, each lasting greater than 5 days. Rex's criteria are somewhat stringent, eliminating many cases that do not last for a full ten days; in addition, they do not distinguish between normal and extreme blocking episodes, either in terms of amplitude or duration. It is difficult to make an entirely objective definition of a block in terms of duration (Quiroz, 1987). In rare instances, a block may appear to last for several months. For example, in 1959, a blocking anticyclone that formed over the Northeast Atlantic in January persisted into late fall, with a few brief interruptions. The result was a severe drought over Central Europe that summer (Chang, 1972).

Atmospheric blocking thus results in prolonged periods of anomalous weather, over large geographical areas. The temporal frequency of occurrence is sufficiently irregular that medium- to long-range prediction of blocks is still elusive. Hence the physical understanding leading to accurate long-range forecasting of blocks remains a fascinating and challenging research topic.

In the case to be examined in this work, a Northeast Pacific block formed in January 1989, accompanying a strong outbreak of continental arctic air over North

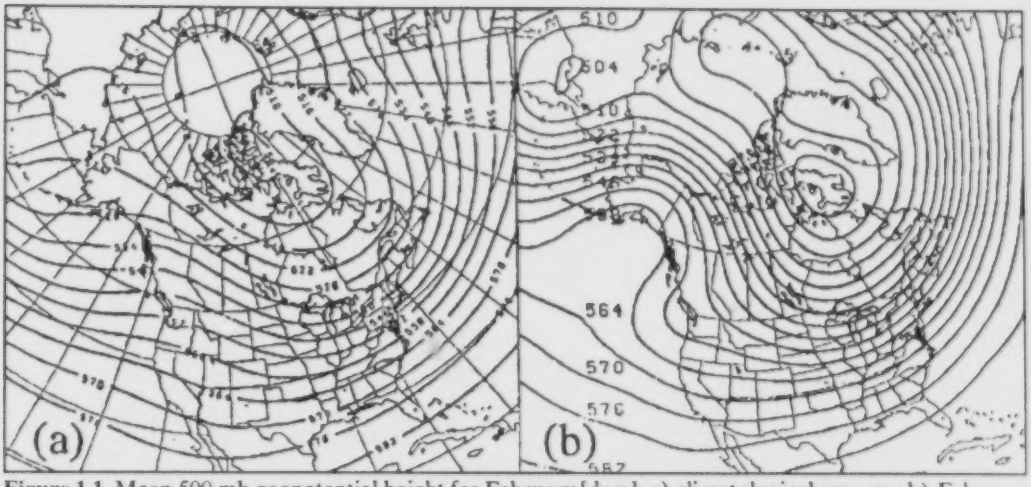

Figure 1.1 Mean 500 mb geopotential height for February [dam]; a) climatological average; b) February 1989.

America. Except for some minor zonal shifting, the block persisted until the end of February. The 500 mb height field, averaged for the entire month of February, is shown in Figure 1.1. It shows an extraordinarily strong ridge over Alaska and the Gulf of Alaska, with height anomalies greater than 30 dam in this region (d'Amours, 1989).

We may divide the episode into two periods, based on the form of the flow pattern at 500 mb. During the first period, from about February 1 to 15, the flow pattern had the familiar 'Omega' shape. During the second, shorter period, February 16 to 22, immediately before it broke down, the block developed a discernible dipole-like ('high-over-low') form. Daily 500 mb charts averaged over 5 days are given in Appendix A2.

The principal goal of this work is to see whether mid-tropospheric data from this event are consistent with theories that treat blocks as persistent, coherent structures. More specifically, we are interested in structures that correspond to free-mode solutions of the governing equations, for which the potential vorticity, q, and the stream-function, ψ, are functionally related as $q = q(\psi)$. A free mode for *blocking* flows would be analogous to (but not necessarily the same as) the Rossby wave, which, in the absence of any forcing, is a free mode of the *non-blocking* category of flows. We concentrate on a particular free mode called the *modon*, and we examine

our data to see whether this block, during its dipole-like configuration, displays any of its basic dynamical characteristics. Central to our analysis is the relation between geostrophic stream-function and vorticity. This approach has been used in the study of a Northeast Atlantic block (Butchart et al. 1989), but there is no known application of the method to Northeast Pacific blocks. This thesis addresses this deficiency.

The search for realistic yet tractable theoretical prototypes of long-lived geophysical vortices, has led to intensive study of the modon, as well as other free mode structures (Flierl 1987, Malguzzi and Malanotte-Rizzoli 1984). Modons are flow-patterns that can be exactly derived from the fully non-linear, quasi-geostrophic equations of motion. The stream-function (or pressure-pattern) of a steadily-translating beta-plane modon is shown in cartesian coordinates in Figure 1.2. It is an anti-symmetric cyclone-anticyclone dipole moving in an otherwise quiescent flow. Although it is highly idealized, the modon is considered by some researchers to be promising as a prototype that displays essential dynamical features of the dipole-type blocking flows. For example, an isolated barotropic eddy on the beta-plane can be persistent only if it has zero net relative angular momentum (Stern, 1975; Flierl et al., 1983). The simplest means by which this requirement is met, is for the eddy to be composed of a cyclone-anticyclone dipole.

The modon divides the flow into two separate regions:

1. an interior region of closed contours, and strong vorticity gradients;
2. the exterior, with open contours, and relatively weak vorticity gradients.

The trapping of fluid particles in the interior region is another important characteristic of a blocking prototype. If the modon interior is lying in an area of anomalous forcing, the trapped fluid can become highly modified, and rapid amplification is possible.

A plot of vorticity versus co-moving stream-function for the modon, using points from the entire domain, yields *two* straight lines. The line associated with interior points has the steeper slope. This particular *non-analytic* vorticity-stream-function relationship is the modon 'signature' that distinguishes it from other free mode solutions that are linear (e.g. Rossby waves), or weakly non-linear, such as the

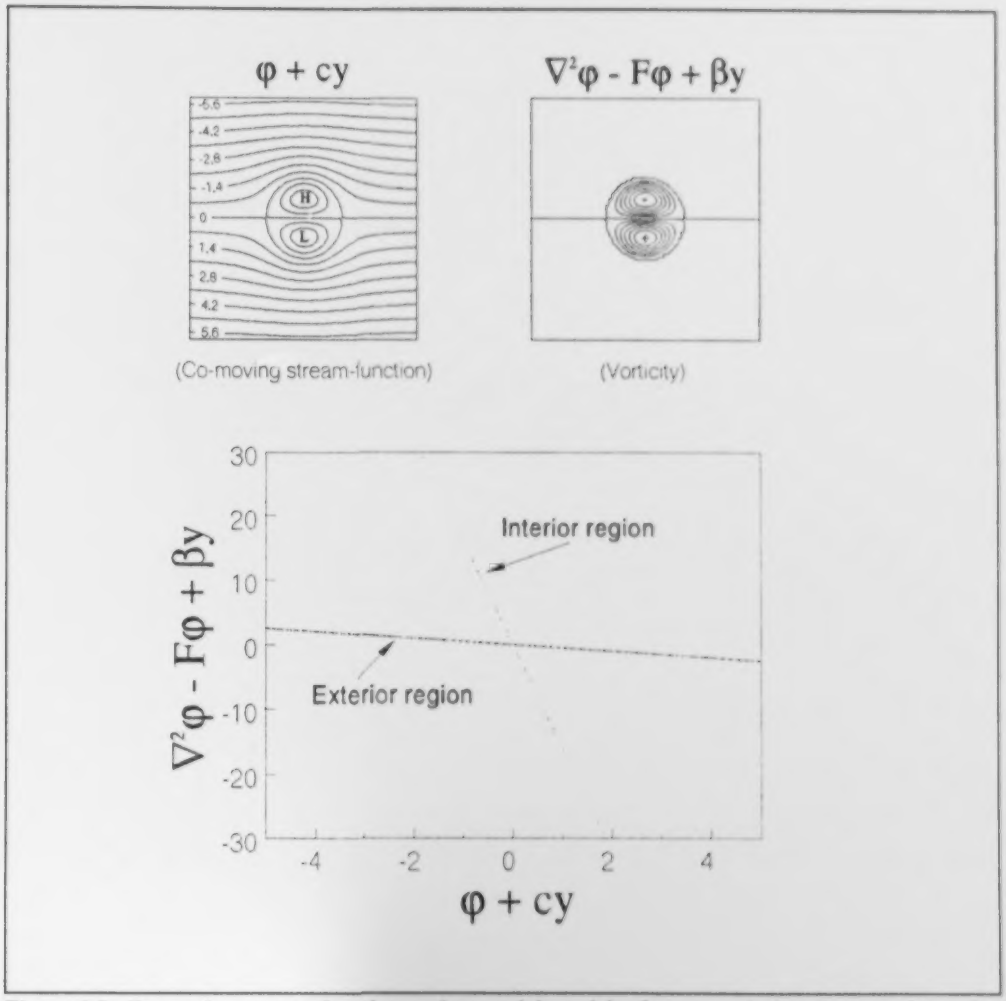

Figure 1.2 Co-moving stream-function and potential vorticity for an equivalent barotropic modon embedded in a westerly flow. The solution is outlined in section 2.2.1.

solitary wave discussed by Malguzzi and Malanotte-Rizzoli (1984).

The mathematical modon existence condition excludes stationary Rossby waves in the exterior region (McWilliams, 1980; Flierl, 1987), so that Rossby waves and modons belong to disjoint flow regimes. This is consistent with the theory of multiple equilibria, first introduced by Charney and Devore (1979) in the context of global-scale Rossby-wave resonance, and then extended to localized structures by Pierrehumbert and Malguzzi (1984). The range of allowable phase speeds of modons is outside that of Rossby waves. In fact, a stationary, fully barotropic beta-plane

modon cannot exist in a westerly current, although Verkley (1987) managed to construct barotropic modons on a spherical surface. For the equivalent barotropic and baroclinic cases, stationary modons can exist in a realistic westerly background flow (Flierl et al., 1980).

Numerical investigations of modon dynamics (and hence, their applicability to blocking) have examined their behaviour under increasingly realistic conditions, such as interactions with topography (Swaters, 1986; Carnevale et al., 1988), or the Ekman boundary-layer (Swaters and Flierl, 1989). In general, modons have been found to be rather stable. The stability of modons and modon-like structures is considered by some to be problematic in the case of rapid development and evolution of a block. Frederiksen and Bell (1990) suggest that an exact, steady, and robust modon solution may be inadequate for modelling blocks, which can develop rapidly out of an unstable flow configuration, and then display complex transient behaviour for their duration.

However, Haines and Marshall (1987) demonstrated, in a barotropic beta-plane model, that dipole eddy forcing of an initially zonal flow could rapidly excite modon-like structures, and maintain them against dissipation by friction and Rossby wave radiation. Haines (1989) extended this to a two-level baroclinic model. In both instances, it was shown that, if the mathematical existence condition were relaxed, modons could rapidly develop, and then coexist with Rossby waves, for time scales comparable with blocking duration times.

Asymmetric modons have been found experimentally. Flierl et al. (1983) produced modons from simple barotropic 'jet streams' in rotating tank experiments. These asymmetric modons travelled in curved paths, and interacted with other vortices produced by the jets.

There have been relatively few observational studies seeking nonlinear modon characteristics in dipole-like blocking situations. McWilliams (1980) investigated the January 1963 Northeast Atlantic blocking incident. His attempt to show that the zonally- and vertically-averaged data supported the modon existence condition was inconclusive, even though the blocking stream-function bore a strong visual resemblance to that of a modon. Using a different approach, Butchart et al. (1989) plotted scatter diagrams of potential vorticity versus stream-function, from the October 1987 Northeast Atlantic block. Their diagrams clearly indicate a non-

analytic, very roughly linear relationship between the two variables. The same general results were obtained for plots of absolute vorticity versus stream-function, which indicated that, at least in the case they examined, Northeast Atlantic blocks may be reasonably well-modelled by the equivalent barotropic modon. The scatter diagrams were thus found to be useful in a qualitative sense. Read et al. (1986) showed how the area of the $q(\psi)$ plots is equivalent to the net geostrophic vorticity flux, and is therefore also a quantitative measure of the degree of departure of the system from a free mode state, for which the $q(\psi)$ plot area vanishes.

Butchart et al. (1989) noted that Pacific blocks are usually of the 'Omega' form, and so are not often as symmetric as the Atlantic blocks, which frequently have a dipolar form. Hence the Pacific blocks may not be well-modelled by simple beta-plane modons, and they suggested that asymmetric modons in spherical co-ordinates, or modons in external shear flows, might be more appropriate for that region.

Thus far, observational investigation of the atmospheric modon model has been limited to evaluations of blocking over the Northeast Atlantic region. This thesis addresses this deficiency by presenting scatter diagrams for the Northeast Pacific, calculated on the 500 mb surface, for the period January 23 through February 26, 1989. In addition to examining the qualitative appearance of the diagrams, we investigate the relation between certain quantities calculated from our (ψ,q) scatter-plot data, and the relevant free mode parameters. In particular:

i. The area of each $q(\psi)$ plot is computed and compared to the net geostrophic flux of vorticity into the blocking region, to test the results of Read et al. (1986). This result states that the area can be interpreted as measuring the departure of the system from *any* free mode solution of the quasi-geostrophic equations of motion.

ii. The slopes of least-squares-fit $q(\psi)$ lines for the scatter-plots are used to test the modon existence condition. The slopes can also be used to qualitatively examine the hydrodynamical stability of the flow.

iii. For each day on which the existence condition is satisfied, the data is used to compute a modon radius value. This is compared with the actual block dimensions. For the days on which the block has a dipolar form, we compare the observed separation of the vorticity extrema with that predicted by the

modon model. The degree to which the compared quantities are equal indicates the consistency of our data with the modon model.

The baroclinicity within the blocking region is examined. A set of vertical normal modes is obtained, using a power-law relation for the tropospheric static stability derived from our data, with the approximation of a constant lapse rate. We calculate the Root-Mean-Square contribution, of each of the four lowest normal modes, to the blocking eddy component of stream-function within the block, in order to ascertain the degree of baroclinicity.

The organization of the thesis is as follows. Chapter 2 outlines the theoretical background, presenting the mathematical derivation of the modon solution, the vertical normal modes, and the strategy of testing our data for free mode characteristics. Chapter 3 is a description of the computational process, including summaries of the finite-differencing, smoothing, and integration algorithms. Chapter 4 is a discussion of the evolution of the block, and of the results of our computations. Conclusions are presented in Chapter 5.

Chapter 2

Theoretical Background

The mathematical analysis of a meteorological problem is typically initiated by a systematic reduction of the quite complex atmospheric motion equations to something more manageable. The reduction is accomplished by applying physical scaling procedures (Holton 1979; Pedlosky 1987) which effectively isolate those scales of motion that are to be studied. In our case we are interested in space scales of the order of 1000 km, and time scales large compared to one day. The analytical results may be compared with a numerical simulation, or, as in this study, with observed data. The degree to which the two are consistent can indicate the extent to which the choice of scaling, and hence the model, is justified.

In this chapter we first discuss some of the concepts underlying current fundamental research of blocking fluid dynamics. We outline the classical equivalent barotropic modon solution, and then present in detail the baroclinic geostationary modon solution to the frictionless, source-free quasi-geostrophic vorticity equation. During our analysis we perform a separation of variables. This leads to a horizontal modon solution, and a vertical structure equation. We find an exact analytic solution to the vertical structure eigenvalue problem, by employing a simple power-law for the vertical static stability that fits our data well. The resulting eigensolutions are orthonormalized, to be used as basis functions, or normal modes for the vertical structure within the blocking region. The relative contribution of each normal mode to the vertical structure measures the degree of baroclinicity within the block. The final two sections introduce the scatter diagram, and the way in which stream-function-vorticity plots may be used to determine whether the block displays either modon or general free mode characteristics.

2.1 Regional blocking theories

The mathematical techniques that are used in the study of blocking flows are practically the same as those used in studying ocean ring-eddies, Jupiter's Great Red Spot, and plasma vortices (e.g. in fusion reactors). Common to all of these examples are the following observed dynamical properties (Flierl 1987):

a. Nearly geostrophic balance.
b. Structures are spatially isolated, i.e. the phenomena are regional rather than global.
c. Non-linear effects cannot be neglected. This is usually equivalent to stating that the system is of finite amplitude, in contrast to linear theory, in which waves are often assumed to be of infinitesimal amplitude.
d. Potential vorticity gradients are significant.

Physical systems thus characterized are described as *coherent* wave structures. The term *solitary waves* is also used, to distinguish them from the more familiar wave-trains (such as Rossby waves).

At this point an explanation of the terms 'regional' and 'global' is in order. Depending on which atmospheric motion scales are emphasized, theories of blocking mechanisms fall into either one of two different categories (Haines and Marshall 1987):

i) the global approach;
ii) the regional, or local description.

Theories based upon a *global* approach assume that a block is a global phenomenon, i.e. the block, and its controlling factors, or forcings, are on the global or planetary scale. A typical planetary horizontal length scale is 10^7 m (Holton 1979); this can be thought of as an average wavelength for planetary-scale waves. Global theories treat the meridional flow-pattern of a block as resulting from resonant interactions of planetary (Rossby) waves, either with each other, or with some forcing mechanism such as bottom topography. It should be mentioned that forcings by global-scale anomalous sea surface temperatures appear to contribute relatively little to mid-latitude block formation (Wallace and Blackmon 1983; Shukla 1986). The opposite appears to be true for smaller scales, however. Kung et al. (1990) found that general circulation model (GCM) simulations of blocking episodes were improved somewhat, when high resolution sea surface temperature data were utilized.

An example of a global approach is that of Austin (1980), who demonstrated, using a spectral (Fourier) analysis, that the two main northern hemisphere blocking regions lie near the two main areas of constructive interference of stationary

planetary-scale atmospheric waves. Further analysis in this direction could be in the context of resonant wave-wave interactions.

Modons, first discussed by Stern (1975) and Larichev and Reznik (1976), fall into the category of *regional* theories. These theories are based upon the idea that, while blocks themselves may be of the planetary scale, they are actually quite localized with respect to the background flow; the really significant *forcings* for blocks are believed to be on a smaller, synoptic scale. A typical length scale for synoptic weather systems is 10^6 m. During the past decade considerable evidence has accumulated indicating that synoptic-scale eddies are essential to the growth and persistence of blocking flows. Hansen and Chen (1982), using spectral analyses, discovered that, in addition to the linear superposition of planetary-scale waves, blocking can develop during periods of non-linear forcing of planetary waves (zonal wavenumbers 1 to 4) by intense baroclinic *synoptic-scale* waves (zonal wavenumbers 5 to 10). This non-linear interaction occurs in *discontinuous* episodes of strong energy transfer. Other observational studies like that of Dole and Gordon (1983) and Mak (1991), suggest that development and decay of blocks are highly affected by synoptic-scale disturbances.

The results of Illari (1984) strongly suggest that the 1976 'European Drought' block was kept from being advected down-stream, by synoptic-scale eddy forcing. Isentropic analyses presented by Shutts (1983), and Hoskins et al. (1985), revealed the nature of this forcing, called 'eddy-straining'. This process was highlighted in the work of Shutts (1986), in a case study of 1983 Northeast Atlantic blocking, and Haines and Marshall (1987), in numerical experiments. They showed how synoptic-scale barotropic eddies are deformed in the diffluent flow of the block, thereby maintaining it against frictional dissipation. The zonal compression of the eddy-train, as it enters the split-jet area, naturally leads to a dipole structure of the forcing field. Thus was discovered a physical mechanism to account for the persistence of blocks, which appears to have run counter to earlier intuition: rather than being dislodged by synoptic-scale disturbances, blocks could in fact be strengthened by them.

It is evident, therefore, that synoptic-scale eddies can be the dominant forcing mechanism for the growth and maintenance of blocks. A corollary to this is that a block can be at least partially isolated from, or independent of, the mean planetary-scale flow in which it is embedded, since it is affected mainly by the smaller-scale disturbances. Such a system is said to be *coherent*.

2.2 Baroclinic modon solutions to the quasi-geostrophic equations

In this section we first outline the classical equivalent barotropic modon solution. Then a detailed derivation of the baroclinic modon solution is presented.

2.2.1 Steadily-travelling equivalent barotropic modon solution

In the equivalent barotropic case, the quasi-geostrophic potential vorticity equation can be written in the *non-dimensional* form (Pedlosky 1987)

$$\frac{\partial}{\partial t}(\nabla^2\varphi - F\varphi + \beta y) + J(\varphi, \nabla^2\varphi - F\varphi + \beta y) = 0, \qquad (2.2.1)$$

where we define the following non-dimensional variables:

$Q \equiv \nabla^2\varphi - F\varphi + \beta y$ is the equivalent barotropic potential vorticity;
$F = (L/R_d)^2$ is the rotational Froude number;
R_d and L are respectively the deformation radius and length scale;
β is the northward gradient of the Coriolis parameter;
φ is the stream-function;
and the Jacobian determinant of functions a and b with respect to the non-dimensional coordinates x and y is defined as

$$J(a,b) \equiv \frac{\partial a}{\partial x}\frac{\partial b}{\partial y} - \frac{\partial a}{\partial y}\frac{\partial b}{\partial x}.$$

For a steady solution that is translating at a constant zonal speed c, we can transform to co-moving co-ordinates, which results in a new zonal derivative term that absorbs the time derivative. Letting $\xi = x\text{-}ct$, the t- and x-derivatives map as:

$$\partial/\partial t = -c\,\partial/\partial\xi,$$
$$\partial/\partial x = \partial/\partial\xi,$$

while the y-derivatives remain unchanged. Substituting these relations into the vorticity equation (2.2.1) yields

$$J(\varphi + cy, Q) = 0, \qquad (2.2.2)$$

in which the Jacobian is now with respect to the co-moving independent variables ξ and y. Equation (2.2.2) implies that there is a functional relationship between the two dependent variables (vorticity and co-moving stream-function):

$$Q = \mathcal{F}(\varphi + cy). \tag{2.2.3}$$

To proceed beyond (2.2.3) it is necessary to determine the form of the function $\mathcal{F}$. Since we are looking for a localized structure, we require that the disturbance decay to zero at infinity sufficiently rapidly that the energy and enstrophy (mean-square vorticity) are finite. Thus, for all streak-lines, $\varphi + cy$ = constant, which extend to infinity, it follows from (2.2.3) that the function $\mathcal{F}$ has the linear form

$$\mathcal{F}(z) = (\beta/c)z. \tag{2.2.4}$$

The classical modon solution now *assumes* that the co-moving streamlines exterior to a circle of radius r = a (where $r^2 = \xi^2 + y^2$) extend to infinity; those interior to this boundary do not. For the exterior region (r > a), it follows from (2.2.3) and (2.2.4) that

$$\nabla^2\varphi - (F + \beta/c)\varphi = 0. \tag{2.2.5}$$

For the interior (r < a) streak-lines that do not extend to infinity, it is then assumed that the relation is also linear, but of a different form. This choice has the following physical justification. For quasi-geostrophic two-dimensional turbulent flow, the cascade of enstrophy is generally from large to small scales (Pedlosky 1987). Hence it may be expected that a persistent large-scale structure should be in a state of minimal enstrophy. Stern (1975) showed, using variational methods, that the requirement of minimal enstrophy leads to a linear vorticity-stream-function relationship, for an isolated barotropic eddy. Leith (1984) derived similar results for differing classes of isolated vortices. In addition to these theoretical considerations, there is mounting observational evidence, in the form of vorticity versus stream-function scatter diagrams such as our own, that the relation *is* linear.

Assuming, then, the following linear relation, for r < a,

$$Q = -(\chi^2 + F)(\varphi + cy), \tag{2.2.6}$$

where χ is a real number, we easily obtain a second, inhomogeneous, Helmholtz equation

$$\nabla^2\varphi + \chi^2\varphi = -(\beta + cF + c\chi^2)y. \tag{2.2.7}$$

The stream-function φ of the modon must be a solution to (2.2.5) and (2.2.7). To close the problem, we need to match the solutions across the modon radius $r = a$. It can be easily shown (and we discuss this in more detail in section 2.2.2) that for the modon to have continuous vorticity across $r = a$, we must have

$$\varphi + cy = 0 \tag{2.2.8}$$

on $r = a$. In addition, we require that the velocity be continuous across $r = a$.

The solution to (2.2.5) and (2.2.7), subject to (2.2.8) and the continuity of velocity is

$$\varphi = -\frac{acK_1(\eta r)}{K_1(\eta a)}\sin\vartheta, \quad r > a, \tag{2.2.9a}$$

$$\varphi = \left[\frac{a(\beta+cF)J_1(\chi r)}{J_1(\chi a)} - (\beta+cF+c\chi^2)\right]\frac{\sin\vartheta}{\chi^2}, \quad r < a, \tag{2.2.9b}$$

where J_1 and K_1 are respectively the ordinary and modified Bessel functions of the first kind of order one. The variable ϑ is the plane-polar azimuth, given by $\tan\vartheta = y/\xi$, while η is defined as

$$\eta^2 = \beta/c + F.$$

η, χ and the radius a satisfy the dispersion relation (derived in detail in section 2.2.2)

$$-\frac{K_2(\eta a)}{\eta K_1(\eta a)} = \frac{J_2(\chi a)}{\chi J_1(\chi a)}. \tag{2.2.10}$$

2.2.2 Derivation of the governing baroclinic equations

We begin with the following *dimensional* equations of motion for an incompressible, frictionless, adiabatic atmosphere in hydrostatic balance (Holton 1979)

$$u^*_{t^*} + u^* u^*_{x^*} + v^* u^*_{y^*} + \omega^* u^*_{p^*} - fv^* = -\Phi^*_{x^*}, \tag{2.2.11a}$$

$$v^*_{t^*} + u^* v^*_{x^*} + v^* v^*_{y^*} + \omega^* v^*_{p^*} + fu^* = -\Phi^*_{y^*},$$

$$\Theta^*_{t^*} + u^* \Theta^*_{x^*} + v^* \Theta^*_{y^*} + \omega^* \Theta^*_{p^*} = 0, \tag{2.2.12}$$

$$u^*_{x^*} + v^*_{y^*} + \omega^*_{p^*} = 0. \tag{2.2.13}$$

$$\Phi^*_{p^*} = -\frac{1}{\rho^*}, \tag{2.2.14}$$

Stars are used throughout this section to denote dimensional quantities. Partial derivatives with respect to a variable are denoted by subscripts in that variable. The potential temperature, Θ^*, is defined, using the Ideal Gas Law, $T = p/\rho R$, as

$$\Theta^* = \frac{p^*}{\rho^* R}\left(\frac{p_0}{p^*}\right)^{R/c_p}, \tag{2.2.15}$$

and we assume a beta-plane approximation for the Coriolis parameter

$$f = f_0 + \beta^* y,$$

where f_0 is chosen to be the reference Coriolis parameter at 60°N. The remaining variables are

(x^*,y^*), the horizontal coordinates, which increase eastward and northward, respectively,
p^*, the pressure,
t^*, time,

(u^*,v^*,ω^*), the components of velocity in isobaric coordinates,
$\Phi^* = \Phi^*(x^*,y^*,p^*,t^*)$, the geopotential,
and ρ^*, the density.

We proceed to non-dimensionalize the variables using the following scales

$$(x^*,y^*) = L(x,y),$$
$$p^* = p_0 p,$$
$$t^* = (L/U_*)t,$$
$$\beta^* = (U_*/L^2)\beta,$$
$$(u^*,v^*) = U_*(u,v),$$
$$\omega^* = (\varepsilon p_0 U_*/L)\omega,$$
$$\varepsilon = U_*/(f_0 L).$$

Furthermore, we assume that the variables Φ^*, Θ^*, and ρ^* each consist of a *dynamically inert* reference component (which is in hydrostatic balance) plus a departure from the reference value, which we call the dynamic anomaly, i.e.

$$\Phi^* = \phi_r(p^*) + \phi^*(x^*,y^*,p^*,t^*), \tag{2.2.16}$$
$$\Theta^* = \theta_r(p^*) + \theta^*(x^*,y^*,p^*,t^*), \tag{2.2.17}$$
$$\rho^* = \rho_r(p^*) + \rho^*(x^*,y^*,p^*,t^*). \tag{2.2.18}$$

The reference components thus satisfy

$$\frac{\partial \phi_r}{\partial p^*} = -\frac{1}{\rho_r},$$
$$\theta_r = \frac{p^*}{\rho_r R}\left(\frac{p_0}{p^*}\right)^{R/c_p}.$$

We non-dimensionalize the anomaly fields as

$$\phi^* = f_0 U_* L\phi,$$
$$\theta^* = (f_0 U_* L/R)\theta,$$
and $$\rho^* = p_0/(f_0 U_* L)\rho.$$

With the exception of the reference variables, un-starred variables are non-dimensional. We now introduce the expressions (2.2.16), (2.2.17), (2.2.18), together

with all of our non-dimensional variables, into the equations (2.2.11) through (2.2.15). After rearranging, we are left with the following *non-dimensional* equations

$$\varepsilon [u_t + uu_x + vu_y + \varepsilon \omega u_p] - [1 + \varepsilon \beta y]v + \phi_x = 0, \tag{2.2.20a}$$

$$\varepsilon [v_t + uv_x + vv_y + \varepsilon \omega v_p] + [1 + \varepsilon \beta y]u + \phi_y = 0, \tag{2.2.20b}$$

$$\theta_t + u\theta_x + v\theta_y + \frac{R}{f_0^2 L^2} \frac{d\theta_r}{dp} \omega \theta_p + \varepsilon \omega \theta_p = 0, \tag{2.2.21}$$

$$u_x + v_y + \varepsilon \omega_p = 0. \tag{2.2.22}$$

$$\phi_p = -\frac{1}{\rho}, \tag{2.2.23}$$

with θ given by

$$\theta = \frac{p}{\rho}^{1 - R/c_p}. \tag{2.2.24}$$

We are interested in large-scale atmospheric motions, which are characterized by a small Rossby number, i.e. $0 < \varepsilon \ll 1$ (Holton 1979). We can employ the technique of expanding each of the dependent variables in an asymptotic series in ε (Bender and Orszag 1978), thus

$$(u,v,\phi,\theta,\rho) \approx (u,v,\phi,\theta,\rho)^{(0)} + \varepsilon (u,v,\phi,\theta,\rho)^{(1)} + \varepsilon^2 (u,v,\phi,\theta,\rho)^{(2)} + \ldots$$

The superscripts (0), (1), (2), etc. indicate the order, and are not exponents. When we substitute the non-dimensional equations (2.2.20) through (2.2.24) into this asymptotic expansion, we obtain one set of equations for each power of ε. For the O(1) equations, which contain all terms multiplied by $\varepsilon^0 = 1$, we have

$$v^{(0)} = \phi_x^{(0)}, \tag{2.2.25a}$$

$$u^{(0)} = -\phi_y^{(0)}, \tag{2.2.25b}$$

$$\theta_t^{(0)} + u^{(0)}\theta_x^{(0)} + v^{(0)}\theta_y^{(0)} + \frac{R}{f_0^2 L^2}\frac{d\theta_r}{dp}\omega^{(0)} = 0, \tag{2.2.26}$$

$$u_x^{(0)} + v_y^{(0)} = 0, \tag{2.2.27}$$

$$\phi_p^{(0)} = -\frac{1}{\rho^{(0)}}, \tag{2.2.28}$$

$$\theta^{(0)} = \frac{p^{1-R/c_p}}{\rho^{(0)}}. \tag{2.2.29}$$

We note that (2.2.25a) and (2.2.25b) are simply the geostrophic wind equations. Combining (2.2.28) and (2.2.29) results in

$$\theta^{(0)} = -\left[p^{1-R/c_p}\right]\phi_p^{(0)}, \tag{2.2.30}$$

which we can use to substitute for $\theta^{(0)}$ in (2.2.26), yielding the quasi-geostrophic energy equation

$$(\phi_p^{(0)})_t + J(\phi^{(0)}, \phi_p^{(0)}) + \sigma_r \omega^{(0)} = 0, \tag{2.2.31}$$

in which the static stability parameter σ_r is defined as

$$\sigma_r(p) \equiv -\frac{p_0}{f_0^2 L^2}\left[\frac{1}{\rho_r \theta_r}\frac{d\theta_r}{dp}\right], \tag{2.2.32}$$

and the Jacobian determinant is

$$J(a,b) \equiv a_x b_y - a_y b_x.$$

The $O(\varepsilon)$ equations are

$$(-\phi_y^{(0)})_t + J(\phi^{(0)},-\phi_y^{(0)}) - \beta y \phi_x^{(0)} - v^{(1)} + \phi_x^{(1)} = 0, \qquad (2.2.33a)$$

$$(\phi_x^{(0)})_t + J(\phi^{(0)},\phi_x^{(0)}) + \beta y \phi_y^{(0)} + u^{(1)} - \phi_y^{(1)} = 0, \qquad (2.2.33b)$$

$$u_x^{(1)} + v_y^{(1)} + \omega_p^{(0)} = 0. \qquad (2.2.34)$$

Subtracting ∂_y(2.2.33a) from ∂_x(2.2.33b) yields

$$\frac{D}{Dt}[\nabla^2\phi^{(0)} + \beta y] + u_x^{(1)} + v_y^{(1)} = 0, \qquad (2.2.35)$$

in which we have defined the operator

$$\frac{D}{Dt} \equiv \frac{\partial}{\partial t} + J(\phi_x^{(0)},).$$

We can substitute (2.2.34) into (2.2.35) to eliminate the $O(\varepsilon)$ u and v terms, which results in

$$\frac{D}{Dt}[\nabla^2\phi^{(0)} + \beta y] - \omega_p^{(0)} = 0. \qquad (2.2.36)$$

From (2.2.31) we can write

$$\omega_p^{(0)} = -\frac{D}{Dt}\left[\frac{\partial}{\partial p}\left(\frac{1}{\sigma_r}\phi_p^{(0)}\right)\right],$$

and if we substitute this into (2.3.36) and re-arrange terms, we obtain

$$q_t + J(\phi^{(0)},q) = 0, \qquad (2.2.37)$$

where we have defined the quasi-geostrophic potential vorticity, q, as

$$q \equiv \nabla^2\phi^{(0)} + \beta y + \frac{\partial}{\partial p}\left(\frac{1}{\sigma_r}\frac{\partial\phi^{(0)}}{\partial p}\right). \qquad (2.2.38)$$

2.2.3 Geostationary modon embedded in a stratified zonal flow

In this section all variables are dimensional, so that the units are the same as those of our data. We re-dimensionalize (2.2.38) using the scales of section 2.2.2, obtaining the following equation for the source-free quasi-geostrophic potential vorticity on a beta-plane

$$\frac{\partial q}{\partial t} + J(\psi,q) = 0, \qquad (2.2.39)$$

in which ψ is the geostrophic stream-function, given by

$$\psi \equiv \phi/f_0,$$

q is the quasi-geostrophic potential vorticity, given by

$$q = \nabla^2\psi + \beta y + f_0^2\frac{\partial}{\partial p}\left(\frac{1}{\sigma_r}\frac{\partial\psi}{\partial p}\right), \qquad (2.2.40a)$$

and where the static stability parameter, σ_r, is defined as

$$\sigma_r = -\frac{1}{\rho_r\theta_r}\frac{d\theta_r}{dp}, \qquad (2.2.40b)$$

The other variables in (2.2.39) and (2.2.40) have the same meaning as the reference and/or dynamic anomaly variables in section 2.2.2.

We now present the details of the solution. For the classical equivalent barotropic modon, we worked within a coordinate system in which the modon was propagating with a constant zonal speed. Atmospheric blocks, on the other hand, are

more or less geostationary in the usual fixed reference frame. The solution we present for the continuously vertically-stratified problem represents a stationary or steady modon embedded in a stratified zonal flow, with no meridional shear. Our solution procedure follows that of Haines and Marshall (1989). Our starting point is equation (2.2.39), which in the stationary case leads to

$$q = \mathcal{F}(\psi) \tag{2.2.41}$$

Proceeding as in Haines and Marshall (1989), we assume that both stream-function and vorticity can be expressed as linear combinations of zonal background plus eddy fields, namely

$$\psi = \psi_0(y,p) + \psi_1(x,y,p), \tag{2.2.42a}$$
$$q = q_0 + q_1(x,y,p). \tag{2.2.42b}$$

We note that ψ_1 in (2.2.42a) is the dynamic anomaly, which is the departure from the reference state. The background zonal-flow stream-function is assumed to be of the form

$$\psi_0 = - U(p)y, \quad U(p) > 0, \tag{2.2.43}$$

so that the background vorticity, given by

$$q_0 = \beta y + f_0^2 \frac{\partial}{\partial p}\left(\frac{1}{\sigma_r}\frac{\partial \psi_0}{\partial p}\right),$$

reduces to

$$q_0 = \beta y - f_0^2 \frac{\partial}{\partial p}\left(\frac{1}{\sigma_r}\frac{dU(p)}{dp}y\right). \tag{2.2.44}$$

The background flow (2.2.43) corresponds to a vertically stratified zonal wind with no meridional shear.

The vorticity anomaly has the form

$$q_1 = \nabla^2 \psi_1 + f_0^2 \frac{\partial}{\partial p}\left(\frac{1}{\sigma_r}\frac{\partial \psi_1}{\partial p}\right). \qquad (2.2.45)$$

We assume that the eddy fields have the separable form

$$\psi_1 = \Psi(p)\tilde{\psi}(x,y), \qquad (2.2.46a)$$
$$q_1 = \Psi(p)\tilde{q}(x,y), \qquad (2.2.46b)$$

where $\Psi(p)$ is the vertical structure function. It turns out that this separation of variables leads to a horizontal solution $\tilde{\psi}(x,y)$ that is the same as the equivalent barotropic modon solution. This is so because the substitution of the separable solution (2.2.46) into (2.2.45) leads to

$$\tilde{q} = \nabla^2 \tilde{\psi} - k^2 \tilde{\psi}, \qquad (2.2.47)$$

in which

$$k^2 = -\frac{f_0^2}{\Psi(p)}\frac{d}{dp}\left(\frac{1}{\sigma_r}\frac{d\Psi}{dp}\right). \qquad (2.2.48)$$

Here k^2 corresponds precisely to a dimensional F, (or inverse deformation radius), as in the equivalent-barotropic equation (2.2.1). We proceed here toward the solution for the horizontal components; the vertical structure equation (2.2.48) is dealt with in section 2.3.

If we now re-write equation (2.2.41) in terms of the zonal and eddy components, we get

$$q_0 + q_1 = \mathcal{F}(\psi_0 + \psi_1). \qquad (2.2.49)$$

Substituting into this equation for ψ_0, q_0, q_1, and ψ_1 from (2.2.43), (2.2.44), (2.2.45), and (2.2.46), respectively, yields

$$y\frac{\partial q_0}{\partial y} + \tilde{q}\Psi(p) = \mathcal{F}(-U + \tilde{\psi}\Psi(p)), \qquad (2.2.50)$$

where we have used

$$\frac{\partial q_0}{\partial y} = \beta - f_0^2 \frac{\partial}{\partial p}\left(\frac{1}{\sigma_r}\frac{dU}{dp}\right). \qquad (2.2.51)$$

Next, substituting in (2.2.50) for $\tilde{q}$ from (2.2.47), we end up with

$$y\frac{\partial q_0}{\partial y} + [\nabla^2\psi - k^2\psi]\Psi(p) = \mathcal{F}(-Uy + \psi\Psi(p)). \qquad (2.2.52)$$

We now define a modon radius a, without initially having a fixed value for it. We require that on the exterior region, $r > a$, all streamlines extend to infinity, while in the interior region, $r < a$, they are all closed, where $r = (x^2+y^2)^{1/2}$.

Exterior region

In the exterior ($r > a$) we require the anomaly fields to vanish at great distance from the origin. For $r \gg a$, (2.2.52) reduces to:

$$\frac{\partial q_0}{\partial y} y = \mathcal{F}(-Uy)$$

so that in the far field $\mathcal{F}$ is a simple linear function. Substituting now for $\mathcal{F}$ into (2.2.52), and simplifying, yields

$$\nabla^2\psi - k^2\psi = -\frac{1}{U}\frac{\partial q_0}{\partial y}\psi.$$

Applying the chain rule to $\partial q_0/\partial y$, we get

$$\frac{\partial q_0}{\partial y} = \frac{dq_0}{d\psi_0}\frac{\partial \psi_0}{\partial y} = -U\frac{dq_0}{d\psi_0} \equiv -U\Lambda_0. \qquad (2.2.53)$$

Substituting (2.2.53) in for $\partial q_0/\partial y$, we get

$$\nabla^2\psi - [k^2 + \Lambda_0]\psi = 0, \quad \text{for} \quad r > a. \qquad (2.2.54)$$

A *bounded* exterior solution to (2.2.54) could consist of a linear combination of either J or K Bessel functions, depending on the sign of $k^2+\Lambda_0$. However, the J Bessel functions do not decay rapidly enough to satisfy the requirement that the

global kinetic energy

$$E_n = \int_{\mathbb{R}^2}\int (u^2+v^2)d\mathbb{R}^2 = \int_{\mathbb{R}^2}\int (\nabla\psi)^2 d\mathbb{R}^2$$

and global enstrophy

$$E_s = \frac{1}{2}\int_{\mathbb{R}^2}\int (u_y-v_x)^2 d\mathbb{R}^2 = \frac{1}{2}\int_{\mathbb{R}^2}\int (\nabla^2\psi)^2 d\mathbb{R}^2$$

both remain finite. Equivalent to this last requirement is the condition

$$\gamma^2 \equiv k^2 + \Lambda_0 > 0, \qquad (2.2.55)$$

which is the *modon existence condition* for a baroclinic system. This condition is sufficient to ensure that the exterior solutions consist of the K Bessel functions.

The modon existence condition excludes oscillatory solutions to (2.2.54), which means that there can be no Rossby wave solutions. To see how this can be, we re-write the existence condition, using the chain rule in (2.2.53), as

$$-\frac{\dfrac{\partial q_0}{\partial y}}{U} + k^2 > 0.$$

It is clear that this condition is satisfied for U lying in two ranges:

1. $U < 0$, corresponding to an easterly background flow. This is the only possibility for fully barotropic flows, for which k, or $F \to 0$.

2. $U > \dfrac{\dfrac{\partial q_0}{\partial y}}{k^2} \sim \dfrac{\beta}{k^2}$, which corresponds to a westerly flow.

We have assumed that the term $\partial q_0/\partial y > 0$. On average this is true in the mid-troposphere, and it is always satisfied if the zonal wind profile changes linearly with pressure, as can be easily verified using (2.2.51). The geostationary Rossby wave can

only exist in a westerly background flow. Therefore the first case clearly excludes Rossby waves. The Rossby wave's zonal phase speed is expressed (in dimensional units) as

$$c_x = -\frac{\beta}{\kappa^2 + \eta^2 + R_d^{-2}},$$

where κ and η are the zonal and meridional wavenumbers, respectively. R_d is a deformation radius (Pedlosky 1987, sec. 6.11); R_d^{-2} corresponds to the (non-dimensional) F of section (2.2.1). The maximum zonal wave speed (moving westward) is clearly

$$c_x = -\frac{\beta}{R_d^{-2}}.$$

This is also the maximum value (with opposite sign) of a westerly background flow U, in which a geostationary Rossby wave may exist. Recalling that k^2 and R_d^{-2} (or F) are essentially equivalent, we conclude that the allowable westward-moving modon speeds lie beyond the maximum permissible speed for stationary Rossby waves.

The general solution to (2.2.47) consists of modified (K) Bessel functions that decay exponentially with distance from the origin:

$$\psi = \sum_{n=0}^{\infty} [A_n \cos(n\theta) + B_n \sin(n\theta)]\, K_n(\gamma r).$$

Again $r = (x^2+y^2)^{1/2}$ and $\tan\theta = y/x$. The coefficients A_n and B_n will be determined by matching the exterior and interior solutions across the boundary r = a.

Interior region

In the interior (r < a), we now *assume* that the vorticity-stream-function relationship is also linear, i.e.

$$q = -\mu^2 \psi, \qquad (2.2.56)$$

in which μ is a real constant. The minus sign is chosen in order to be consistent with the observation that large-scale cyclonic (i.e. high) vorticity is invariably associated

with lows, and vice versa. This can be attributed to the geostrophic balance (Holton 1979), and another explanation given by Read et al. (1986) is presented in section 2.5. We substitute for q as before, which yields

$$y\frac{\partial q_0}{\partial y} + [\nabla^2\psi - k^2\psi]\Phi(p) = -\mu^2(-Uy + \psi\Phi(p)),$$

and after some re-arranging, we have

$$\nabla^2\psi + (\mu^2 - k^2)\psi = \frac{Uy}{\Phi(p)}[\mu^2 + \frac{dq_0}{d\psi_0}]. \qquad (2.2.57)$$

This is an inhomogeneous Helmholtz equation. In order for the solution to be finite at r = 0, the homogeneous part of the solution must be comprised of I or J Bessel functions, depending on the sign of the term μ^2 - k^2. However, to match up smoothly with the exterior K Bessel functions at r = a, it can only consist of J Bessel functions. This means that μ^2 - $k^2 > 0$. The general solution is then

$$\psi = \frac{Uy(\mu^2 + \Lambda_0)}{\Phi(p)\lambda^2} + \sum_{n=0}^{\infty}[C_n\cos(n\vartheta) + D_n\sin(n\vartheta)]\,J_n(\lambda r), \qquad (2.2.58)$$

where we have defined

$$\lambda^2 \equiv \mu^2 - k^2 > 0.$$

The definitions of γ and λ entail that

$$|\Lambda_0| < k^2 < |dq/d\psi|_{r<a}. \qquad (2.2.59)$$

Graphically, this means that the interior slope of the full solution, $dq/d\psi$, is steeper than the exterior slope Λ_0. This relation also provides a range of allowed values for k^2. The coefficients of the sines and cosines in (2.2.57) are determined by applying the boundary condition of continuous vorticity across r = a.

Continuity of vorticity across r = a

We desire a solution for which q is continuous across r = a. Our two linear vorticity-stream-function relationships are

$$q = \Lambda_0\psi = \Lambda_0(\psi_0 + \psi_1), \quad r > a, \text{ and}$$
$$q = -\mu^2\psi = -\mu^2(\psi_0 + \psi_1), \quad r < a.$$

The difference between these must vanish as $r \to a^{\pm}$, i.e.

$$\lim_{r \to a^{\pm}} (\mu^2 + \Lambda_0)(\psi_0 + \psi_1) = 0.$$

This will be satisfied if we set $\psi_0 + \psi_1 = 0$, on the modon radius $r = a$, for both the interior and exterior solutions. Then for the exterior, we will have

$$\psi_0 + \psi_1 = -Uy + \Psi\psi = 0, \quad r \to a^+,$$

or

$$-Ua \sin\vartheta + \Psi B_1 \sin\vartheta K_1(\mu r) = 0,$$

where we see that, out of the infinite series, only the coefficient B_1 is non-zero, while the rest of the coefficients vanish, due to the linear independence properties of the sines and cosines. We have, therefore,

$$B_1 = \frac{U(p)a}{\Psi(p)K_1(\gamma a)},$$

so that our exterior solution is complete.

The same limiting procedure is then followed for the interior:

$$\psi_0 + \psi_1 = -Uy + \Psi\psi = 0, \quad r \to a^-,$$

or

$$-Ua \sin\vartheta + \Psi D_1 \sin\vartheta J_1(\lambda r)(\mu^2 + \Lambda_0)/\lambda^2 = 0,$$

where again the only non-vanishing coefficient in the series is D_1, which we find is

$$D_1 = -\frac{U(p)a(k^2 + \Lambda_0)}{\Psi(p)\lambda^2 J_1(\lambda a)}.$$

The solution for the eddy component of stream-function is thus

$$\psi_1 = \frac{U(p)\,a\,K_1(\gamma r)\sin\theta}{K_1(\gamma a)}, \quad r > a, \tag{2.2.60a}$$

$$\psi_1 = -\frac{U(p)\,a(k^2+\Lambda_0)J_1(\lambda r)\sin\theta}{\lambda^2 J_1(\lambda a)} + \frac{U(p)(\mu^2+\Lambda_0)r\sin\theta}{\lambda^2}, \quad r < a. \tag{2.2.60b}$$

Adding on the background stream-function (2.2.43) gives us the full solution:

$$\psi = U(p)\left[\, a\frac{K_1(\gamma r)}{K_1(\gamma a)} - r \,\right]\sin\theta, \quad r > a, \tag{2.2.61a}$$

$$\psi = U(p)\frac{(k^2+\Lambda_0)}{\lambda^2}\left[\, r - a\frac{J_1(\lambda r)}{J_1(\lambda a)}\right]\sin\theta, \quad r < a. \tag{2.2.61b}$$

Our modon wavenumbers are

$$\gamma^2 = k^2 + \Lambda_0,$$

and

$$\lambda^2 = \mu^2 - k^2,$$

where $\Lambda_0 = dq_0/d\psi_0$ (for $r > a$), $\mu^2 = -dq/d\psi$ (for $r < a$), and k^2 is defined in (2.2.48).

Dispersion relationship

The second boundary condition at $r = a$ is that the velocity be continuous. This is equivalent to requiring continuity of $\nabla\psi_1 = (\partial_r, r^{-1}\partial_\theta)\,\psi_1$, i.e.

$$\nabla\psi_1|_{r\to a+} = \nabla\psi_1|_{r\to a-}$$

Because ψ_1 is continuous across $r = a$, it follows that $\partial_\vartheta \psi_1$ is continuous across $r = a$. Thus continuity of velocity is ensured if $\partial_r \psi_1$ is continuous across $r = a$. Application of this condition to (2.2.60) leads to

$$\frac{Ua}{K_1(\gamma a)}\left[\gamma K_1'(\gamma a)\sin\vartheta + \frac{K_1(\gamma a)}{a}\cos\vartheta\right] = -\frac{Ua(k^2+\Lambda_0)}{\lambda^2 J_1(\lambda a)}\left[\lambda J_1'(\lambda a)\sin\vartheta + \frac{J_1(\lambda a)}{a}\cos\vartheta\right] + \frac{U(\mu^2+\Lambda_0)}{\lambda^2}[\sin\vartheta + \cos\vartheta],$$

where primes denote derivatives with respect to the argument. Grouping the cosine terms and simplifying, we get the trivial result $U = U$, indicating that the background zonal wind is the same over the entire domain.

Grouping the sine terms gives us

$$\frac{Ua\gamma}{K_1(\gamma a)}K_1'(\gamma a) = -\frac{Ua(k^2+\Lambda_0)}{\lambda J_1(\lambda a)}J_1'(\lambda a) + \frac{U(\mu^2+\Lambda_0)}{\lambda^2}.$$

The derivatives can be eliminated by using the following well-known recurrence relations for the Bessel functions:

$$xJ_1'(x) = J_1(x) - xJ_2(x),$$
$$xK_1'(x) = K_1(x) - xK_2(x).$$

After substituting for the derivatives and cancelling out several terms, we are left with

$$-\frac{\gamma K_2(\gamma a)}{K_1(\gamma a)} = \frac{(k^2+\Lambda_0)J_2(\lambda a)}{\lambda J_1(\lambda a)}.$$

Recalling that $\gamma^2 = k^2 + \Lambda_0$, we divide by γ^2 to get

$$-\frac{K_2(\gamma a)}{\gamma K_1(\gamma a)} = \frac{J_2(\lambda a)}{\lambda J_1(\lambda a)}. \qquad (2.2.62)$$

This is the *modon dispersion relationship*.

2.3 The solution to the vertical structure problem

The vertical structure equation (2.2.48) arose from the separation of variables procedure. We wish to solve for the function $\Psi(p)$, and the number k, which together satisfy the equation

$$\frac{d}{dp}\left[\frac{1}{\sigma_r}\frac{d\Psi}{dp}\right] + \frac{k^2}{f_0^2}\Psi = 0. \tag{2.3.1}$$

We need to impose an upper and a lower boundary condition. Both upper and lower boundaries are isobaric surfaces, on which we specify zero vertical velocity, allowing variable geopotential height. The derivation proceeds as in Malguzzi and Malanotte-Rizzoli (1984).

In the quasi-geostrophic stationary case, the isentropic, source-free thermodynamic equation (2.2.31) can be written

$$J(\psi, \partial\psi/\partial p) + f_0\sigma_r\omega = 0,$$

in which ω is the vertical velocity in isobaric coordinates. Our condition of zero vertical velocity results in

$$J(\psi, \partial\psi/\partial p) = 0.$$

This is equivalent to

$$\partial\psi/\partial p = f(\psi),$$

in which f is some function, the form of which we determine by invoking the far-field condition, as in section 2.2.2. We recall that ψ is the departure from the reference state, and is assumed to be composed of a zonal background, and eddy component, each of which is separable, thus

$$\psi = \psi(x,y,p) = -U(p)y + \Psi(p)\psi(x,y).$$

Substituting for $\partial\psi/\partial p$ and ψ in the equation for f, yields

$$-\frac{dU(p)}{dp}y + \frac{d\Psi(p)}{dp}\psi(x,y) = f(-U(p)y + \Psi(p)\psi(x,y)).$$

We apply the far-field condition, namely that $\psi \to 0$, as $x^2 + y^2 \to \infty$, which leaves

$$(\partial U/\partial p)\, y = f(-U(p)\, y).$$

This fixes the form of f as a linear function of its argument, as in section 2.2.3, so we have

$$\frac{\partial\psi}{\partial p} = \frac{dU/dp}{U}\psi.$$

It follows that

$$\frac{d\Psi}{dp} - \frac{dU(p)/dp}{U(p)}\Psi = 0, \qquad (2.3.2)$$

which is our boundary condition for both the upper and lower boundaries.

We now have a two-point eigenvalue problem of Sturm-Liouville type. For such problems, the Sturm-Liouville theory guarantees an infinite sequence of k_n, for n = 0, 1, 2, ..., such that $0 \le k_0 < k_1 < k_2 < \ldots$ (Zauderer 1989). Every eigenvalue k_n is associated with an eigenfunction Ψ_n, each pair of which satisfies the boundary-value problem (2.3.1), (2.3.2). It can be shown that for problems such as ours, we cannot have $k_0 = 0$ (Zauderer 1989), which means that the eddy field ψ_1 in our continuously stratified model does not contain a purely barotropic mode.

Deriving the eigenvalues $k_n > 0$.

To make any headway we have to settle on an equation for $\sigma_r(p)$. Below the tropopause, and neglecting the planetary boundary layer, σ_r can be reasonably well-approximated by a power-law,

$$\sigma_r \approx A\, p^b. \qquad (2.3.3)$$

In order to get an estimate of the constants A and b, we first compute a least-squares power-law. From our data set, we compute values of σ_r at 4 levels (775, 600, 450, and 325 mb), using centred finite differences, on all 28 days of February 1989. The daily area-average over the grid of virtual potential temperature is used as the reference potential temperature, θ_r. We obtained A = 397.9 and b = -1.711, in S.I units. The correlation coefficient for this least-squares fit to our data was quite high: ϱ = 0.947. It is interesting to note that b = -2 exactly is equivalent to an isothermal atmosphere (Holton, 1979).

We can also demonstrate a physical justification for the power law (2.3.3). For a hydrostatic atmosphere in which the reference lapse rate $\Gamma \equiv -dT_r/dz$ is constant, it is straightforward to show that

$$\sigma_r = \left[\frac{1}{c_p} - \frac{\Gamma}{g}\right] \frac{R^2 \theta_r}{p_0^{R/c_p}} \, p^{-2+R/c_p}, \qquad (2.3.4)$$

where we have also assumed that the reference potential temperature θ_r is approximately constant, or at least varies slowly with pressure. This assumption is reasonable in our case. The weighted vertical average of θ_r is 300K, and the value of θ_r at any pressure level departs from this vertical average by no more than 10%. R/c_p = 0.286 is the ratio of the gas constant to the specific heat at constant pressure, for dry air, and the exponent in the power law for the constant lapse-rate atmosphere is therefore b = -1.714, which is very close to our least-squares estimate. From our data, we once again use the grid area-average of the virtual potential temperature as the reference potential temperature θ_r, from which we calculate an estimate of the constant lapse rate Γ. This enables us to compute a range of values for A:

$$0 < A \leq 426;$$

the means by which this is accomplished is described in section 3.6.

Substituting for σ_r in (2.3.1) using the power law (2.3.3), we can write our vertical structure equation as

$$\frac{d}{dp}\left[p^{-b}\frac{d\Psi}{dp}\right] + \frac{Ak^2}{f_0^2}\Psi = 0, \tag{2.3.5}$$

with the same boundary condition (2.3.2).

Close scrutiny of (2.3.5) reveals that it is one of the many varied forms of Bessel's differential equation (Hildebrand, 1976); in this instance the general solution is

$$\Psi(p) = p^{\frac{1+b}{2}} Z_{\frac{1+b}{2+b}}\left(\frac{\sqrt{A}\,k}{f_0}\frac{1}{1+b/2}p^{1+b/2}\right), \tag{2.3.6}$$

where Z_ν signifies an ordinary Bessel function of either the first or second kind (J or Y, respectively) of order ν. The choice of Bessel function is dictated by the index of Z_ν in (2.3.6),

$$\nu = \frac{1+b}{2+b}.$$

If the index ν is a positive integer, then the complete general solution will be a linear combination of the J and Y Bessel functions of integer order. Otherwise the solution consists of a combination of the J Bessel functions of order $\pm\nu$. In our case, the exponent b in the power law (2.3.3) is

$$b = -2+\frac{R}{c_p} = -2+\epsilon = -1.714.$$

This leads to an index

$$\nu = 1-\frac{1}{\epsilon} = -2.501,$$

and our general solution to (2.3.5) is therefore

$$\Psi(p) = p^{\frac{\epsilon-1}{2}}\left[c_1 J_{1/\epsilon-1}\left(\frac{2k\sqrt{A}}{\epsilon f_0}p^{\epsilon/2}\right) + c_2 J_{1-1/\epsilon}\left(\frac{2k\sqrt{A}}{\epsilon f_0}p^{\epsilon/2}\right)\right]. \qquad (2.3.7)$$

$J_{1/\epsilon-1}$ and $J_{1-1/\epsilon}$ are the (linearly independent) Bessel functions of order $\pm(1-1/\epsilon)$ of the first kind. The constants c_1 and c_2 are undetermined at this point.

We set them by applying the boundary condition, by substituting the general solution (2.3.8) into (2.3.2). Upon implementing the following Bessel function identities

$$\frac{d}{dx}Z_\nu(x) = Z_{\nu-1}(x) - \frac{\nu}{x}Z_\nu(x),$$
$$\frac{d}{dx}Z_\nu(x) = \frac{\nu}{x}Z_\nu(x) - Z_{\nu+1}(x),$$

several terms merge or are cancelled, leaving for the lower boundary

$$c_1\left[-\frac{\epsilon}{2}\alpha_b k J_{1/\epsilon-2}(\alpha_b k) + \left(1 - \epsilon + p_b\frac{U'(p_b)}{U(p_b)}\right)J_{1/\epsilon-1}(\alpha_b k)\right]$$
$$+ c_2\left[\frac{\epsilon}{2}\alpha_b k J_{2-1/\epsilon}(\alpha_b k) + \left(1 - \epsilon + p_b\frac{U'(p_b)}{U(p_b)}\right)J_{1-1/\epsilon}(\alpha_b k)\right] = 0, \qquad (2.3.8)$$

where

$$\alpha_b = \frac{2\sqrt{A}}{\epsilon f_0}p_b^{\epsilon/2}.$$

The same equation is obtained for the upper boundary, $p = p_t$,

$$c_1\left[-\frac{\epsilon}{2}\alpha_t k J_{1/\epsilon-2}(\alpha_t k) + \left(1 - \epsilon + p_t\frac{U'(p_t)}{U(p_t)}\right)J_{1/\epsilon-1}(\alpha_t k)\right]$$
$$+ c_2\left[\frac{\epsilon}{2}\alpha_t k J_{2-1/\epsilon}(\alpha_t k) + \left(1 - \epsilon + p_t\frac{U'(p_t)}{U(p_t)}\right)J_{1-1/\epsilon}(\alpha_t k)\right] = 0, \qquad (2.3.9)$$

where

$$\alpha_t = \frac{2\sqrt{A}}{\epsilon f_0} p_t^{\epsilon/2}.$$

This pair of equations, (2.3.8) and (2.3.9), can only be satisfied if the determinant of the coefficients of c_1 and c_2 vanishes, that is, if

$$\left[\frac{\epsilon}{2}\alpha_b k J_{1/\epsilon-2}(\alpha_b k) - \left(1 - \epsilon + p_b \frac{U'(p_b)}{U(p_b)}\right) J_{1/\epsilon-1}(\alpha_b k)\right]$$
$$\cdot\left[\frac{\epsilon}{2}\alpha_t k J_{2-1/\epsilon}(\alpha_t k) + \left(1 - \epsilon + p_t \frac{U'(p_t)}{U(p_t)}\right) J_{1-1/\epsilon}(\alpha_t k)\right]$$

$$-\left[\frac{\epsilon}{2}\alpha_b k J_{2-1/\epsilon}(\alpha_b k) + \left(1 - \epsilon + p_b \frac{U'(p_b)}{U(p_b)}\right) J_{1-1/\epsilon}(\alpha_b k)\right]$$
$$\cdot\left[\frac{\epsilon}{2}\alpha_t k J_{1/\epsilon-2}(\alpha_t k) - \left(1 - \epsilon + p_t \frac{U'(p_t)}{U(p_t)}\right) J_{1/\epsilon-1}(\alpha_t k)\right] = 0. \tag{2.3.10}$$

This is a single equation that can be solved numerically for k. Although we are guaranteed an infinite sequence of k_n, for n = 0, 1, 2, ..., in our case we are interested only in the lowest few modes, for $n \leq 3$. For each eigenvalue, k_n we can calculate an eigenfunction $\Psi_n(p)$, using (2.3.7). In our calculation, we can set one constant, $c_1 = -1$, and then c_2 can be defined by using, say, the upper boundary condition (2.3.9).

The functions $\Psi_n(p)$ are useful because they can be utilized to discover how the baroclinicity changes over time. It has been proven in many textbooks on differential equations (e.g. Zauderer 1989) that, for any Sturm-Liouville problem, such as ours, the eigenfunctions solving it are mutually orthogonal, and are basis functions within the boundaries. For our purposes, this means that any physically-relevant function of pressure may be written as a generalized Fourier series, with the eigenfunctions, or normal modes, taking the place of the more familiar sines and cosines.

Our method will be to discretize the first four eigenfunctions, by computing their values at a number of pressure levels. The discretization enables us to then numerically compute the integrals required for determining the coefficients in the Fourier series. We also need to orthonormalize the eigenfunctions, which is readily accomplished using the Gram-Schmidt procedure (Arfken, 1985) as follows.

The gravest eigenfunction $\Psi_0(p)$, is first normalized:

$$\Psi_0(p) \leftarrow \frac{\Psi_0(p)}{\left[\frac{1}{\Delta p}\int[\Psi_0(p)]^2 dp\right]^{1/2}},$$

in which $\Delta p = p_b - p_t$. The integrals in the remainder of this section are all evaluated between p_b and p_t. The next eigenfunction, Ψ_1, is made orthogonal to Ψ_0 by subtracting from Ψ_1 its projection onto Ψ_0, thus

$$\Psi_1(p) \leftarrow \Psi_1(p) - \Psi_0(p)\left[\frac{1}{\Delta p}\int \Psi_0(p)\,\Psi_1(p)\,dp\right],$$

after which it is normalized in the same manner as Ψ_0:

$$\Psi_1(p) \leftarrow \frac{\Psi_1(p)}{\left[\frac{1}{\Delta p}\int[\Psi_1(p)]^2 dp\right]^{1/2}}.$$

Ψ_2 is next made orthogonal to both Ψ_0 and Ψ_1 by subtracting from it the projections of each of Ψ_0 and Ψ_1 onto Ψ_2:

$$\Psi_2(p) \leftarrow \Psi_2(p) - \Psi_0(p)\left[\frac{1}{\Delta p}\int \Psi_0(p)\,\Psi_2(p)\,dp\right] - \Psi_1(p)\left[\frac{1}{\Delta p}\int \Psi_1(p)\,\Psi_2(p)\,dp\right],$$

after which it, too, is normalized in the same way as Ψ_0 and Ψ_1. This procedure can clearly be continued to any number of eigenfunctions; in our case we shall only require the first four.

For the representative vertical structure quantity, we use the eddy stream-function over the blocking region, which we estimate by subtracting from the observed

geostrophic stream-function a hydrostatic reference field, and an estimated zonal background field. Although this calculation is only done at the five data-levels, the eddy field is assumed to vary smoothly enough in the vertical, that it may be linearly interpolated at a number of intermediate levels. One set of the generalized Fourier coefficients can then be computed from the column of stream-function values at each horizontal grid-point.

The average magnitude of each coefficient in our generalized Fourier series is a measure of the contribution to the vertical structure by the corresponding mode. For example, in a highly baroclinic situation with a great deal of vertical variation, we would expect the coefficients of the higher modes to be greater than they would be in a less baroclinic flow. We follow Holmström (1963) and use the root-mean-square values of each Fourier coefficient over the blocking region, as the average.

2.4 Scatter diagrams

Free mode flows, in which $q = q(\psi)$, can be detected by plotting stream-function versus vorticity scatter diagrams, using values of ψ and q calculated at grid points. In the case of the modon, the $q(\psi)$ relation is linear and multi-valued. This distinguishes the modon from other free modes. For instance, the solitary wave, or soliton solution, a free mode studied extensively by Malguzzi and Malanotte-Rizzoli (1984), has an analytic $q(\psi)$ relation, which need not be linear. They found that $\Lambda_0 \equiv dq_0/d\psi_0$ is negative for a stable solitary wave. More recently, Haines and Malanotte-Rizzoli (1991) have discovered in a numerical model that the sign of the curvature $d^2q_0/d\psi_0^2$ distinguished blocking (split-jet) from intense jet flow-types (see our Figure 4.2.1). We do not pursue this aspect of the $q(\psi)$ relation, except to note that visual inspection of our scatter plots does not appear to confirm this result.

Since we have hypothesized that our block is a localized structure, we follow the lead of Butchart et al. (1989), and distinguish between (ψ,q) values from inside and outside the blocking region. After some experimentation, we have chosen a simple fixed box-shape as the boundary between the interior and exterior. The box edges are latitudes 46° and 70° N, and longitudes 114° and 166° W. The values of (ψ,q) from within this region have been plotted using crosses, while the exterior region's

values are represented by dots (Appendix A2).

2.5 Slope and area of the q(ψ) plot

In addition to the qualitative interpretation of the diagrams, the analysis of section 2.2.3 provides us with a method to quantitatively test the applicability of the modon free mode model to this block. First, we can test the modon existence condition, (2.2.55). We estimate the slopes $dq/d\psi$ for the interior and exterior regions using the method of least squares. We must also have a value for at least one vertical structure eigenvalue, k, satisfying (2.2.59), i.e.

$$|dq/d\psi|_{exterior} < k^2 < |dq/d\psi|_{interior}.$$

We can then use values that do satisfy this inequality to formally compute a modon radius, using the dispersion relation (2.2.62). If the modon model is applicable to this block, we would expect to calculate a radius that is reasonably close to the real dimensions of the block, during the dipole stage around February 18.

Another, more general means of testing the applicability of free modes to blocking originates with an interesting result of Read et al. (1986). This relates the area of a q(ψ) scatter plot and the degree to which the system departs from *any quasi-geostrophic* free mode. Suppose that we pick an arbitrary, simple, horizontal curve enclosing a region $\Re_{(x,y)}$, in (x,y) space. The net flux of vorticity across the curve, $\partial\Re_{(x,y)}$, due to the geostrophic wind, can be written as

$$F_q \equiv \oint_{\partial\Re_{(x,y)}} q\vec{v}_g \cdot \hat{n}\, dl, \qquad (2.5.1)$$

where

$\vec{v}_g \equiv \hat{k} \times \nabla\psi$ is the geostrophic wind,

$\hat{n}$ is the outward unit normal vector to the curve $\partial\Re_{(x,y)}$,

and dl is the differential arc-length.

We can apply the two-dimensional divergence theorem to (2.5.1) to get

$$F_q = \int_{\mathfrak{R}} \int_{(x,y)} \nabla\cdot[q(\hat{k}\times\nabla\psi)]dx\,dy = \int_{\mathfrak{R}} \int_{(x,y)} J(\psi,q)\,dx\,dy. \qquad (2.5.2)$$

From elementary calculus we know that the second integral in (2.5.2) may be directly transformed into an integral over the corresponding region $\mathfrak{R}_{(\psi,q)}$, in (ψ,q) space, so that

$$F_q = \int_{\mathfrak{R}} \int_{(\psi,q)} \text{sign}[J(\psi,q)]\,d\psi dq. \qquad (2.5.3)$$

The sign of the Jacobian is positive, if the curve in (ψ,q) space is closed off in the same sense as the corresponding (x,y) space curve, which we take to be counter-clockwise. The sign is negative for (ψ,q) curves that are closed off in the clockwise sense. Hence we see that the net geostrophic flux of vorticity across the curve in physical (x,y) space is equal to the net area of the corresponding region in (ψ,q) space. In the case of a free mode defined by $q = q(\psi)$, we have $J(\psi,q) = 0$, and the area of the (ψ,q) region, and F_q must both vanish. It is evident that either of the two quantities, F_q or the (ψ,q) area, may be thought of as a measure of the *departure* of the system from *any* free mode of the form $q = q(\psi)$.

Because the computation of the (ψ,q) space integral in (2.5.3), using actual data, seems to be difficult, Read et al. (1986) proposed the use of

$$I \equiv \frac{\textit{area enclosed on the } q(\psi) \textit{ plot}}{\textit{area of the circumscribing rectangle}}$$

as a measure of the degree to which the system departs from a free mode form. Calculating the quantity I, however, is also a non-trivial task. The area of the circumscribing rectangle can vary, depending on its orientation. Choosing the proper orientation for the rectangle is in turn difficult because the slope of the scatter plot changes over time.

We compute both the line integral in (2.5.1) and the (ψ,q) space area integral of (2.5.3), using a method described in section 3.5. We can then compare the two, in order to ascertain whether we can detect free-mode behaviour during this blocking episode. If we find that the two quantities are well-correlated, we can conclude that the result (2.5.3) is practical to compute. We also hope to find a correlation between the blocking flow-pattern and the area of the $q(\psi)$ plot, that can indicate whether or

not a free mode is being approached.

Another result of Read et al. (1986) is useful in explaining the observed negative slopes of published scatter diagrams. We have mentioned in section 2.2.2 the observation (over the northern hemisphere) that large-scale cyclonic vorticity is invariably associated with lows, and anticyclonic vorticity with highs, which means $dq/d\psi < 0$. If we include a vorticity source of strength S, and synoptic-scale eddy transport of vorticity with constant eddy diffusivity K, the steady quasi-geostrophic vorticity equation can be written

$$J(\psi,q) = S + K\nabla^2 q. \tag{2.5.4}$$

Integrating both sides of (2.5.4) over the area $\mathcal{A}_\Psi$ enclosed by a mean streamline Ψ, and applying the divergence theorem, we get

$$-K\oint_\Psi \nabla q \cdot \hat{n}\, dl = \iint_{\mathcal{A}_\Psi} S\, dx\, dy. \tag{2.5.5}$$

If we assume that (2.5.4) has the approximate, free mode solution $q = q(\psi)$, then $\nabla q = dq/d\psi \cdot \nabla\psi$, and, along our mean streamline Ψ, $dq/d\psi$ is constant, and so can be taken outside the first integral of (2.5.5). This gives the result

$$\frac{dq}{d\psi} = -\frac{\iint_{\mathcal{A}_\Psi} S\, dx\, dy}{K\oint_\Psi \nabla \cdot d\Gamma}. \tag{2.5.6}$$

This explains, why, in general, observed scatter plot slopes are always negative. The circulation, in the denominator of (2.5.6), will usually have the same sign as the net vorticity source/sink term in the numerator, for time-independent flows. Another heuristic argument for the observed negative slopes is that the stream-function field is roughly sinusoidal (in the two horizontal dimensions), so that

$$\nabla^2\psi \propto -\psi.$$

If the relative vorticity, $\nabla^2\psi$, is the dominant component of the potential vorticity, then we should expect $dq/d\psi < 0$.

Chapter 3
Computations

3.1 Data Preparation

The data (supplied by the Canadian Meterological Centre) consist of objectively-analyzed archived data on a latitude-longitude grid, at a two-degree spacing. The full grid extends from 30°N to 90°N and westward from 20°W to 120°E (Figure 3.1.1). Five levels are used: 850, 700, 500, 400, and 250 mb. At each level, 3 data fields were used:

i. Z, the geopotential height of the pressure surface;
ii. T, the temperature;
iii. $T-T_d$, the dew-point depression.

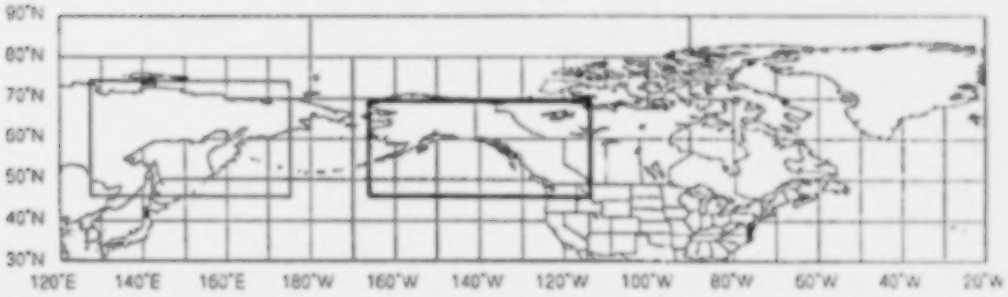

Figure 3.1.1 The region covered by the data grid. The box over the Gulf of Alaska approximates the block's interior. The box over Northeast Asia encompasses another feature discussed in Chapter 4.

There are normally four data-sets for each day (one for every synoptic hour), running for 39 days from 21 January to 28 February, 1989. The initial preparation consists of time-averaging (at each grid point) the 3 data fields, over the four synoptic periods per day. This smooths out the smallest-scale disturbances.

3.2 Calculation of stream-function and vorticity

In this section the approximations to the variables appearing in (2.2.39) and (2.2.40) are presented. We have used the geostrophic stream-function, calculated at each grid point (i,j) as $\psi_{i,j} = f_0^{-1} g Z_{i,j}$, where f_0 is the Coriolis parameter at 60°N, g is

the gravitational acceleration, and $Z_{i,j}$ is the geopotential height of the isobaric surface. The grid point (i,j) is i points north and j points east from the southwest corner of the grid. We remark that although the results of our analysis in Chapter 2 apply to the *departure* from the reference fields, we only subtract out a reference field if we are taking vertical derivatives. Horizontal derivatives (i.e. taken on an isobaric surface) are independent of the reference components, which are functions of pressure only.

The vertical component of absolute vorticity was calculated as $\nabla^2\Psi_{i,j} + f$, using the following centred finite differences for the Laplacian term:

$$\nabla^2\Psi_{i,j} \approx \frac{\Psi_{i,j+1} + \Psi_{i,j-1} - 2\Psi_{i,j}}{\delta x_i^{\,2}} + \frac{\Psi_{i+1,j} + \Psi_{i-1,j} - 2\Psi_{i,j}}{\delta y^2} \qquad (3.2.1)$$

Values of vorticity are not computed for the points on the edge of the grid. The zonal grid-length δx_i is a function of the latitude and so must be accounted for in the differencing scheme. The vertical component of the planetary vorticity, f, is calculated exactly, so that we are departing from the β-plane approximation. This is done for the sake of convenience, and also takes into account the fairly broad latitude band covered by the data set. The difference in computed q and ζ_a from β-plane values is less than 5%, which is insignificant for our purposes.

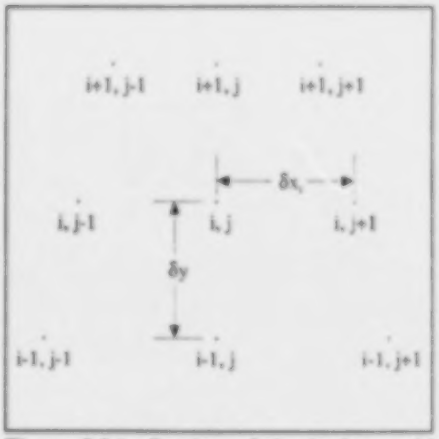

Figure 3.2.1 Portion of the lat-long grid with variable zonal grid-spacing δx_i.

While this choice of stream-function and method of calculating vorticity would be error-prone for eddy flux calculations (Illari 1984), it certainly appears to be adequate for our study. First, we do not compute any derivatives that are higher than second order. Secondly, we are primarily interested in large-scale motions, so we can smooth out most of the numerical error resulting from the finite differencing.

The calculation of q requires an extra term, the baroclinic stretching term. In

order to make use of as many of the different data fields as possible, we do not compute it as in our initial definition (2.2.40), but we follow the technique of Hoskins et al. (1985), as follows. We emphasize that $\psi = \psi(x,y,p)$ in (2.2.40a) is really the dynamic anomaly, or departure from the reference field $\psi_r(p)$. From our definition $\psi = gZ/f_0 = \phi/f_0$, we can re-write the extra term as

$$f_0^2 \frac{\partial}{\partial p}\left(\frac{1}{\sigma_r}\frac{\partial \psi}{\partial p}\right) = f_0 \frac{\partial}{\partial p}\left(\frac{1}{\sigma_r}\frac{\partial \phi^*}{\partial p}\right),$$

where ϕ^* is the departure from the reference geopotential, as in (2.2.16). Applying the hydrostatic equation to ϕ^*, substituting for density using the ideal gas law and potential temperature definition, this becomes

$$f_0 \frac{\partial}{\partial p}\left(\frac{1}{\sigma_r}\frac{-1}{\rho^*}\right) = f_0 \frac{\partial}{\partial p}\left[\left(-\frac{\rho_r \theta_r}{d\theta_r/dp}\right)\frac{-R\theta^*}{p}\left(\frac{p}{p_0}\right)^{R/c_p}\right] = f_0 \frac{\partial}{\partial p}\left[\frac{\rho_r T_r R}{p}\frac{\theta^*}{d\theta_r/dp}\right].$$

The ideal gas law can be written in terms of reference and departure quantities as

$$p = \rho RT = (\rho_r + \rho^*)R(T_r + T^*),$$

and since $\rho^* \ll \rho_r$ and $T_r \ll T^*$, it follows that the baroclinic stretching term can be well-approximated by

$$f_0 \frac{\partial}{\partial p}\left(\frac{\theta^*}{d\theta_r/dp}\right).$$

We approximate the reference field θ_r by the area average on the isobaric surface, over the entire domain, so that θ^* is the local deviation from the area mean, i.e.

$$\theta^*(x,y,p) = \theta(x,y,p) - \theta_r(p).$$

The full expression for the baroclinic, quasi-geostrophic potential vorticity is thus

$$q = \zeta_a + f_0 \frac{\partial}{\partial p}\left(\frac{\theta^*}{d\theta_r/dp}\right). \qquad (3.2.2)$$

Since we are dealing with a fairly thick layer in the troposphere, it is quite likely that considerable moisture is present over large regions of our grid, especially over the southern latitudes. Visual inspection of satellite images for this period confirms this. To take this into account, we make use of the available dew point data, and employed the virtual potential temperature (Iribarne and Godson 1981). This is based on the virtual temperature, defined as the temperature of dry air having the same density as air of a given humidity, at the same pressure. Moist air is less dense than dry air, so that the virtual temperature of moist air is greater than the dry-bulb temperature.

The importance of including the effect of moisture is apparent if we note that, in our analysis of the vertical structure, in section 2.3, the vertical static stability, σ_r, plays an important role. In the atmosphere σ_r is influenced considerably by the moisture content of the air (Iribarne and Godson 1981). However we do not investigate the degree to which our results are improved by the inclusion of moisture data.

The virtual potential temperature is computed as:

$$\theta_v = T_v\,(10^5/p)^{0.286}, \qquad (3.2.3)$$

where the pressure p is in Pascals. T_v is computed as follows. The vapour pressure e_v is computed from the dew point temperature by means of Magnus' approximation to the Clausius-Clapeyron equation (Iribarne and Godson 1981, p.68). From this, the specific humidity is derived as

$$q = \frac{1}{1 + \dfrac{p}{0.622\ e_v}}, \qquad (3.2.4)$$

and the virtual temperature is then approximately

$$T_v = T\,(1 + 0.61q). \tag{3.2.5}$$

The vertical (p) derivatives in (3.2.2) are approximated by centred finite differences. The θ^* term is approximated at the two intermediate levels (1.5 and 2.5 in Figure 3.2.2) by

$$\theta^*_{2.5} = \tfrac{1}{2}(\,\theta_3 - \overline{\theta}_3 + \theta_2 - \overline{\theta}_2\,) \tag{3.2.6a}$$
$$\theta^*_{1.5} = \tfrac{1}{2}(\,\theta_2 - \overline{\theta}_2 + \theta_1 - \overline{\theta}_1\,), \tag{3.2.6b}$$

where $\overline{\theta}_i$ is the area mean value of θ at pressure level i. The term $d\theta_r/dp$ in equation (3.2.2) is approximated at the two intermediate levels by

$$(\delta\overline{\theta}/\delta p)_{2.5} = (\overline{\theta}_3 - \overline{\theta}_2)/(p_3 - p_2) \tag{3.2.7a}$$
$$(\delta\overline{\theta}/\delta p)_{1.5} = (\overline{\theta}_2 - \overline{\theta}_1)/(p_2 - p_1). \tag{3.2.7b}$$

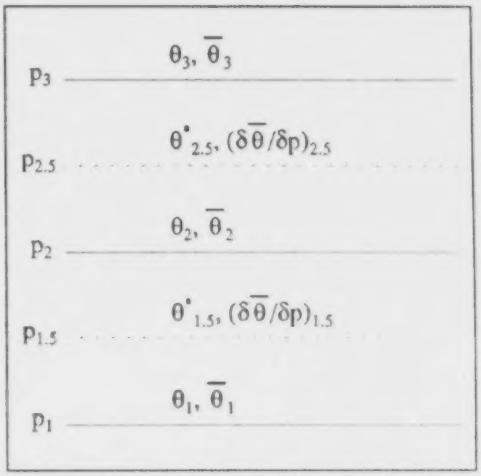

Figure 3.2.2 Vertical differencing scheme showing levels at which the intermediate differences are calculated

The pressure difference between the two intermediate levels, δp_2, is found to be

$$\delta p_2 = \tfrac{1}{2}\,(\,p_3 - p_1\,). \tag{3.2.8}$$

With the differences computed at the intermediate levels, we approximate the second p-derivative in (3.2.2) by

$$\frac{\partial}{\partial p}\left(\frac{\theta^*}{d\theta_r/dp}\right) \approx \frac{\dfrac{\theta^*_{2.5}}{\left(\dfrac{\delta\overline{\theta}}{\delta p}\right)_{2.5}} - \dfrac{\theta^*_{1.5}}{\left(\dfrac{\delta\overline{\theta}}{\delta p}\right)_{1.5}}}{\delta p_2}. \tag{3.2.9}$$

As an example, to calculate q at p_2 = 500 mb, we use the following pressure levels:

p_1 = 700 mb,
$p_{1.5}$ = 600 mb,
$p_{2.5}$ = 450 mb,
p_3 = 400 mb.

3.3 Smoothing

Geostrophic stream-function, absolute vorticity and potential vorticity fields are computed using the 24-hour mean data. Horizontal (spatial) and then temporal smoothing are then applied to these derived fields. We have found that contours of the unsmoothed fields, especially vorticity, are jagged, especially at latitudes greater than 80°N, where the zonal grid-length decreases considerably. This indicates that the horizontal finite-difference Laplacian operator is the cause. To avoid this, we have set the northern boundary of our data grid at 80°N.

A simple 5-point spatial smoothing operator has been applied to the stream-function arrays before calculating vorticity. Smoothing is performed on the absolute vorticity, and again after the addition of the baroclinic term. The spatial smoother is modified to incorporate the variable grid distance. At each application of the operator, neighbouring points are weighted according to their distance from the central point. For an array $f_{i,j}$, this smoothing operator is defined as

$$\tilde{f}_{i,j} = \frac{1}{s+1}\left\{ f_{i,j} + \frac{s}{2}\left[\frac{\delta x_i^{\,2}}{\delta x_i^{\,2} + \delta y^{\,2}}\left(f_{i-1,j} + f_{i+1,j}\right) + \frac{\delta y^{\,2}}{\delta x_i^{\,2} + \delta y^{\,2}}\left(f_{i,j-1} + f_{i,j+1}\right) \right] \right\}. \tag{3.3.1}$$

where s is the smoothing parameter. If we apply this smoother to a sinusoidal field

$$f = Ae^{i(2\pi x/L + 2\pi y/M)},$$

where L and M are the wavelengths in the x- and y-directions, respectively, and where we make the simplification $\delta x_i = \delta y$, we can readily derive the result

$$\tilde{f} = Bf. \qquad (3.3.2)$$

B is the response function, given by

$$B(s;L,M) = 1 - \frac{s}{1+s}\left(\sin^2\frac{\pi\delta x}{L} + \sin^2\frac{\pi\delta y}{M}\right). \qquad (3.3.3)$$

For $s = 1$, $B = 0$ when $L = M = 2\delta y$, so that wavelengths of two grid-lengths are totally removed. On our grid this corresponds to zonal wavelengths of 314 km at 45°N. After some subjective experimentation it was found that three applications of the spatial smoothing operator, using $s = 1$, on the absolute vorticity, with an additional three applications on the potential vorticity, resulted in much smoother vorticity contours.

The temporal smoothing operator is a centred, 5-day average, with equal weights, and is applied last. Application of both smoothing operators results in much smoother contours, and yields scatter plots with a significantly lower degree of scatter. Experiments have revealed that it is inadequate to apply only one or the other of the temporal or spatial smoothers. Contours of vorticity in this case are still rather rough, particularly over the northernmost latitudes, and scatter diagrams of the partially-smoothed fields have a higher degree of scatter.

Using the smoothed fields, the series of scatter plots was constructed by plotting for each day vorticity against ψ for grid points of approximately equal geographical spacing. Because a latitude-longitude grid has been used, simply using values at all points would give far too much emphasis to the northernmost latitudes, where grid-points are closer together in the zonal direction. For plotting, a simple spacing algorithm has been employed, which picked out grid points that are spaced approximately the same, along each grid row (in the zonal direction). Every point whose values are plotted represents the centre of a grid square, with a geographical area equal to approximately 49000 km^2.

For the calculation of the least-squares-fit $q(\psi)$ lines, and the area of the scatter plots, the (q,ψ) values are interpolated linearly in the zonal direction, at a constant zonal spacing of 192 km, which is the zonal grid-length at 30°N. The meridional spacing is 222.2 km, so we are using grid boxes that are nearly square.

3.4 Least-squares q(ψ) lines

Using standard formulæ (e.g. Mendenhall et al., 1981), linear least-squares coefficients are computed for values of stream-function, ψ, and potential vorticity, q, taken from the equidistant geographical points, for each day's data. The coefficients are computed using q as the independent and ψ as the dependent variable, respectively. The variables are scaled before any calculations, in order to avoid overflow and other numerical errors. Two sets of q(ψ) lines are calculated, one for data from outside the block and one for data from inside the block.

It is difficult to devise a simple yet effective algorithm to pick out precisely the data points lying within the block. Our method of using a fixed box-shape entails either excluding some interior points, or including exterior points. This inevitably affects the values of the linear least-squares coefficients. For example, suppose the block consists of a circular region of closed contours. Then the corners of a box enclosing the block would include some points from *outside* the circular region. In a modon, these exterior points would have (ψ,q) values that lie along a different line than the one defined by (ψ,q) values from within the region of closed contours. Hence a least-squares-fit line that includes these exterior points will be a poorer approximation to the interior q(ψ) line.

In our case, there are much fewer interior than exterior data points (204 versus 1655, respectively), so that the *interior* line is more easily 'contaminated' by the inclusion of (ψ,q) values that are really outside the block. Since there are so many exterior data-points, including some of the interior values in the calculation of the exterior least-squares coefficients will not have too much of an effect. Therefore the error can be reduced by defining a fairly small box, thereby ensuring that as few exterior points as possible are included in the box, at the expense of losing a few true interior points to the outside of our box.

To further ensure that we exclude as many exterior points as possible, we impose the condition, that (ψ,q) values from within the box are *not* used in the computation of the interior least-squares line, *unless* the ψ values lie within 1.8 standard deviations of the mean value of ψ within the box. The change in the least-squares slopes and intercepts for the interior region, compared to when this condition is omitted, is greatest (approximately 10%) during the first and third weeks of February, when the lines from the interior and exterior regions are most different. The rest of the time,

the change is negligible. Assuming that the values of ψ are normally distributed about their mean, this algorithm will exclude about 8% of the scatter plot points. It turns out that, on average, the percentage of points actually excluded is 8%.

3.5 Vorticity flux and the area of the q(ψ) plots

The line integral in (x,y) space of the net potential vorticity flux, in (2.5.1), has been computed along the edges of the box bounded by the latitudes 46° and 70°N, and longitudes 114° and 166°W. This box was subjectively chosen to surround, as closely as possible, only the portion of the block having closed contours, on as many days as possible.

The line integral is approximated using finite differences along the edges:

$$F_q \approx -\sum_{j=166\,^\circ W}^{114\,^\circ W} q_{i,j}\frac{\delta\psi_{i,j}}{\delta x_i}\delta x_i\Big|_{i=46\,^\circ N} - \sum_{i=46\,^\circ N}^{70\,^\circ N} q_{i,j}\frac{\delta\psi_{i,j}}{\delta y}\delta y\Big|_{j=114\,^\circ W} + \sum_{j=114\,^\circ W}^{166\,^\circ W} q_{i,j}\frac{\delta\psi_{i,j}}{\delta x_i}\delta x_i\Big|_{i=70\,^\circ N} + \sum_{i=70\,^\circ N}^{46\,^\circ N} q_{i,j}\frac{\delta\psi_{i,j}}{\delta y}\delta y\Big|_{j=166\,^\circ W}. \qquad (3.5.1)$$

Here we have used the *outward* unit normal, so *positive* F_q implies a net transfer of vorticity *out of* the box. The summations are in an anti-clockwise sense, along the southern, eastern, northern, and western edges, respectively. Clearly the terms δx_i and δy cancel, so that the approximation does not explicitly depend on the grid resolution. The sign of the contribution of each edge varies with the sign of δx_i and δy in the numerator; these are negative on the western and northern edges of the box. The remaining differences $\delta\psi_{i,j}$ are evaluated as forward, centred, or backward differences according to whether the point (i,j) lies on the end or within the line segment. For example, the first sum in (3.5.1) has the differences

Forward (initial point): $\delta F_q = \frac{1}{2}(q_{i,j} + q_{i,j+1})(\psi_{i,j+1} - \psi_{i,j})$
Centred (interior): $\delta F_q = \frac{1}{2}q_{i,j}(\psi_{i,j+1} - \psi_{i,j-1})$
Backward (end point): $\delta F_q = \frac{1}{2}(q_{i,j} + q_{i,j-1})(\psi_{i,j} - \psi_{i,j-1})$.

Referring to Figure 3.5.1, we evaluate the (ψ,q) space area integral of (2.5.3), as follows. Although we evaluate the net vorticity flux as a line integral around the boundary of our fixed region, we could obtain the same result by evaluating the net

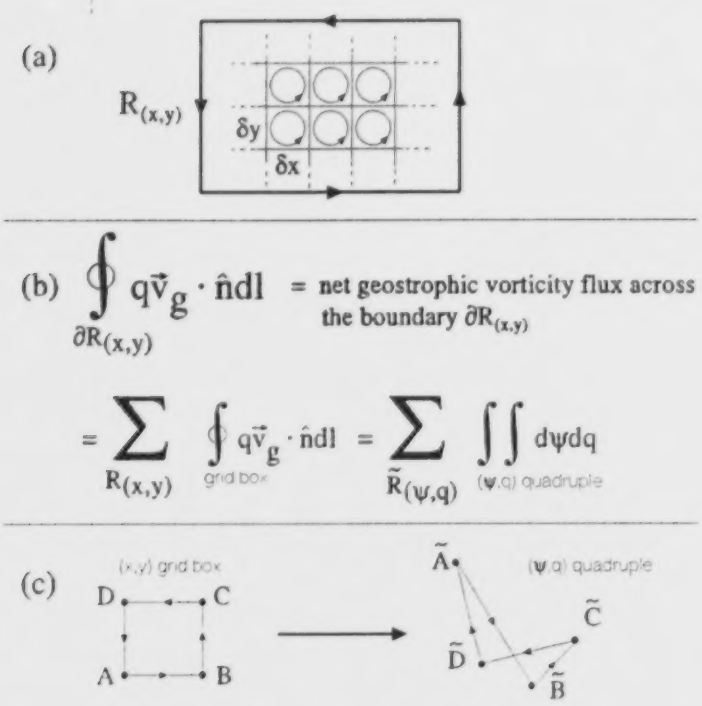

Figure 3.5.1 Evaluating the (ψ,q) area integral. (a) and (b) show the equivalence of the net flux as a line integral around the boundary, with the summing of the (ψ,q) areas associated with each interior grid box. (c) shows a typical (ψ,q) area that can be evaluated using (3.5.2).

flux across individual grid boxes, and then summing over all the grid boxes within the block region. From Figure 3.5.1(a) we see that the contribution from adjacent interior grid-box edges cancel, leaving only the contributions from the outside edges. It is then possible to express the area enclosed by the corresponding (ψ,q) curve, as the sum of the areas corresponding to all the grid boxes within the block region (see Figure 3.5.1(b)). The (ψ,q) curve corresponding to each grid box encloses an area that is easily computed using the integral

$$\text{Area} = \frac{1}{2}\oint[\psi dq - q d\psi]. \tag{3.5.2}$$

It can be readily demonstrated that this formula always gives the correct sign and

magnitude, for any (ψ,q) curve corresponding to the four corners of a grid box, one example of which is shown in Figure 3.5.1(c).

3.6 Vertical structure eigenvalues and eigenfunctions

We solve equation (2.3.10) for the first four eigenvalues k_n, where n = 0, 1, 2, 3. We use the following numerical values:

1. p_b = 850 mb (our lowest data level);
2. p_t = 250 mb (the highest level in our data set);
3. $219.5 \leq A \leq 426.1$, for the static stability power-law;
5. $\epsilon = 2/7$ exactly, in order to have Bessel functions of half-odd-integer order, which are straightforward to evaluate.

The coefficient A in the static stability power law

$$\sigma \approx A\, p^b, \tag{2.3.3}$$

was found by *assuming* a constant lapse rate, and using a mean virtual potential

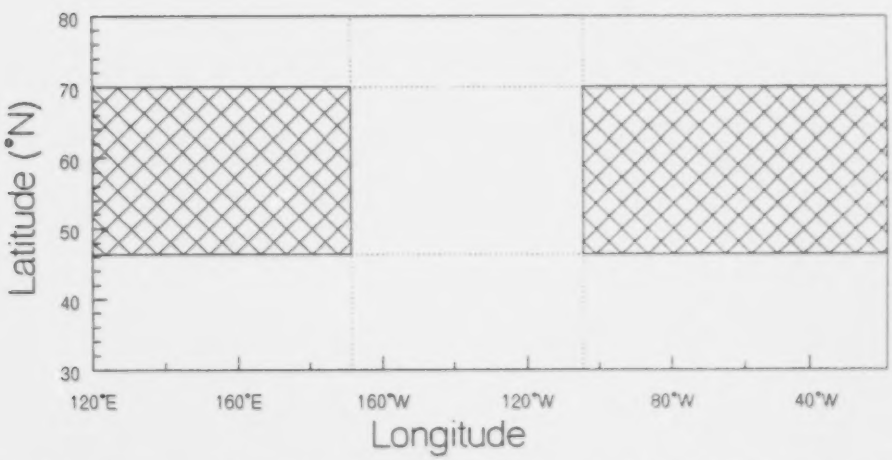

Figure 3.6.1 Evaluation of U'(p)/U(p) for $p=p_b$, and $p=p_t$. The hatched area shows the region over which the term is averaged.

temperature over the entire layer 850 to 250 mb, of 300 K. The average virtual potential temperature over all the data levels, over all days, $\bar{\theta}_r$, is 300 K.

The lapse rate, Γ, was estimated using centred differences between each data level, of the area mean (reference) virtual temperature, T_r, i.e.

$$\Gamma = -\frac{dT_r}{dz} = \frac{gp}{RT_r}\frac{dT_r}{dp},$$

in which the hydrostatic equation and the gas law have also been applied. A weighted average of Γ was then computed over the interval 850 to 250 mb, and averaged over all days; the resulting constant lapse rate was found to be

$$\Gamma = 5.23°C/km,$$

which is reasonably close to the U.S. Standard Atmosphere lapse rate of 6.5°C/km, but not as close to the dry-adiabatic lapse rate $\Gamma_d = g/c_p = 9.75°C/km$. By applying the preceding results to (2.3.4), the range of values of A corresponding to the range of

$$5.23°C/km \leq \Gamma \leq 9.75°C/km$$

is

$$426.1 \geq A > 0.$$

However we pick a lower value A = 219.5, which is equivalent to choosing a constant lapse rate of Γ = 7.42°C/km. Our range of A thus corresponds to a 1.1°C/km 'buffer' on either side of the U.S. Standard lapse rate.

The calculation of the background zonal wind term $U'(p)/U(p)$, used in (2.3.9) and (2.3.10) goes as follows. The numerator is computed using the thermal wind equation at 850 and 250 mb

$$\frac{\partial U}{\partial p} = \frac{R}{p f_0}\left(\frac{\partial T}{\partial y}\right)_p.$$

For T we use the virtual temperature, zonally averaged along latitudes 46°N and 70°N, but excluding values from inside our box, between longitudes 114°W and 166°W (refer to Figure 3.6.1). $\partial T/\partial y$ is then estimated as $(\bar{T}_{70°N} - \bar{T}_{46°N})$ / 2667 km, where

$\overline{T}$ indicates a zonal average.

The denominator U(p) is estimated by computing the average geostrophic wind at 850 and 250 mb, over the same region (hatched area in Figure 3.6.1). The average values of $U'(p)/U(p)$ over 35 days (January 23 through February 26), are found to be -3.3399×10^{-5} Pa^{-1}, at 850 mb, and -2.0898×10^{-5} Pa^{-1}, at 250 mb.

The eigenvalues k_n were first located approximately by graphing (2.3.10), after which the successive bisection method was used for increased accuracy. The first four eigenvalues thus found are listed in the following table. The two numbers given in each row of the table are the values found with A = 219.5, and A = 426.1, respectively.

n	k_n [$\times10^{-6}$ m^{-2}]
0	1.745811 / 1.253767
1	5.641016 / 4.051074
2	9.999512 / 7.179980
3	14.54419 / 10.44449

Examination of (2.3.6) and (2.3.7) shows that the magnitude of the eigenvalues is closely related to the value of A, which in turn is rather sensitive to the constant lapse rate Γ. The tabulated eigenvalues show the range of the k_n corresponding to the constant lapse rate $\Gamma = (6.5 \pm 1.1)°C/km$.

We shall use the k_n corresponding to A = 219.5, for the remainder of the computations. Experiments showed that this choice had no discernable effect on any of the results, with the exception of the modon radius calculations.

The eigenfunctions $\Psi_n(p)$, n = 0, 1, 2, 3, are computed using the solution (2.3.7), which, with $\epsilon = 2/7$, takes the form

$$\Psi_n(p) = p^{\frac{\epsilon-1}{2}}\left[c_1 J_{5/2}\left(\frac{2\sqrt{A}\,k_n}{\epsilon f_0} p^{\epsilon/2}\right) + c_2 J_{-5/2}\left(\frac{2\sqrt{A}\,k_n}{\epsilon f_0} p^{\epsilon/2}\right)\right]. \tag{3.6.1}$$

We let $c_1 = -1$, and c_2 is defined by the upper boundary condition (2.3.9).

The next step is to orthonormalize the four eigenfunctions over the interval $[p_b, p_t]$. The eigenfunctions are already orthogonal, since they are linearly independent solutions of a Sturm-Liouville boundary value problem (2.3.1), (2.3.2) in this interval. However, to ensure the accuracy of our discretization of the Ψ_n, we go through the complete Gram-Schmidt orthonormalization procedure. This we carry out as described in Arfken (1985). The resulting modes are normalized by dividing each one by the integral of its square over the vertical domain, thus

$$\Psi_m(p) \leftarrow \Psi_m(p) \div \left[\frac{1}{(p_b - p_t)} \int_{p_t}^{p_b} [\Psi_m(p)]^2 dp\right], \tag{3.6.2}$$

so that they satisfy the relation

$$\frac{1}{(p_b - p_t)} \int_{p_t}^{p_b} \Psi_m(p)\,\Psi_n(p) dp = \delta_{mn}, \tag{3.6.3}$$

where the Kronecker delta is defined as

$$\delta_{mn} = \begin{cases} 0, & m \neq n \\ 1, & m = n \end{cases}$$

We have employed Simpson's 1/3 rule for the evaluation of the integrals in (3.6.2) and (3.6.3), at 60 equidistant pressure levels from 850 to 250 mb.

We use the orthonormalized eigenfunctions as the basis functions in a generalized Fourier series for the vertical structure of the *eddy* stream-function, within the fixed box that approximates the region occupied by the block (bounded by latitudes 46°N

and 70°N, and longitudes 114°W and 166°W). The eddy stream-function is defined from (2.2.16) and (2.2.42) as

$$\psi_1(x,y,p) = \psi(x,y,p) - \psi_r(p) - \psi_0(x,y,p),$$

so that, to estimate it, we must subtract from the data, first, a hydrostatic reference stream-function, followed by a background zonal flow stream-function. We have used the constant lapse rate 5.23 °C/km to calculate a reference thermal profile, which is then used with the gas law and the hydrostatic equation to compute values of ψ_r at each data level (850, 700, 500, 400, and 250 mb). We estimate the zonal flow

$$\psi_0 = -U(p)\,y$$

by noting that this may be written as

$$U(p)\cdot y = \int^{y} U(p)dy = \int^{y} \frac{d}{dy}\langle\psi\rangle_x dy = \langle\psi\rangle_x,$$

where $\langle\psi\rangle_x$ is the average along a latitude line, of the dynamic anomaly stream-function. In computing the zonal average, the values within the block region have been omitted (refer to Figure 3.6.1).

After subtracting out the reference and zonal flow components, we are left with estimates of the eddy stream-function at each grid point within the block region. Because the zonal separation of grid points decreases as we go northward, we interpolate (linearly) values of the eddy stream-function at a constant zonal interval of 192 km. This leaves us with a set of eddy stream-function values at points that are evenly spaced horizontally, at five data levels. At each of the evenly-spaced points, we then interpolate linearly in the vertical, at 60 equidistant levels between 850 and 250 mb. This enables the calculation of the generalized Fourier coefficients using Simpson's 1/3 rule for the integrals, at each point within the block region.

The Fourier series is

$$\psi_1(x,y,p) = \sum_{n=0}^{\infty} a_n(x,y)\,\Phi_n(p). \tag{3.6.4}$$

We calculate the four lowest terms in the series, at each point (x,y). The Fourier coefficients, a_0, a_1, a_2, a_3, are computed using the usual Fourier formula

$$a_n(x,y) = \frac{1}{(p_b - p_t)} \int_{p_t}^{p_b} \psi_1(x,y,p)\,\Phi_n(p)\,dp. \tag{3.6.5}$$

The integral in (3.6.5) is evaluated by Simpson's method, using the interpolated values of $\psi_1(x,y,p)$ at the 60 equidistant pressure levels between 850 and 250 mb.

One set of four coefficients is thus calculated for each evenly-spaced grid point within the block region. In order to be able to compare the average contribution of each mode to the vertical structure of the eddy, we compute the root-mean-square (RMS) value of each coefficient, defined as

$$\langle a_n \rangle_{RMS} = \left[\frac{\sum_{x,y}^{(Npoints)} [a_n(x,y)]^2}{N} \right]^{1/2}.$$

The RMS values are then scaled so that the sum of their squares is unity, i.e.

$$\langle a_n \rangle_{RMS} \leftarrow \langle a_n \rangle_{RMS} \div \sqrt{\langle a_0 \rangle^2_{RMS} + \langle a_1 \rangle^2_{RMS} + \langle a_2 \rangle^2_{RMS} + \langle a_3 \rangle^2_{RMS}}. \tag{3.6.6}$$

The foregoing computations are repeated for each day from January 23 through February 26. The results portray the evolution of the relative contributions of the different modes to the vertical structure.of the blocking eddy.

Chapter 4

Results and Discussion

The discussion and evaluation of the results of our computations will proceed as follows. First, a description of the 500 mb flow pattern evolution will be presented. Next will follow a discussion of the scatter diagrams, in which their resemblance to a free mode form is subjectively analyzed. The slopes of the least-squares lines, $dq/d\psi$, are used to examine the hydrodynamic stability of the block. We present the results of using $dq/d\psi$ for testing the modon existence condition, and for calculating a modon radius. We then discuss the vorticity flux and (q,ψ) space area integrals, and their utility as measures of the block's free mode behaviour. In the final section we present the results of the vertical normal mode analysis. Throughout this chapter our discussion is based upon the 5-day mean values of stream-function and vorticity, charts of which are given in Appendix A2.

4.1 Synopsis

During the latter half of January, a strongly baroclinic situation was in place over North America. A zonal flow of quite mild Pacific air persisted over central Canada, while a very cold air mass lay over the Arctic, where record-setting minimum temperatures and maximum barometric pressures were recorded, notably the highest ever North American surface pressure reading of 1074.8 mb, at Northway, Alaska, on January 31. In the first few days of February, a blocking ridge formed quickly over the North-east Pacific after an intense cyclonic system left the Gulf of Alaska and tracked across western Canada and the United States. This resulted in a surge of Arctic air that reached the west coast and covered all but the southernmost states. The block was characterized, in the lower troposphere, by a very strong horizontal thermal contrast between its mild Pacific flank and the cold northwesterly stream further east over central North America. For example, during the second week in February, record mild temperatures were observed over Yukon, while near-record low temperatures were experienced over southern Canada (Canadian Climate Centre 1989).

Initially, on January 23, there are four features of interest (refer to Appendix A2):

i) the arctic vortex, centred in the Arctic Ocean north of Alaska (78°N 160°W);

ii) a dipole structure, in Northeast Asia (centre: 68°N 140°E);
iii) a cyclonic vortex over the western shore of Baffin Island (70°N 80°W).
iv) a weak ridge oriented northeast-southwest about 1800 km west of California.

Over most of North America, on January 23, the flow is predominantly westerly, with a weak trough over Nevada and California. Extending from the Northwest Pacific, across the Bering Sea, and linking with the Arctic vortex, is an elongated trough. Beginning January 24, this trough merges into a strong cyclonic vorticity centre, that moves rapidly southeastward, away from the arctic vortex. By January 28, this disturbance has moved into the Gulf of Alaska, and has developed a number of closed contours. A ridge emerging out of the quasi-stationary Asian dipole amplifies steadily. The Asian dipole evolves into a multipole, with several vorticity maxima and minima rotating about a centre at 60°N 155°E (Kamchatka Peninsula). The initially weak eastern Pacific ridge also builds until it reaches the Queen Charlotte Islands by January 28.

The arctic disturbance and the eastern Pacific ridge together produce an intense southwesterly flow over the Gulf of Alaska. The arctic disturbance continues to advance southeastward, so that by January 31, the flow over the Gulf is northwesterly. At this time, west of the arctic disturbance, warm, low-vorticity air is advected into the northern ridge. By February 1 the two ridges are in phase, forming a single, large-amplitude blocking ridge: the Omega-block. This feature is flanked by two large vortices (over Northern Asia and Baffin Island), with the smaller, more intense arctic disturbance still moving southeastward down its side. After February 8, the arctic disturbance becomes indistinct as it merges with the strong westerly flow over the eastern United States.

Between February 9 and 15 the ridge over the Gulf of Alaska is traversed by a series of cyclonic and anti-cyclonic short-wave disturbances. By February 16, cyclonic systems to the east and west pinch off the ridge, resulting in closed contours. From February 17 through 20, the block consists of a cut-off anti-cyclone to the north, with two smaller cut-off cyclonic vortices to the south. It is during this period that the block is most reminiscent of a dipolar modon. After February 20, the anti-cyclonic component weakens rapidly, while the cyclonic part remains intense, and drifts southeastward. The ridge lying along 170°W on February 22 builds into the region formerly occupied by the block, before it, too, weakens after February 26 (not shown

in Appendix A2).

Based on the 500 mb flow pattern, we may subjectively consider the block to have evolved between two states. From about February 1 to 15, the flow pattern had the familiar 'Omega' (Ω) shape. During the second, shorter period, February 18 to 22, immediately before it broke down, the block developed a discernible dipole-like form. The question of whether either of these states represents a free mode is central to the discussion in this chapter.

4.2 Scatter diagrams and the evolving block

We concentrate in this discussion on diagrams from the 500 mb surface, the full series of which is presented in Appendix A2. We present two sets of scatter plots: stream-function versus (the vertical component of) absolute vorticity, and stream-function versus quasi-geostrophic potential vorticity. We recall that our potential vorticity is simply the absolute vorticity plus a baroclinic stretching term. For barotropic dynamics, we would expect no difference between the two types. Hence, by comparing the two series of scatter plots, we can observe, at least qualitatively, the degree of baroclinicity in the block.

In general there were few differences between the 500 mb diagrams and those of the other pressure levels. This weak vertical variation is confirmed by our analysis of the vertical normal modes in section 4.5. One interesting observation is that our 500 mb level scatter charts show the sharpest definition, and the linear, multi-valued vorticity-stream-function relationship is visually most evident at this level. This contrasts somewhat with the results of Butchart et al. (1989), who derived most of their conclusions from charts at the 300 mb level. In general, the non-linear dynamics, characteristic of modon-like structures, could be expected to be more dominant at higher levels in the troposphere, where non-linear advective effects are more significant due to the increased average wind speeds. Our 400 mb $q(\psi)$ scatter diagrams (not shown) were not nearly as well-defined as those at 500 mb. The reason is that the 250 mb surface intersects the tropopause. With our coarse vertical resolution, this leads to errors when computing the baroclinic term for q at 400 mb, due to the sharp increase in the vertical static stability at the tropopause. A display of our charts at levels other than 500 mb has been considered unnecessary.

The first two days' scatter charts indicate a single, roughly linear vorticity-stream-

function relationship. There appears to be no significant difference between values from within the box (46 to 70°N, 114 to 166°W) and the exterior regions.

As the arctic disturbance intensifies and moves southeastward, the plot steepens slightly, and there emerges a distinct 'lobe' of interior points on the scatter diagram, easily discernible by January 28. This cluster of points is clearly due to the disturbance, since it is composed of relatively high vorticity, low stream-function values. With time, the lobe moves toward higher stream-function and lower vorticity, consistent with the translation of the vortex southeastward. Although we see a non-analytic vorticity-stream-function relation during this time (January 28 to February 6), it is clear that the stream-function and vorticity fields are not those of a dipole. This indicates that a non-analytic, linear $q(\psi)$ relation is not sufficient for the flow to have the modon free mode form. The disturbance clearly does not have zero net angular momentum, which we recall is a requirement for a persistent (quasi-stationary) isolated eddy (Stern 1975; Flierl et al. 1983), and thus it must translate.

We could at this point guess that the travelling vortex is some kind of free mode; we see clearly on the scatter diagrams a fairly strong indication that $q = q(\psi)$, which is our definition of a free mode. However, as we will point out in section 4.4, the (ψ,q) plot area indicates that the system is far away from a free mode configuration during the days in which the vortex predominates, compared to when the Omega- and dipole-form blocks are in place.

The initial steepening due to the arctic disturbance is consistent with the observations of Malanotte-Rizzoli and Hancock (1987). For their composite of 12 Atlantic blocking ridges, they describe, in their terminology, a northern barrier of the trapping potential, which emerges and intensifies during the first week. This is equivalent to a steepening of the $q(\psi)$ scatter plot. It is interesting that in both cases, the initial steepening is out of the north. If we consider the disturbance as a vorticity source, S, the steepening is also in agreement with equation (2.5.6):

$$\frac{dq}{d\psi} = - \frac{\iint_{\mathcal{R}_\psi} S\,dx\,dy}{K \oint_{\psi} \vec{v} \cdot d\vec{l}}$$

Hansen and Chen (1982) observed that blocking was preceded by intense synoptic-

scale development, *upstream* of the block. In our case, there is some activity upstream of the block, prior to its formation. The elongated trough over the Northwest Pacific (January 23-25) appears to merge into the arctic vorticity centre before the latter intensifies over the eventual location of the block.

The travelling vortex may also be explained by referring to the rotating-tank modons found by Flierl et al. (1983). In their experiments, the shear from a narrow barotropic jet gave rise to an asymmetric dipole, which translated in a curved path. We may speculate that the anticyclonic shear at the southwest edge of the travelling arctic vortex accomplishes what the jet did in the tank experiments; that is, the shear acts to spin up the anticyclonic vorticity in the block.

From February 8 through February 12, the scatter-plots again show a roughly linear, analytic relationship. During this time, there appear to be no closed streamlines or vorticity contours, suggesting that the dynamics are nearly linear. The $q(\psi)$ scatter plots for the interior region, over the same time, show a rather distinctly linear $q(\psi)$ relationship, suggesting the Omega-block is also a free mode. We observe, subjectively, a poorer correlation between *absolute* vorticity, ζ_a, and ψ, which indicates that this free mode is better represented by our baroclinic model. From February 13 onwards, closed contours become visible, and a distinct low-vorticity lobe emerges on the scatter plot for the interior region. This we associate with the cut-off anti-cyclone building over Alaska.

The scatter plots exhibit a fairly distinct non-analytic, linear form between February 15 and 21. The $q(\psi)$ plots for the interior block region have a more symmetric form, i.e. the cyclonic and anti-cyclonic lobes balance one another. The plots of absolute vorticity versus stream-function lack a distinct anti-cyclonic lobe, although they exhibit a more distinct cyclonic component. The 500 mb flow pattern and the $q(\psi)$ scatter plots on February 19 through 21 bear a reasonable resemblance to those of the equivalent barotropic modon (see Figure 1.2). After February 22, as the

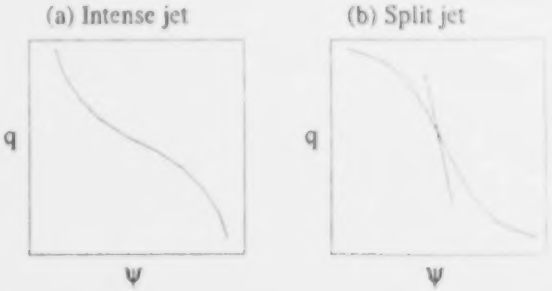

Figure 4.2.1 Idealized $q(\psi)$ plots showing the difference in curvature between (a) intense-jet anomaly, and (b) split-jet anomaly. See text for discussion.

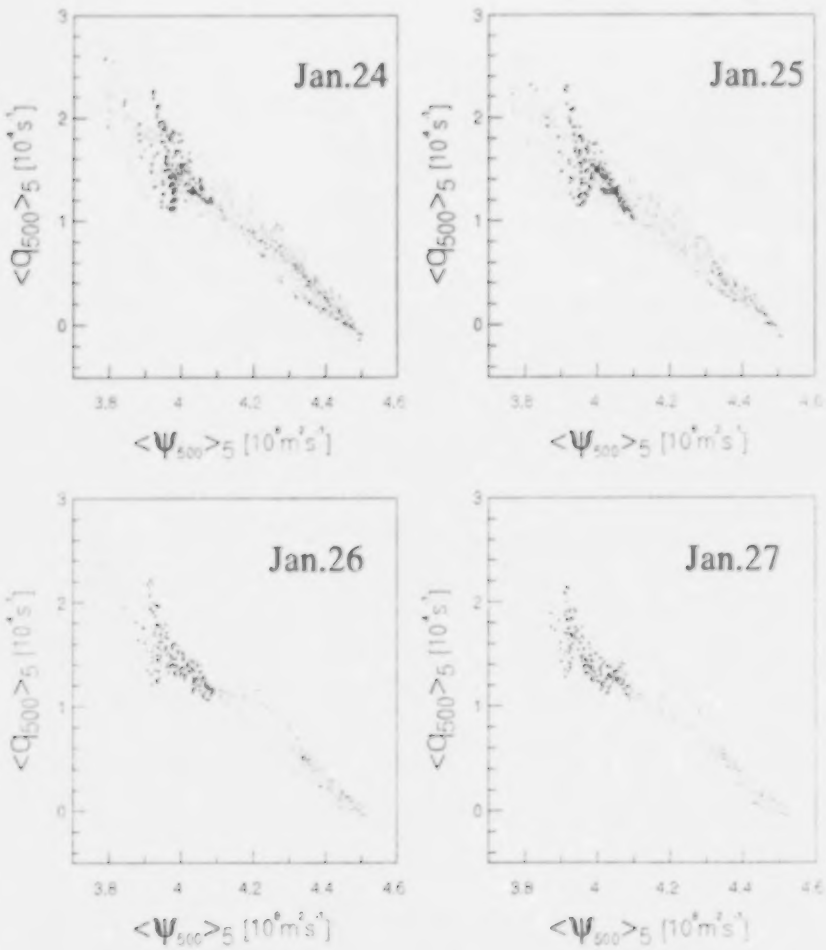

Figure 4.2.2 Scatter diagrams of 500 mb geostrophic stream-function versus potential vorticity. Crosses indicate values from within the area between 46-74°N, and 128-176°E.

dipole block breaks down, the scatter plots continue to have a multi-valued linear form, with a distinct cyclonic lobe persisting until February 25. This lobe is clearly associated with the intense vortex that slowly moves out of the rectangular block region. A matching anti-cyclonic component is difficult to perceive on the scatter plots, which is also the case during the last week in January when the intense arctic disturbance is dominant. Thus the demise of the block is similar to its birth, both events being accompanied by transient, strongly cyclonic synoptic-scale vortices. However, as shall be seen in section 4.4, there are significant differences between the two vortices, with respect to the net vorticity flux over the fixed block region.

It is not clear whether the curvature of our scatter plots for the exterior region is consistent with that found in numerical experiments by Haines and Mallanote-Rizzoli (1991). They discovered that the slope $dq/d\psi$ is more negative to the north and south of the block in the case of an intense-jet anomaly (Fig. 4.2.1(a)), in contrast with the split-jet anomaly, or block, where $dq/d\psi$ is less negative to the north and south (Fig. 4.2.1(b)). The lack of definition to the exterior region component of our diagrams is probably because the flow in this region does not consist of a simple zonal flow, but rather contains other vortices that cause significant spread about the idealized vorticity-stream-function lines.

One such feature is the multipole over Northeast Asia, which is interesting since it appears to emit blobs of high and low vorticity air. Of particular interest is the anticyclonic blob that emerges over the Kamchatka Peninsula (62°N 164°E) on January 27; it is this feature that appears to evolve into the blocking ridge over the Gulf of Alaska from February 4 to 8. To further examine the multipole, a series of scatter diagrams were produced that distinguish vorticity-stream-function values from the box-shaped region between latitudes 46-74°N, and longitudes 128-176°E. For the days January 24-26, plots from this region resemble miniature modon diagrams (Figure 4.2.2). On other days (not shown), the plots are less well defined, probably due to our choice of a large box that encompasses many points exterior to the multipole. We may speculate that the Asian system acts as a source of synoptic-scale eddies, which are entrained into the block downstream by means of the straining mechanism described by Shutts (1986). Assuming that the form of $q(\psi)$ in the eddies survives this process, it could explain the distinctive $q(\psi)$ relation which develops within the block at its dipole stage.

4.3 The slope $dq/d\psi$: hydrodynamic stability, modon existence condition, and the modon radius

The values of slopes and q-intercepts, for each day's least-squares $q(\psi)$ lines, are tabulated in Appendix A1. The least squares lines are also drawn on the scatter diagram for each day.

Stability

Throughout our time series, $dq/d\psi$ and $d\zeta_a/d\psi$ are seen to be negative. This is true for the least-squares $q(\psi)$ lines, and is subjectively obvious when viewing the

scatter plots. To examine how this relates to the hydrodynamic stability, we utilize Arnol'd's second linear Liapunov-stability theorem for non-parallel flows (Arnol'd 1966, McIntyre and Shepherd 1987). A system is said to be stable, if it is configured such that the energy, constrained by a suitable Casimir functional, is near a minimum. This quantity is analogous to the energy of a classical Hamiltonian system. The theorem states that a sufficient condition for Liapunov stability, in a domain $\mathbb{C}$, is that

$$0 > \frac{dq}{d\psi} > -\nu_{min}, \tag{4.3.1}$$

everywhere in $\mathbb{C}$ (Figure 4.3.1). Here $\nu_{min} > 0$ is the minimum eigenvalue of the problem

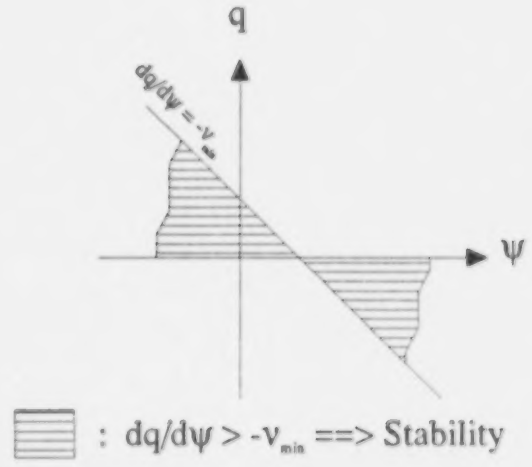

Figure 4.3.1 Illustration of Arnol'd's second stability theorem. Scatter plot curves with slopes no steeper than that of any line within the hatched area are stable.

$$\begin{aligned} \nabla^2\varphi + \nu\varphi &= 0, \quad \text{in } \mathbb{C}, \\ \varphi &= 0, \quad \text{on } \partial\mathbb{C}. \end{aligned} \tag{4.3.2}$$

We can estimate ν_{min} by considering the boundary-value problem (4.3.2) for an infinite zonal channel of width M. The solution will consist of products of sines and cosines with a zonal wave component, which, when we apply the boundary condition, leaves

$$\varphi = e^{\pm ikx} \sin\left(\frac{n\pi}{M}y\right), \quad n = 1,2,3,\ldots,$$

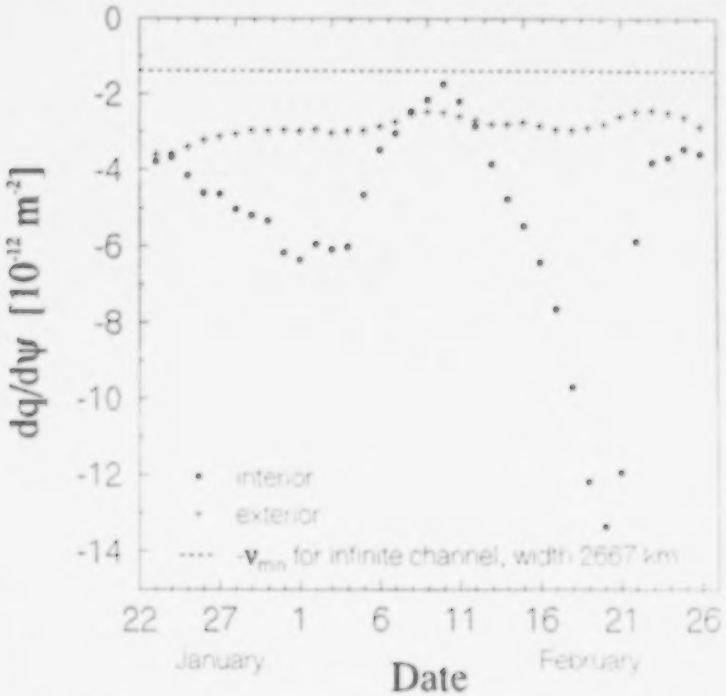

Figure 4.3.2 The slopes of the least-squares 500 mb $q(\psi)$ lines. The estimated minimum slope for stability is given as a horizontal dashed line.

where k is a zonal wavenumber. The smallest ν_{min} satisfying (4.3.2) is given by k = 0 and n = 1, that is

$$\nu_{min} = \left(\frac{\pi}{M}\right)^2.$$

If we set M = 2667 km (the north-south dimension of our usual box-shaped block region), we obtain the value

$$\nu_{min} = 1.4 \times 10^{-12}\ m^{-1}.$$

This value of ν_{min} is shown on Figure 4.3.2, together with the interior and exterior slopes of the least-squares $q(\psi)$ lines. It is evident that the stability condition, as we have estimated it, is never satisfied. Indeed, it is farthest from being met during the time when the block is strengthening, and when it most resembles a dipole. From

February 8 to February 11 the condition is closest to being satisfied. This corresponds to the time in which the Omega-block shows few closed contours, and the interior scatter plot shows a highly correlated $q(\psi)$ relation. This suggests that the Omega-block during this time is a stable free mode, and the lack of closed contours indicates it is governed by dynamics which are only weakly non-linear. Between February 12 and 23, our results indicate that the block is less stable. We would also expect the dipole form of the block to be less stable, since its duration is rather brief when compared to the lifetime of the block.

Modon existence condition and the modon radius

If we examine the computed least-squares $q(\psi)$ slopes (Appendix A1), it is apparent that the existence condition (2.2.26) is nearly always satisfied by the gravest eigenvalue $k_0^2 \approx 3.05 \times 10^{-12}\ m^{-2}$. This condition is sufficient to ensure the modon is spatially localized. We have used the stronger requirement (2.2.30), testing the slopes of our least-squares $q(\psi)$ lines, for both the interior and exterior regions, against the square of the gravest eigenvalue, i.e.

$$-\left(\frac{dq}{d\psi}\right)_{interior} > k_0^2 > -\left(\frac{dq}{d\psi}\right)_{exterior} . \qquad (4.3.3)$$

This relation is tested using each day's slopes. If it is satisfied, the modon dispersion relation (2.2.33)

$$-\frac{K_2(\gamma a)}{\gamma K_1(\gamma a)} = \frac{J_2(\lambda a)}{\lambda J_1(\lambda a)} \qquad (2.2.33)$$

is then solved for the radius a. The constants γ and λ are defined to be

$$\gamma^2 = k_0^2 + (dq/d\psi)_{exterior},$$

and

$$\lambda^2 = -(dq/d\psi)_{interior} - k_0^2.$$

We use Newton's method to solve (2.2.33) for a. The physical separation of the modon vorticity extrema can be readily found by setting $\partial/\partial r$ of (2.2.61b) equal to zero and solving for r. The separation is found to be approximately 0.95 a. The results are displayed in the following table, together with the measured separation of the potential vorticity extrema, abstracted from the charts in Appendix A2 onto

a polar stereographic projection. The separation is not straightforward to measure, since on most of the days in question we observe two or more (cyclonic) q-maxima near the southern boundary of the rectangular block region. Three measurements are given for the separation of extrema that are inside, or very close to, the rectangular block region:

1. distance between the northern q-minimum and the western q-maximum;
2. distance between the northern q-minimum and the eastern q-maximum;
3. distance between midpoints of q-mimima and midpoints of q-maxima.

Date	Modon Radius [km]	Modon q-extrema separation [km]	Observed q-extrema separation [km]
February 15	2561	2418	1333/2700/1133
February 16	2135	2033	1389/2000/889
February 17	1804	1725	1478/1889/1500
February 18	1495	1432	1778/2144/1611
February 19	1277	1223	1833/2111/1789
February 20	1205	1152	1822/1922/1789
February 21	1309	1246	1500/1444/1644
February 22	2410	2251	1833/1833/1556

It turns out that the existence condition (4.3.3) is satisfied for some days on which the block does not have a dipolar form at all, in particular during the period between January 31 and February 4, when the intense arctic disturbance is dominant. Although it is possible to formally compute a modon radius value on these days, it has little if any physical meaning. Therefore we have shown only those results from the period in which a dipolar structure is evident. The radii from February 18 through 21 appear to be in good agreement with the actual size of the block.

The sensitivity of the computed radius to the least-squares slope was examined by subjectively choosing a slightly steeper line to fit the February 19 interior region plot, with a slope of -2×10^{-11} m^{-2}, which we argue makes a 'better' fit to the scatter plot for the interior region. The corresponding modon radius is 934 km, which is still reasonably close to the actual dimension of the dipole block. It can be seen that several of the least-squares lines do not appear to be steep enough, so that our tabulated estimates of the modon radius may be slightly high. We note that these results are quite sensitive to our choice of $k_0 = 1.7458\times10^{-6}m^{-2}$. The value $k_0 = 1.2538\times10^{-6}m^{-2}$, which corresponds to the constant lapse rate $\Gamma = 5.23°C/km$, does not even satisfy (4.3.3).

The separation of modon q-extrema and the observed separation show little agreement, no matter what measuring scheme is used. This is not surprising, however, since the separation measurement is highly affected by the asymmetry of the vorticity field. This asymmetry is not optimally represented by the map projection used for Appendix A2. It could be influenced by the choice of temporal smoother. We must stress that these results are quite sensitive to the choice of k_0, and so we do not put too much emphasis on them.

4.4 Vorticity flux and the area of the $q(\psi)$ plots

The computed $q(\psi)$ plot area (for the interior of our box), along with that of the net geostrophic vorticity flux, F_q, are depicted in Figure 4.4.1. The two quantities are in quite good agreement, from which we conclude that it is possible to calculate the result (2.5.3) of Read et al. (1986), and that our data are reasonably consistent.

The time series of the net flux and $q(\psi)$ area clearly show that they remain near zero values for the lifetime of the block. This strongly suggests that the block is an inertial free mode of the quasi-geostrophic equations. The two quantities evolve in a manner which we can relate to the development of the block. Between January 23 and 28, they become more negative, which is consistent with the flux of cyclonic vorticity into the block region with the intense arctic disturbance. As that system moves through and exits the rectangular region, the net flux and scatter-plot area increase strongly, up to February 3. This is interpreted as a loss of cyclonic vorticity from the region, which is consistent with the amplification of the (anti-cyclonic) blocking ridge during the first week in February. Between February 3 and 8, the net

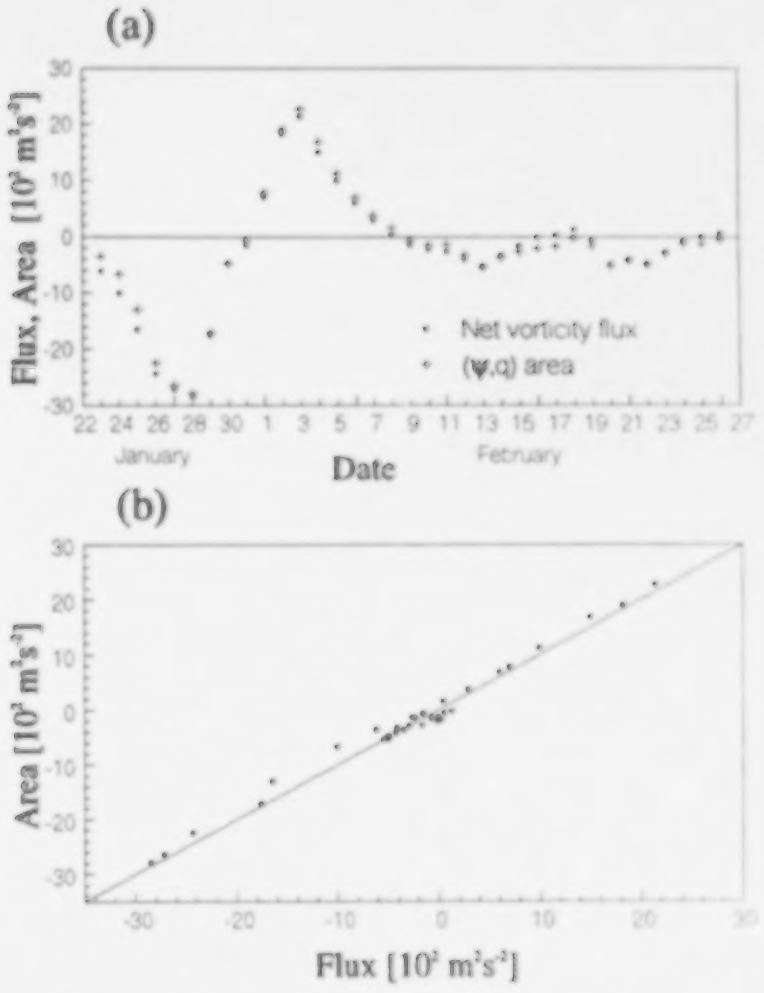

Figure 4.4.1 a) Time series of the area of the 500 mb q(ψ) scatter plots, and the net vorticity flux across the box bounded by latitudes 46°-70°N and longitudes 114°-166°W. The area values are computed using (ψ,q) values from inside the box, as well as along the edges.
(b) The same variables as (a): net vorticity flux plotted against the (ψ,q) space scatter-plot area.

flux and area decrease, and after February 8, they remain near zero; during this time the Omega-block persists over the Northeast Pacific, until the emergence of the dipole configuration between February 16 and 21. The flux and area are slightly negative during the dipole period, indicating the influx of cyclonic vorticity into the block region. This helps to explain the breakdown of the anti-cyclonic component of the dipole after February 21. The cyclonic vortex that drifts southeastward out of the block region is not associated with any significant change in the net flux. Therefore, even though this vortex may play a key role in the breakdown of the block, the physical mechanism at work could be different from that of the initial

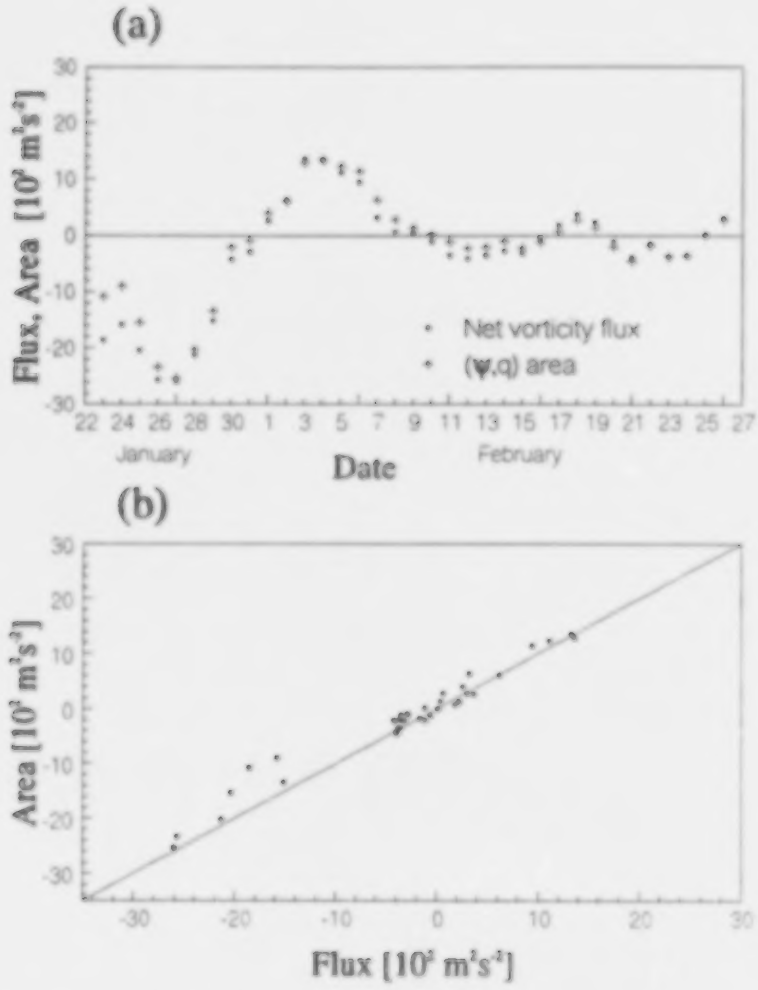

Figure 4.4.2 a) Time series of the area of the 500 mb q(ψ) scatter plots, and the net vorticity flux across the box bounded by latitudes 40°-74°N and longitudes 114°-174°W. The area values are computed using (ψ,q) values from inside the box, as well as along the edges.
(b) The same variables as (a): net vorticity flux plotted against the (ψ,q) space scatter-plot area.

arctic disturbance.

In order to see the effect of choosing a different region, we have repeated the calculations for a larger rectangular region, from 40° to 74°N and 114° to 174° W. The results, shown in Figure 4.4.2, are very similar, which indicates that the net flux and q(ψ) plot area are not too dependent on the dimensions of the block region. If we regard the scatter-plot area and net flux both as measures of departure from a free mode form (as in section 2.5), we may conclude that after February 8, the 500 mb flow is configured as a quasi-geostrophic free mode. It is interesting to

observe that the two quantities remain near zero through to the end of our data set, suggesting that, although the Omega block and dipole block have dissipated, a free mode is still dominant. Apparently, the scatter-plot area does not distinguish between the different flow configurations. It is certainly possible that the initial, zonal flow, or the flow at the end of our data set, could also be quasi-geostrophic free modes.

That the strong increase in the net vorticity flux *precedes* the amplification of the Omega-block can be related to the earlier discussion, in section 4.2, of the very intense arctic vortex. The initial increase in the net vorticity flux, and the steepening of the scatter plot, both coincide with the entry of the vortex into the blocking region, on January 29, and continue for as long as the vortex lies within the region. The net positive vorticity flux that persists from February 1 through 7 serves to extract cyclonic vorticity from the block region, which naturally leads to the amplification of the block ridge. The arctic disturbance is a good candidate for the role of synoptic-scale block-initiator, observed by Hansen and Chen (1982). It may be that the capability of this vortex to generate the block can be identified by the steepening of the scatter plot and the sustained increase in net vorticity flux. This leads to the fascinating possibility that the trend of these quantities could be used to forecast the potential for block development.

Although the distinct $q(\psi)$ scatter plots associated with the intense arctic vortex suggested that it, too, could be a free mode, the trend of the $q(\psi)$ area clearly discounts this possibility. This demonstrates the risk of simply visually interpreting the scatter plots without other information.

4.5 The baroclinicity of the block

In general the vorticity-stream-function scatter diagrams from other pressure-levels were similar to those at 500 mb. However, as discussed at the beginning of section 4.2, the 500 mb level scatter diagrams showed more clearly the linear $q(\psi)$ relation. We conclude, from the similarity of the 500 mb absolute and potential vorticity scatter diagrams, that the block is not too far from being equivalent barotropic, for the space and time scales with which we are concerned. We examine this question in more detail using the quasi-geostrophic vertical structure eigenfunctions, or normal modes, which are derived in section 2.3. The lowest four modes are shown in Figure 4.5.1.

The eigenfunctions have been orthonormalized so that for each mode Ψ_n, we have

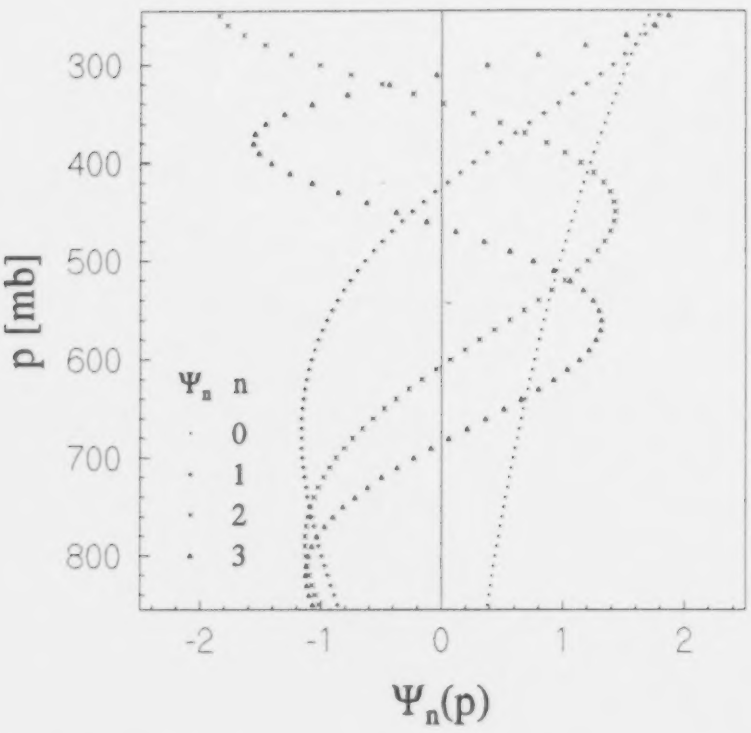

Figure 4.5.1 Vertical normal modes. These are our solutions to the boundary-value problem (2.3.1), (2.3.2), (2.3.3).

$$\frac{1}{(p_b - p_t)} \int_{p_t}^{p_b} \Psi_n(p)\, \Psi_n(p) dp = \delta_{mn},$$

in which p_b = 850 mb and p_t = 250 mb, and δ_{mn} is the Kronecker delta. We recall that these vertical normal modes do not explicitly appear in the modon solution. They originate in the definition of the inverse deformation radius k, in (2.2.48). Because of their properties as solutions of a Sturm-Liouville problem, we can use them in a generalized Fourier series for any physically-realistic function of pressure. In our case we are interested in studying the vertical structure of the eddy stream-function ψ_1 introduced in the baroclinic modon solution (section 2.2.2). As described in section 3.6, we have estimated the eddy stream-function, and computed the Root-Mean-Square values of the Fourier coefficients for the four lowest normal modes.

The time series of the Root-Mean-Square (RMS) Fourier coefficients are shown in Figure 4.5.2. They have been normalized so that the sum of squares of the

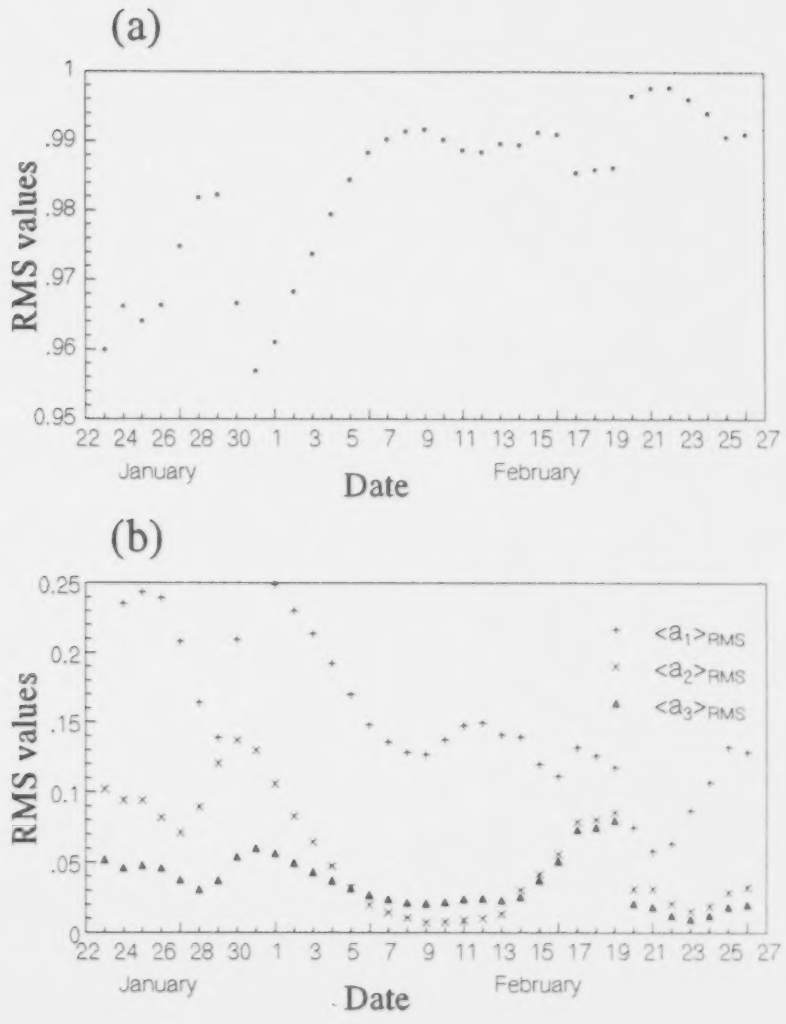

Figure 4.5.2 Time series of normalized Root-Mean-Square (RMS) Fourier coefficients of the four gravest vertical normal modes. The region over which the mean is taken is the box shape bounded by latitudes 46°-70°N and longitudes 114°-166°W. (a) Gravest mode. (b) First, second, and third modes. Normalization is such that the sum of the squares of each day's four RMS values is unity.

coefficients for each day is unity. The magnitude of each normalized coefficient shows the relative contribution of its mode to the total vertical structure of the eddy component of the stream-function.

The contribution of the gravest, "quasi-barotropic" mode (figure 4.5.2a) appears to dominate the other modes during the entire series. This confirms our initial suspicion that the block is nearly equivalent barotropic. During the first week in February, when the block first forms, there is a small but definite increase in the

contribution of the gravest mode, matched by a decrease in the contributions of the higher baroclinic modes. For the duration of the block, the contribution of the gravest mode is practically constant, with one notable exception.

Between February 17 and 19 there is a small but abrupt decrease in the contribution of the gravest mode, which then returns abruptly to its earlier level on February 20. The sudden decrease in the gravest mode's contribution is matched by a more gradual increase in those of the baroclinic modes. Between February 19 and 20, modes 0, 2, and 3 return abruptly to their levels prior to the 17th. Examining the contoured stream-function and potential vorticity charts for February 16, 17, 18, and 19 reveals a fairly intense cyclonic vortex that has developed within the block region, southeast of the cut-off anticyclone. A second, weaker vortex lies southwest of the anti-cyclone. The merging of the two vortices, south of the anti-cyclone, results in the dipole on February 20. It is clear from the contour charts that the potential vorticity of the vortex (both in term of gradient and value) is most intense on the same 3 or 4 days that have the increased RMS baroclinicity.

We suggest that the vortices which are entrained into the block, thereby forming the dipole, may play a role similar to the synoptic-scale eddies observed by Illari (1984) and Shutts (1986). That is, these vortices *force* the dipole to form. In the eddy-straining process, however, the eddies are baroclinically inactive (Haines and Marshall 1987), while our vertical normal mode analysis seems to indicate that, immediately preceding the formation of the dipole, there is a brief period of intense baroclinic activity. This does not appear to be of the same magnitude as the earlier arctic cyclonic disturbance, and it does not seem to be associated with any significant change in the net vorticity flux. The fact that it is a *brief* episode of synotic-scale activity suggests that the same non-linear, upscale energy transfer observed by Hansen and Chen (1982) may be acting in this instance.

Chapter 5

Conclusions

We have discussed a series of scatter diagrams of geostrophic stream-function versus vorticity at 500 mb, for a Northeast Pacific blocking episode. We discover that the block can be naturally divided into two stages, an Omega-block stage (February 1-15), and a dipole stage (February 18-22). During both periods the diagrams display a linear relation between potential vorticity, q, and stream-function, ψ. Calculated areas of the scatter plots, in (ψ,q) space, decrease during the same time. From Read et al. (1986) we know that the scatter plot area is a measure of the departure from a free mode. From computations of this plot area, using our data, we conclude that this block may be well-modelled by free-mode solutions of the governing (quasi-geostrophic) equations, such solutions being characterized by the relation $q = q(\psi)$. In applying Arno'ld's second stability theorem, it appears that the Omega-block is more stable than the dipole. The dynamics for this period appear to be linear or weakly non-linear, based upon the lack of closed vorticity contours. The dipole form of the block appears to be unstable, which is consistent with its relatively brief duration.

5.1 The modon free mode

During the block's dipole stage, the scatter diagrams are reminiscent of those of a geostationary, equivalent barotropic modon embedded in a westerly flow. We test the applicability of the modon free mode by examining the modon existence condition, and by calculating a modon radius. The input for these tests are the slopes of least-squares fit $q(\psi)$ lines from inside and outside the block, and the gravest eigenvalue of the vertical structure equation, equivalent to an internal deformation radius. The vertical structure equation arises from the separation of variables in the solution of the baroclinic modon, and we derive an analytic solution for it, using a power-law for the vertical static stability derived from our data.

Our results for the modon radius suggest it may be reasonable to consider the dipole stage of the block to be approaching the equivalent-barotropic modon free mode form. The computed radii are slightly larger than the actual block dimensions,

and this might be attributed to the inadequacy of the least-squares slopes in accurately representing the scatter plots for the interior region. We have also compared the theoretical and estimated separation of the modon vorticity maximum and minimum. This test gave poorer results: the measured separation was significantly greater. The asymmetry of the potential vorticity field, together with the fact that there is sometimes a multiplicity of extrema, make it difficult to define, let alone to measure, the dipole separation. However, the measured separation values are still well within the computed theoretical modon diameter.

The reliability of these tests is tempered by their sensitivity to the magnitude of the eigenvalue k_0. The value of k_0, corresponding to our estimated average lapse rate Γ = 5.23°C/km, is too small to satisfy the modon existence condition. Since smaller k_0 corresponds to greater static stability (i.e. a smaller lapse rate), our results suggest that a modon-type block cannot exist if the static stability is too high.

We have not found any *quantitative* evidence that associates the Omega-block stage with any particular free mode. The tests for the modon nature of the dipole stage cannot be applied to the Omega-block, and we are unaware of any other analytic, localized free modes that can be identified with the Omega-block form.

5.2 The baroclinicity

The scatter plots of 500 mb ψ versus absolute vorticity, ζ_a, are qualitatively quite similar to those with the potential vorticity, q. They show greater similarity during the dipole stage than for the Omega-block stage. We have computed the Root-Mean-Square contribution by the four lowest vertical normal modes to the eddy stream-function within the blocking region. The greatest contribution is that of the gravest mode, which is consistent with our observation that the flow appears to be equivalent barotropic. The contribution of the gravest mode increases as the Omega-block develops, and remains at an elevated level for its duration. The three higher modes all show a tendency opposite to that of the gravest mode.

The transition from the Omega to the dipole block is marked by a brief, discontinuous increase in the baroclinicity. We associate this increase with the intense cyclonic vortices that are entrained into the block, forming the cyclonic component of the dipole. We conclude that the dipole block is just as barotropic as the Omega-block, but that both stages of the block appear to be initiated by an

increased level of baroclinic activity.

5.3 Forecasting the block

We have found that the time series of the $q(\psi)$ plot area corresponds to the evolution of the block in a way that suggests the Omega and dipole forms are both free modes of the governing quasi-geostrophic equations. From Read et al. (1986) we know that this area in (ψ, q) space is analytically equivalent to the net potential vorticity flux by the geostrophic wind across the corresponding area in physical space. The decrease in the flux preceding the formation of the Omega-block can be physically identified with an intense synoptic-scale cyclonic system emerging out of the Arctic Ocean and tracking southeastward across the North American continent. This vortex is clearly distinguished on the scatter diagrams as a steepening of the plot between January 27 through February 4. The same effect during initial blocking development was observed by Malanotte-Rizzoli and Hancock (1987) in their composite of 12 North Atlantic blocking episodes.

We see some similarity between this intense vortex and the barotropic jet used by Flierl et al. (1983) to generate modons in the laboratory. We are led to speculate whether the strong anticyclonic shear on the southwestern flank of the vortex is analogous to the shear on the edge of the barotropic jet that creates the anticyclonic component of the laboratory modon. We consider it possible that this disturbance played the role of a nonlinear up-scale forcing mechanism, described by Hansen and Chen (1982) as being crucial in the initial formation of some blocks.

The scatter diagrams cannot show the details of the energy transfer that would verify this hypothesis. However, it appears that the net vorticity flux across the blocking region must decrease in time if the atmosphere is approaching a free mode. Thus we propose that blocks might be successfully forecast when significant decreases in net geostrophic vorticity flux across the preferred blocking region are caused by synoptic scale systems that are associated with steepening of the $q(\psi)$ scatter plots.

5.4 Suggestions for further study

It would be interesting to study more blocking episodes, to see whether our conclusions are generally applicable, or merely peculiar to this particular block. At this point the technique we have used seems useful, and is relatively straightforward to implement.

During the course of this work a number of possibilities for improvement have been noted. Our method of dividing the data region into the interior and exterior, could be improved by changing the shape of the box. However, considerable experimentation is required to position it in such a way that it contains the block on as many days as possible. The scatter plots and least-squares lines derived for an *elliptic* interior (not shown) were found to differ very little from the results obtained using a fixed box. Without a sophisticated computer work-station, it was considered too time-consuming to try to find the best possible interior. Except for the calculation of the 5-day averaged stream-function and vorticity fields, which were calculated using the University of Alberta's Amdahl mainframe, all of our results were obtained on a microcomputer with an 80286 microprocessor, and minimal commercial software. A simple home-made animation routine proved to be very useful for perusing the many charts, especially for detecting transient synoptic-scale features.

Since we could only hope to successfully test the modon model during the rather brief dipole stage of the block, we took ample measures to compute 'good' least-squares $q(\psi)$ lines. In spite of this, we see in Appendix A2, that the interior region lines for the dipole period (February 18-22) do not look like they are steep enough. Experimentation showed that imposing a steeper slope on the interior line resulted in modon radii that were much closer to the actual dipole-block dimensions. It could be that our least squares method ought to be replaced by a different scheme.

We have noted previously that we could only compute useful values of potential vorticity at one level, 500 mb. Our computed 400 mb q appeared to suffer from error in the baroclinic term, which is probably because the data level immediately above it, 250 mb, was above the tropopause over the northern part of the data grid. With better vertical resolution, we could compute scatter plots at more levels, and this would enable us to make a better qualitative assessment of the vertical variation. In addition, we would have more accurate estimates of the quantities used in the

vertical normal modes calculations (e.g. static stability). The possibility of using an isentropic vertical coordinate may be worth considering, as it may yield more realistic streamlines than those of our isobaric vertical coordinate.

The smoothing and averaging techniques described in Chapter 3 could perhaps be improved upon. For example, a nine-point spatial smoother could be more effective than our five-point version. It is quite possible that using equal weights for the 5-day average smears some of the information out over time, an error which could be reduced by increasing the weight for the day on which each average is centred. However, we note that Mak (1991) has successfully used a running ten-day mean of 500 mb data as an estimate of a blocking component, for a blocking energetics analysis. It is uncertain whether changes to the smoothing methods would significantly affect our final results, and no experimentation was done in this regard.

It is uncertain what the result of including topography in a study such as ours would be. Such a move might only obscure some of the fundamental findings, due to the increased complexity in both the analysis and computations.

References

Arfken, G., 1985: *Mathematical methods for physicists, 2nd edition*. Academic Press, Orlando, Florida, 985 pp.

Arnol'd, V.I., 1966: On an a priori estimate in the theory of hydrodynamical stability. *Izvestia Uchebn. Zaved. Matematika*, **54**, 3-5 (in Russian). English translation, 1969: *American Mathematical Society Translations Series 2*, **79**, 267-269.

Austin, J.F., 1980: The blocking of mid-latitude westerly winds by planetary waves. *Quarterly Journal of the Royal Meteorological Society*, **106**, 327-351.

Baines, P.G., 1983: A survey of blocking mechanisms, with application to the Australian region. *Australian Meteorological Magazine*, **31**, 27-36.

Bender, C.M., Orszag, S.A., 1978: *Advanced mathematical methods for scientists and engineers*, McGraw-Hill, New York, 593pp.

Butchart, N., Haines, K., Marshall, J.C., 1987: A theoretical and diagnostic study of solitary waves and atmospheric blocking. *Journal of the Atmospheric Sciences*,**46**, 2063-2078.

Canadian Climate Centre, 1989: *Climatic perspectives*, **11**, nos. 1-9.

Carnavale, F.C., Vallis, G.K., Purini, R., Briscolini, M., 1988: Propagation of barotropic modons over topography. *Geophysical and Astrophysical Fluid Dynamics*, **41**, 45-101.

Chang, J.-H., 1972: *Atmospheric circulation systems and climates*. The Oriental Publishing Company, Honolulu, Hawaii, 328pp.

d'Amours, R., 1989: *The Monthly Review*, Canadian Meteorological Centre, May, 1989.

Dole, R.M., Gordon, N.D, 1983: Persistent anomalies of the extratropical Northern Hemisphere wintertime circulation: Geographical distribution and regional

persistence characteristics. *Monthly Weather Review*, **111**, 1567-1586.

Flierl, G.R., 1987: Isolated eddy models in geophysics. *Annual Reviews in Fluid Mechanics*, **19**, 493-530.

Flierl, G.R., Stern, M.E., Whitehead, J.A., 1983: The physical significance of modons: Laboratory experiments and general integral constraints. *Dynamics of Atmospheres and Oceans*, **7**, 233-263.

Flierl, G.R., Larichev, V.D., McWilliams, J.C., Reznik, G.M., 1980: The dynamics of baroclinic and barotropic solitary eddies. *Dynamics of Atmospheres and Oceans*, **5**, 1-41.

Frederiksen, J.S., Bell, R.C., 1990: North Atlantic blocking during January 1979: Linear theory. *Quarterly Journal of the Royal Meteorological Society*, **116**, 1289-1313.

Haines, K., 1989: Baroclinic modons as prototypes for atmospheric blocking. *Journal of the Atmospheric Sciences*, **46**, 3202-3218.

Haines, K., Malanotte-Rizzoli, P., 1991: Isolated anomalies in westerly jetstreams: a unified approach. *Journal of the Atmospheric Sciences*, **48**, 510-526.

Haines, K., Marshall, J.C., 1987: Eddy-forced coherent structures as a prototype of atmospheric blocking. *Quarterly Journal of the Royal Meteorological Society*, **113**, 681-704.

Haltiner, G.J., Williams, R.T., 1980: *Numerical prediction and dynamic meteorology, 2nd ed.* J. Wiley & Sons, New York, 477pp.

Hansen, A.R., Chen, T.-C., 1982: Spectral energetics analysis of atmospheric blocking. *Monthly Weather Review*, **110**, 1146-1165.

Hildebrand, F.B., 1976: *Advanced calculus for applications, 2nd ed.* Prentice-Hall, Inc., Englewood Cliffs, NJ, 733pp.

Holmström, I., 1963: On a method for parametric representation of the state of the atmosphere. *Tellus*, **15**, 127-149.

Holmström, I., 1964: On the vertical structure of the atmosphere. *Tellus*, **16**, 288-308.

Holton, J.R., 1979: *An introduction to dynamic meteorology, 2nd ed.* Academic Press, New York, 391pp.

Hoskins, B.J., McIntyre, M.E., Robertson, A.W., 1985: On the use and significance of isentropic potential vorticity maps. *Quarterly Journal of the Royal Meteorological Society*, **111**, 877-946.

Illari, L., 1984: A diagnostic study of the potential vorticity in a warm blocking anticyclone. *Journal of the Atmospheric Sciences*, **41**, 3518-3526.

Illari, L., Marshall, J.C., 1983: On the interpretation of eddy fluxes during a blocking episode. *Journal of the Atmospheric Sciences*, **40**, 2232-2242.

Iribarne, J.V., Godson, W.L., 1981: *Atmospheric thermodynamics, 2nd ed.* D. Reidel, Dordrecht, Holland, 259pp.

Kung, E.C., Dacamara, C.C., Baker, W.E., Susskind, S., Park, C.-K., 1990: Simulations of winter blocking episodes using observed sea surface temperatures. *Quarterly Journal of the Royal Meteorological Society*, **116**, 1053-1070.

Larichev, V., Reznik, G., 1976: Two-dimensional Rossby soliton: an exact solution. *POLYMODE News, No. 19.*

Mak, M., 1991: Dynamics of an atmospheric blocking as deduced from its local energetics. *Quarterly Journal of the Royal Meteorological Society*, **117**, 477-493.

Malanotte-Rizzoli, P., Hancock, P.J., 1987: Coherent structures in a baroclinic atmosphere. Part IV: A comparison between theory and data. *Journal of the Atmospheric Sciences*, **44**, 2506-2529.

McIntyre, M.E., Shepherd, T.G., 1987: An exact local conservation theorem for finite-amplitude disturbances to non-parallel shear flows, with remarks on Hamiltonian structure and on Arnol'd's stability theorems. *Journal of Fluid Mechanics*, **181**, 527-565.

McWilliams, J.C., 1980: An application of equivalent modons to atmospheric blocking. *Dynamics of Atmospheres and Oceans*, **5**, 43-66.

Malguzzi P., Malanotte-Rizzoli, P., 1984: Nonlinear stationary Rossby waves on nonuniform zonal winds and atmospheric blocking. Part I: The analytical theory. *Journal of the Atmospheric Sciences*, **41**, 2620-2628.

Mendenhall, W., Scheaffer, R.L., Wackerly, D.D., 1981. *Mathematical statistics with applications, 2nd ed.* Duxbury Press, Boston, 686 pp.

Pedlosky, J., 1987: *Geophysical fluid dynamics, 2nd ed.* Springer-Verlag, New York, 710pp.

Pierrehumbert, R.T., Malguzzi, P., 1984: Forced coherent structures and local multiple equilibria in a barotropic atmosphere. *Journal of the Atmospheric Sciences*, **41**, 246-257.

Quiroz, R.S.,1987: Travelling waves and regional transitions in blocking activity in the northern hemisphere, *Monthly Weather Review*, **115**, 919-935.

Read, P.L., Rhines, P.B., White, A.A., 1986: Geostrophic scatter diagrams and potential vorticity dynamics. *Journal of the Atmospheric Sciences*, **43**, 3226-3240.

Rex, D., 1950: Blocking action in the middle troposphere and its effect upon regional climate, I. *Tellus*, **2**, 196-211.

Shukla, J., 1986: SST anomalies and blocking. *Advances in Geophysics*, **29**, Academic Press, 135-161.

Shutts, G.J., 1983: The propagation of eddies in diffluent jetstreams: eddy vorticity forcing of 'blocking' flow fields. *Quarterly Journal of the Royal Meteorological Society*, **109**, 737-761.

Shutts, G.J., 1986: A case study of eddy forcing during an Atlantic blocking episode. *Advances in Geophysics*, **29**, Academic Press, 135-161.

Stern, M.E., 1975: Minimal properties of planetary eddies. *Journal of Marine*

Research, **33**, 1-13.

Swaters, G.E., 1989: A perturbation theory for the solitary-drift-vortex solutions of the Hasegawa-Mima equation. *Journal of Plasma Physics*, **41**, 523-539.

Swaters, G.E., 1986: Barotropic modon propagation over slowly varying topography. *Geophysical and Astrophysical Fluid Dynamics*, **36**, 85-113.

Swaters, G.E. and Flierl, G.R., 1989: Ekman dissipation of a barotropic modon. *Mesoscale/Synoptic Coherent Structures in Geophysical Turbulence*, J. Nihoul, B. Jamont, eds. Elsevier, 149-165.

Tribbia, J., 1984: Modons in spherical geometry. *Geophysical and Astrophysical Fluid Dynamics*, **30**, 131-168.

Wallace, J.M., Blackmon, M.L., 1983: Observations of low-frequency atmospheric variability. *Large-scale dynamical processes in the atmosphere*, B.J. Hoskins, R.P. Pearce, eds., Academic Press.

Zauderer, E., 1989: *Partial differential equations of applied mathematics, 2nd ed.* John Wiley & Sons, 891 pp.

Appendix A1

Vorticity flux, q(ψ) plot area, and Least squares q(ψ) slope-intercept values

Day	Net Flux	Area	$q(0)_{int}$	$dq(0)/d\psi_{int}$	$q(0)_{ext}$	$dq(0)/d\psi_{ext}$
	[both $\times 10$ m^2s^{-2}]		[$\times 10^{-3}s^{-1}$]	[$\times 10^{-12}m^{-2}s$]	[same units]	
23/01	-6.1636	-3.55600	1.6596	-3.7897	1.5998	-3.6027
24/01	-10.0620	-6.71670	1.6141	-3.6763	1.5823	-3.5634
25/01	-16.4842	-13.03210	1.8058	-4.1475	1.5131	-3.3997
26/01	-24.3497	-22.47345	1.9977	-4.6099	1.4365	-3.2166
27/01	-27.1684	-26.43655	2.0198	-4.6364	1.3975	-3.1233
28/01	-28.5056	-27.88045	2.1938	-5.0270	1.3667	-3.0483
29/01	-17.5698	-17.12315	2.2755	-5.1802	1.3339	-2.9670
30/01	-4.8519	-4.73500	2.3561	-5.3272	1.3378	-2.9720
31/01	-1.5632	-0.65015	2.7229	-6.1667	1.3294	-2.9484
01/02	7.0535	7.81065	2.8132	-6.3467	1.3449	-2.9836
02/02	18.2464	19.04675	2.6533	-5.9407	1.3263	-2.9380
03/02	21.4353	22.71870	2.7213	-6.0769	1.3648	-3.0291
04/02	14.9903	16.82730	2.6989	-6.0113	1.3430	-2.9754
05/02	9.9885	11.26560	2.1071	-4.6416	1.3396	-2.9662
06/02	6.0441	6.92060	1.5979	-3.4773	1.2935	-2.8549
07/02	2.9308	3.75150	1.4040	-3.0440	1.2445	-2.7369
08/02	0.4612	1.58005	1.1456	-2.4605	1.1570	-2.5264
09/02	-1.4728	-0.71670	1.0112	-2.1566	1.1354	-2.4742
10/02	-2.2679	-1.45090	0.8316	-1.7447	1.1482	-2.5034
11/02	-2.6255	-1.34980	1.0307	-2.2088	1.1896	-2.5996
12/02	-4.0925	-3.23330	1.3079	-2.8490	1.2313	-2.6950
13/02	-5.4182	-5.32290	1.7396	-3.8431	1.2767	-2.7976
14/02	-3.4217	-3.65910	2.1346	-4.7522	1.2793	-2.7992
15/02	-1.6350	-2.71780	2.4400	-5.4589	1.2653	-2.7646
16/02	-0.1035	-2.06030	2.8482	-6.4172	1.2955	-2.8391
17/02	0.2958	-1.74235	3.3643	-7.6474	1.3365	-2.9411
18/02	1.3210	-0.20015	4.2258	-9.6973	1.3394	-2.9525
19/02	-0.6857	-1.65720	5.2677	-12.184	1.3165	-2.8993
20/02	-4.9240	-5.23280	5.7304	-13.358	1.2756	-2.8006
21/02	-4.1932	-4.16350	5.1168	-11.944	1.1944	-2.6033

Day	Net Flux	Area	$q(0)_{int}$	$dq(0)/d\psi_{int}$	$q(0)_{ext}$	$dq(0)/d\psi_{ext}$
22/02	-5.0030	-4.73520	2.5702	-5.8714	1.1362	-2.4612
23/02	-2.8794	-2.86960	1.7104	-3.8084	1.1227	-2.4264
24/02	-0.6901	-1.32115	1.6662	-3.6776	1.1533	-2.4985
25/02	-0.0096	-1.24275	1.5820	-3.4520	1.2001	-2.6098
26/02	0.6186	-0.49910	1.6456	-3.5773	1.3067	-2.8633

Appendix A1 (continued)

Root-Mean-Square Values of the Vertical Normal Modes Fourier Coefficients

Fourier coefficients of estimated eddy stream-function, normalized so that the daily sum of their squares is unity. The root-mean-square is computed over the rectangular region bounded by latitudes 46° to 70°N and longitudes 114° to 166°W.

Day	$<a_0>_{rms}$	$<a_1>_{rms}$	$<a_2>_{rms}$	$<a_3>_{rms}$
23/01	0.959959209	0.255723208	0.101930521	0.051904764
24/01	0.966226637	0.235311270	0.094386637	0.046106376
25/01	0.964077115	0.243684441	0.094240062	0.047874130
26/01	0.966400862	0.239233434	0.081858069	0.046217646
27/01	0.974848092	0.207767516	0.071245097	0.037787978
28/01	0.981886566	0.163994133	0.089694157	0.030977605
29/01	0.982276559	0.138646960	0.120523833	0.037201088
30/01	0.966650426	0.209538698	0.136924773	0.054149218
31/01	0.956916332	0.252632678	0.129829675	0.060267456
01/02	0.961064219	0.248923078	0.105921432	0.056334622
02/02	0.968364298	0.230111897	0.082850091	0.049547754
03/02	0.973805428	0.213754401	0.064508684	0.043019649
04/02	0.979493141	0.192270458	0.047398590	0.037127901
05/02	0.984482527	0.169638753	0.031708635	0.031801742
06/02	0.988443017	0.147863895	0.019962026	0.026797134
07/02	0.990338564	0.135853142	0.014278494	0.023865337
08/02	0.991490364	0.127943739	0.010787708	0.021464735
09/02	0.991701603	0.126668990	0.007359223	0.020710792
10/02	0.990274191	0.137202248	0.007536775	0.021811062
11/02	0.988750637	0.147400483	0.008864786	0.023804642
12/02	0.988461792	0.149215326	0.010069428	0.024017248
13/02	0.989677131	0.140830189	0.013502967	0.022884822
14/02	0.989450037	0.139383152	0.030205755	0.025469182
15/02	0.991272867	0.119417891	0.041532733	0.037317187
16/02	0.990969121	0.110926397	0.055586919	0.050848059
17/02	0.985504389	0.131506994	0.078460544	0.073012985

Day	$<a_0>_{rms}$	$<a_1>_{rms}$	$<a_2>_{rms}$	$<a_3>_{rms}$
18/02	0.985998929	0.125507325	0.080209740	0.074969307
19/02	0.986201108	0.117334634	0.085240334	0.079837635
20/02	0.996520221	0.074689753	0.030884506	0.020372218
21/02	0.997689366	0.057641070	0.030934868	0.018345119
22/02	0.997737706	0.062917724	0.020405199	0.012021209
23/02	0.996054769	0.086852454	0.015389882	0.009734389
24/02	0.994053304	0.106588349	0.018712182	0.012111594
25/02	0.990697742	0.131833881	0.028317036	0.018328514
26/02	0.991018414	0.128302544	0.032037321	0.019860523

Appendix A2

500 mb vorticity-stream-function scatter plots, and stream-function and vorticity contour charts

On the following pages the full set (January 23 through February 26) of daily scatter plots is presented, together with contour charts of geostrophic stream-function and potential vorticity. The following remarks apply:

(a) All quantities are five-day averages centred on the date written in the centre of the page. There are three pictures for each day: geostrophic stream-function versus absolute vorticity, geostrophic stream-function versus potential vorticity, and contour chart with stream-function and potential vorticity.

(b) Vorticity-stream-function values from within the box-region outlined on the contour charts have been plotted as crosses (+), while the values from outside this region are denoted by dots (·). This blocking region has been subjectively defined to be bounded by latitudes 46°N and 70°N and longitudes 114°W and 160°W.

(c) The stream-function contours are heavy solid lines, and the potential vorticity contours are light dashed lines. The contour interval for stream-function is 6×10^6 $m^2 s^{-2}$, while that of potential vorticity is 2×10^{-5} s^{-1}.

(d) The contour charts do not include the Atlantic region, between 20°W and 40°W, due to computer graphics limitations.

(f) The points in physical space, for which (ψ,q) values for the least-squares lines are estimated, have a constant zonal separation equal to 192 km (the zonal grid spacing at 30°N). The points from which the scatter plots have been constructed are spaced approximately evenly in the east-west direction.

(g) The least-squares q(ψ) lines are drawn on the q(ψ) scatter diagram. The line for (ψ,q) values from outside the blocking region is solid, while the line for the interior (ψ,q) values is dashed.

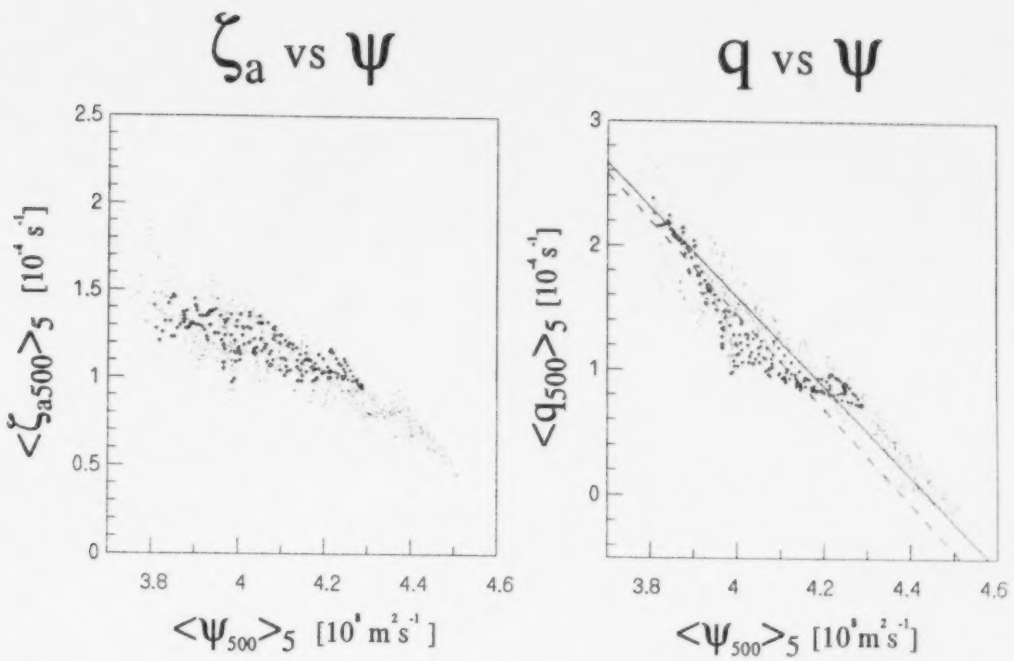
ζa vs ψ
q vs ψ
<ζa500>5 [10-4 s-1]
<q500>5 [10-4 s-1]
<ψ500>5 [10⁶ m² s-1]
<ψ500>5 [10⁶ m² s-1]
2.5
2
1.5
1
0.5
0
3
2
1
0
3.8
4
4.2
4.4
4.6

January 23

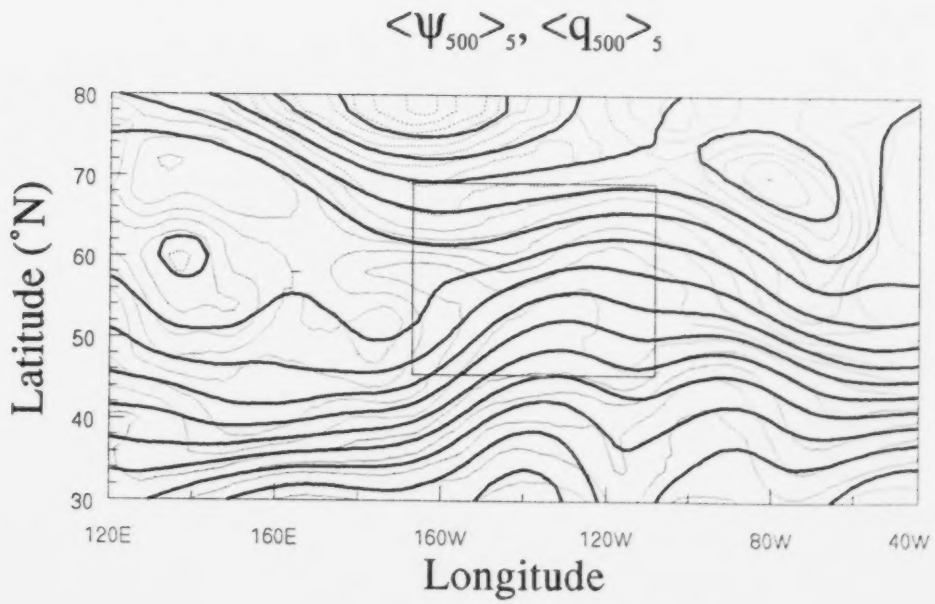
<ψ500>5, <q500>5
Latitude (°N)
80
70
60
50
40
30
120E
160E
160W
120W
80W
40W
Longitude

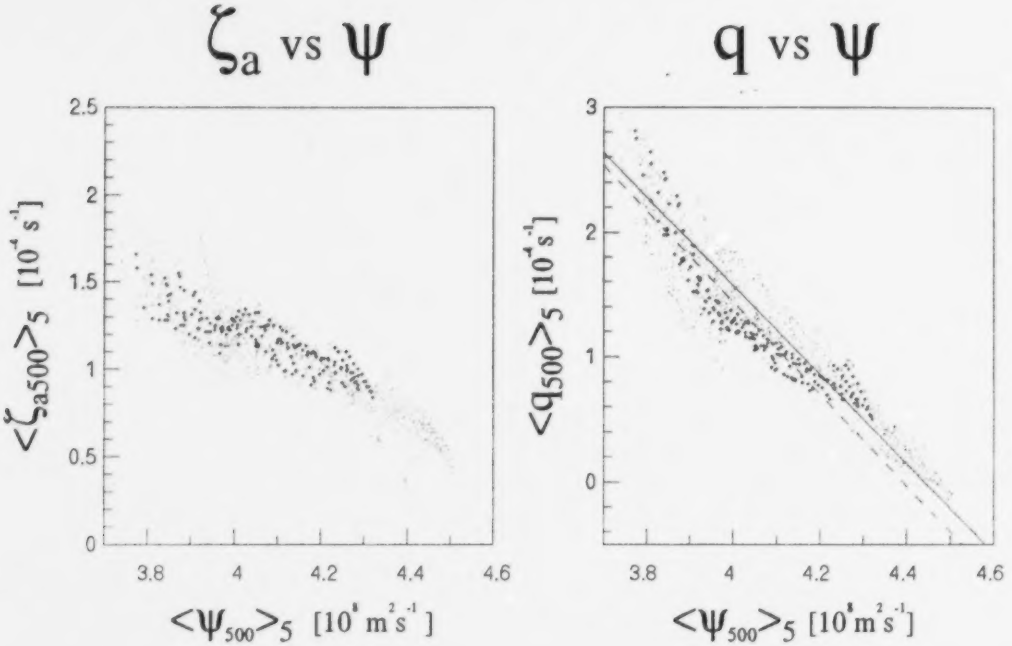
ζa vs ψ
q vs ψ
<ζa500>5 [10-4 s-1]
<q500>5 [10-4 s-1]
<ψ500>5 [10⁸ m²s-1]
<ψ500>5 [10⁸ m²s-1]
2.5
2
1.5
1
0.5
0
3
2
1
0
3.8
4
4.2
4.4
4.6

January 24

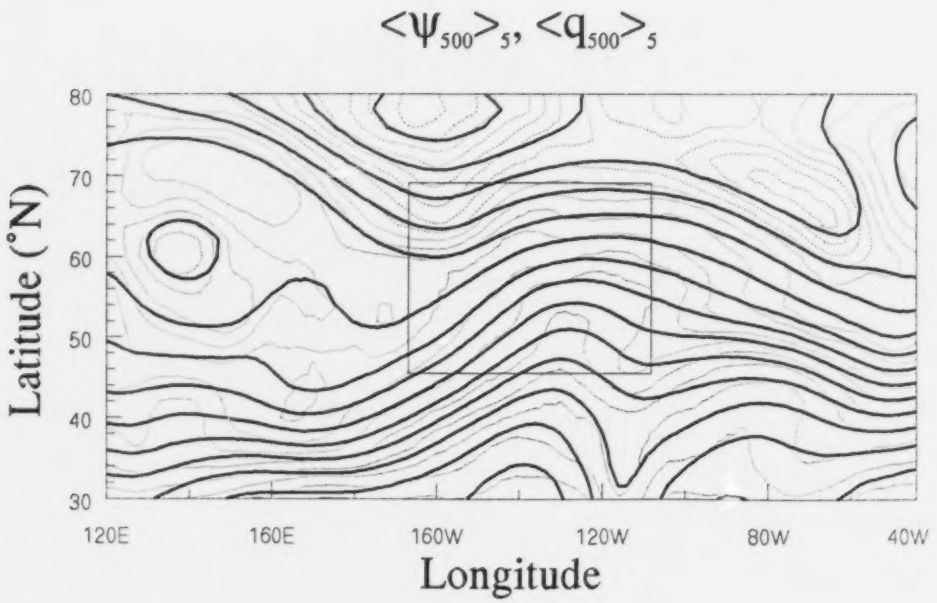
<ψ500>5, <q500>5
Latitude (°N)
80
70
60
50
40
30
120E
160E
160W
120W
80W
40W
Longitude

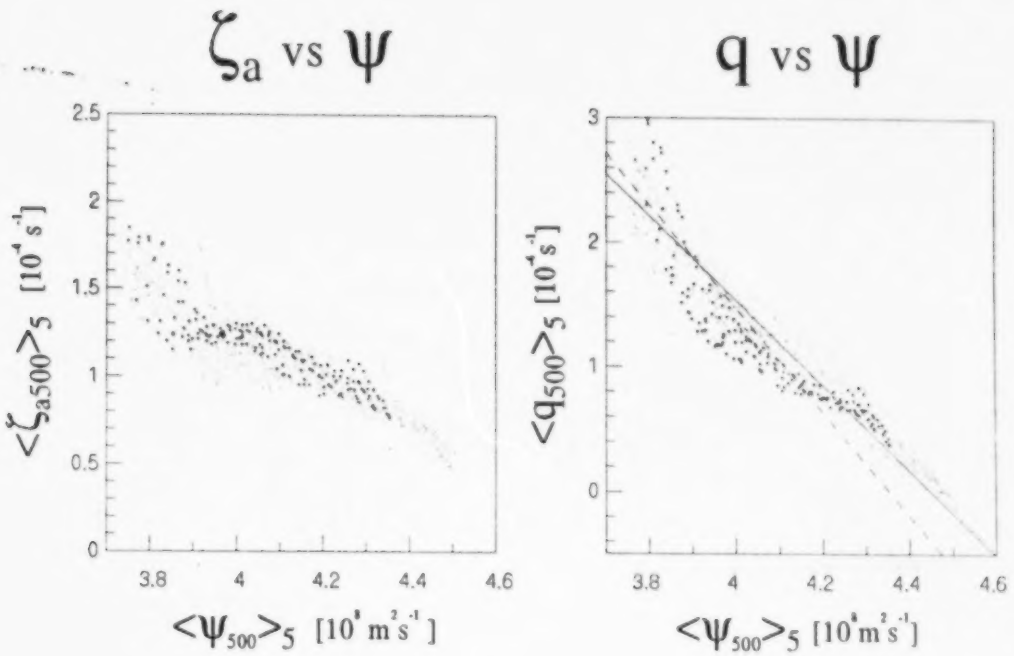
ζ_a vs ψ
q vs ψ
$<\zeta_{a500}>_5$ [10^{-4} s^{-1}]
$<q_{500}>_5$ [10^{-4} s^{-1}]
$<\psi_{500}>_5$ [10^6 $m^2 s^{-1}$]
$<\psi_{500}>_5$ [10^6 $m^2 s^{-1}$]
2.5
2
1.5
1
0.5
0
3
2
1
0
3.8
4
4.2
4.4
4.6

January 25

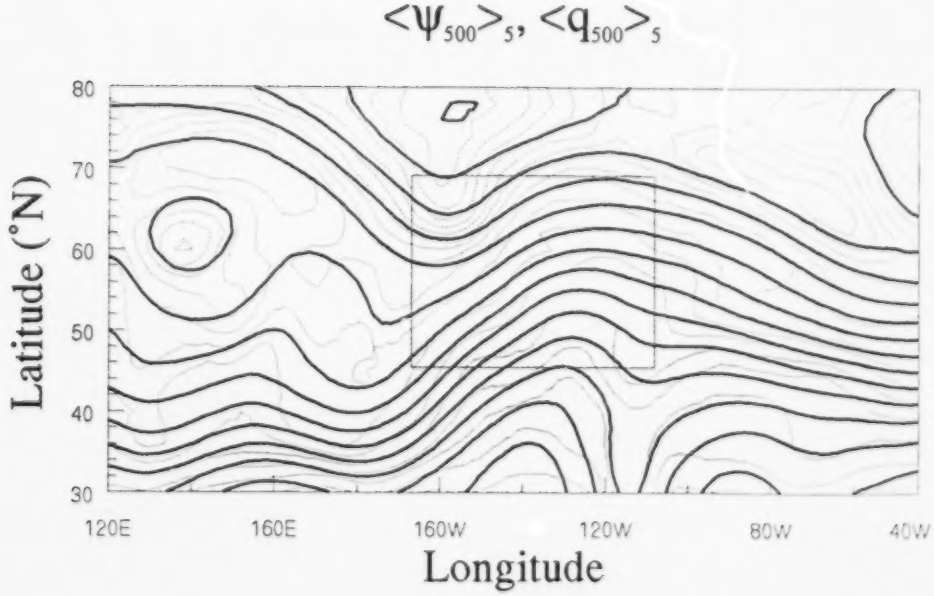
$<\psi_{500}>_5$, $<q_{500}>_5$
Latitude (°N)
80
70
60
50
40
30
120E
160E
160W
120W
80W
40W
Longitude

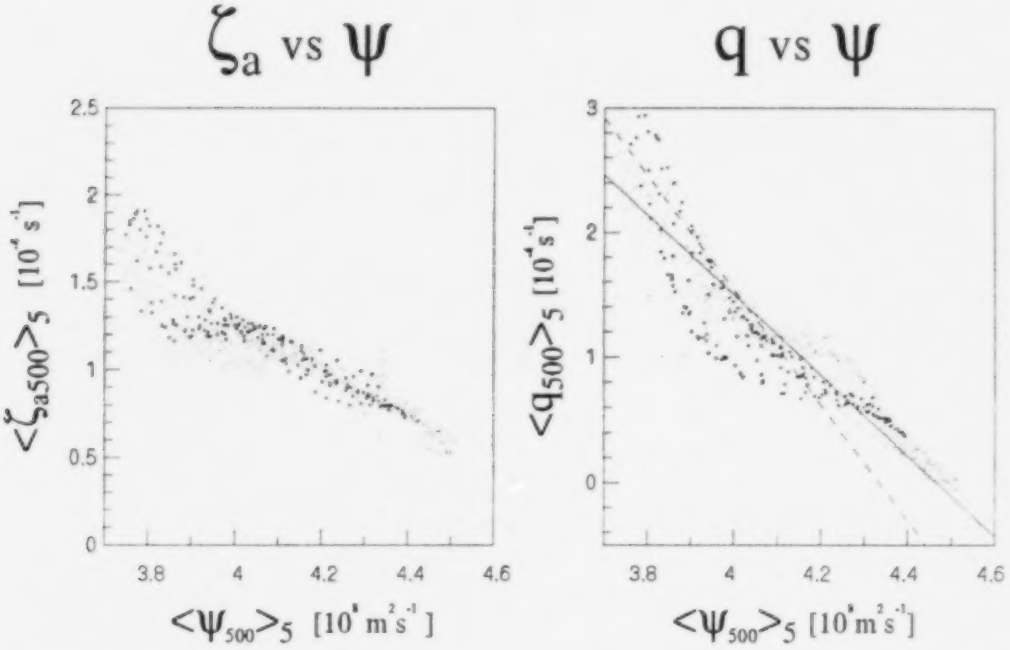
ζa vs ψ
q vs ψ
<ζa500>5 [10⁻⁴ s⁻¹]
<q500>5 [10⁻⁴ s⁻¹]
<ψ500>5 [10⁶ m² s⁻¹]
<ψ500>5 [10⁶ m² s⁻¹]
2.5
2
1.5
1
0.5
0
3
2
1
0
3.8
4
4.2
4.4
4.6

January 26

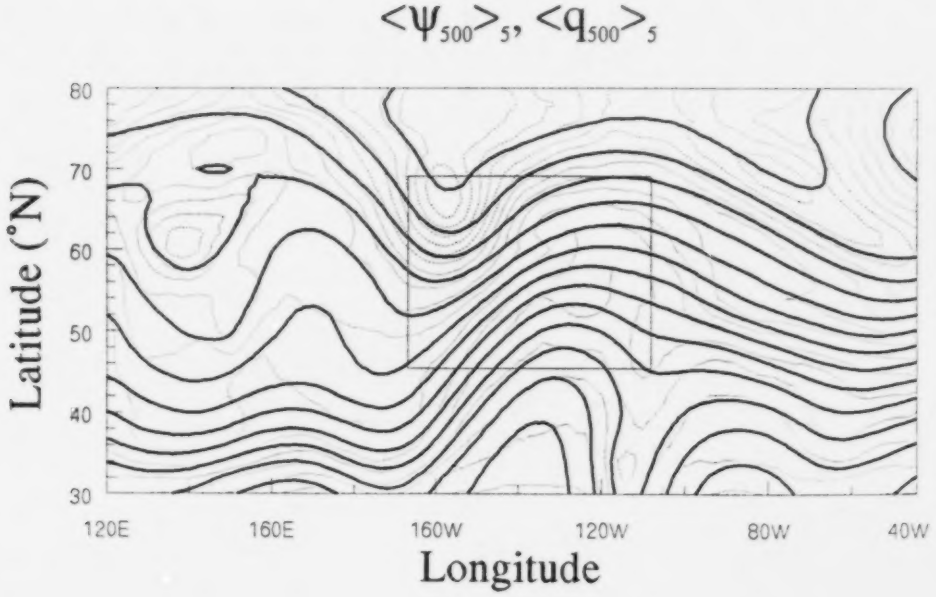
<ψ500>5, <q500>5
Latitude (°N)
80
70
60
50
40
30
120E
160E
160W
120W
80W
40W
Longitude

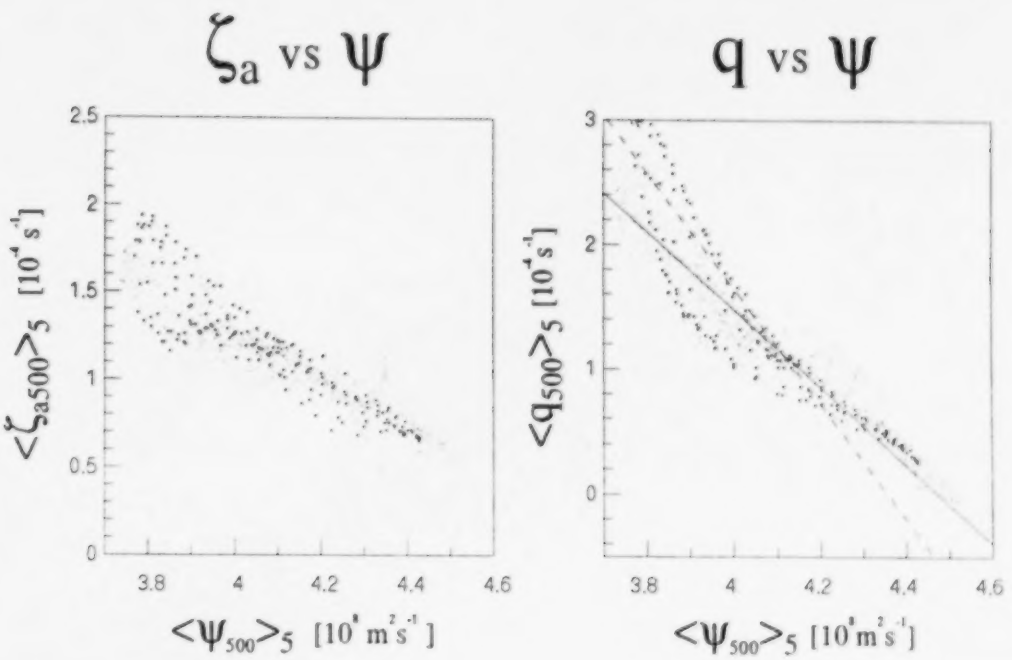
ζa vs ψ
q vs ψ
<ζa500>5 [10⁻⁴ s⁻¹]
<q500>5 [10⁻⁴ s⁻¹]
<ψ500>5 [10⁶ m²s⁻¹]
<ψ500>5 [10⁶ m²s⁻¹]
2.5
2
1.5
1
0.5
0
3
2
1
0
3.8
4
4.2
4.4
4.6

January 27

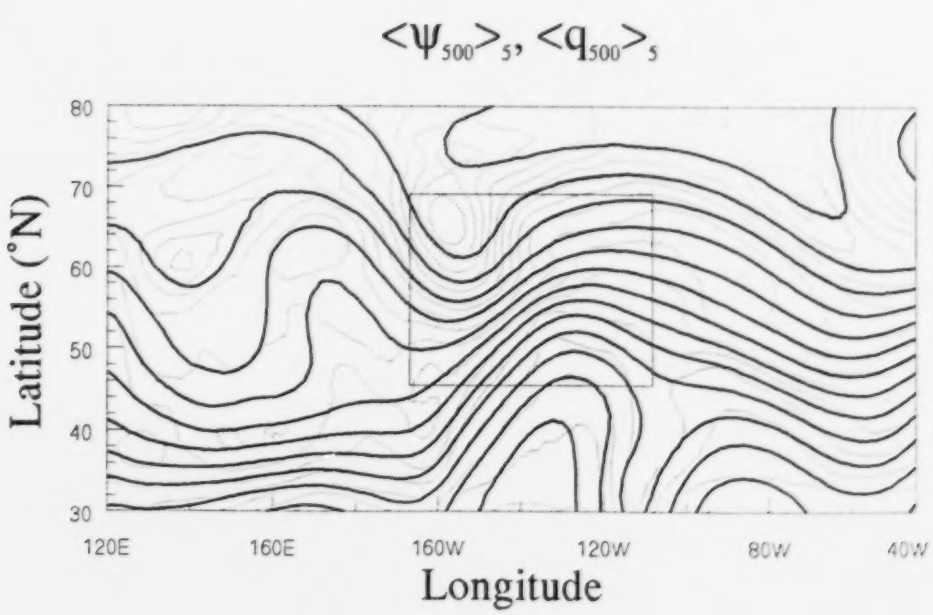
<ψ500>5, <q500>5
Latitude (°N)
80
70
60
50
40
30
120E
160E
160W
120W
80W
40W
Longitude

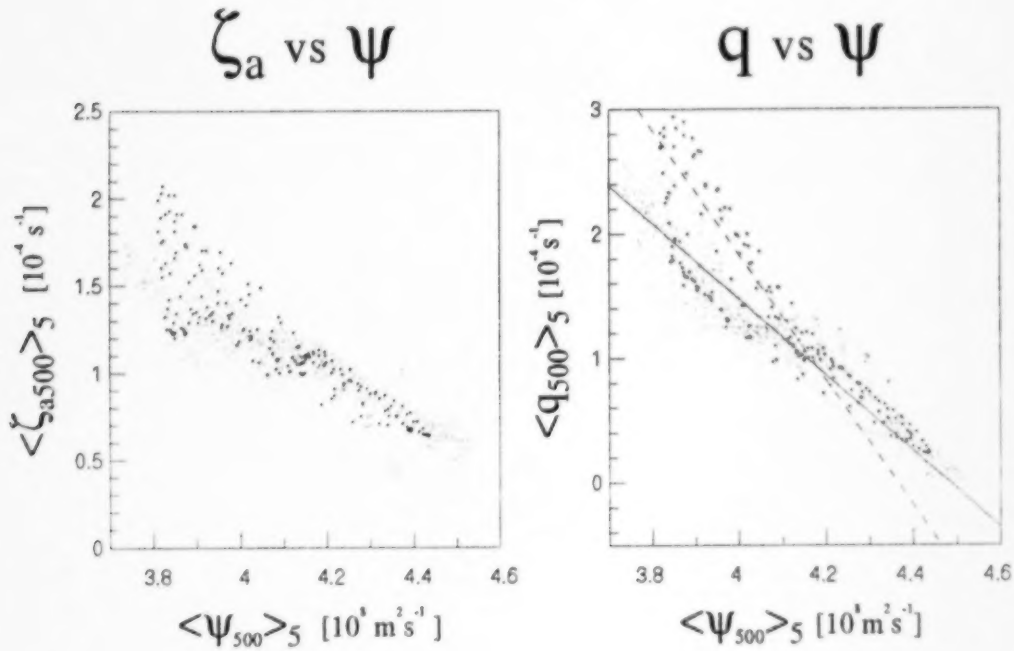
ζa vs ψ
q vs ψ
<ζa500>5 [10-4 s-1]
<q500>5 [10-4 s-1]
<ψ500>5 [10³ m² s-1]
<ψ500>5 [10³ m² s-1]
2.5
2
1.5
1
0.5
0
3
2
1
0
3.8
4
4.2
4.4
4.6

January 28

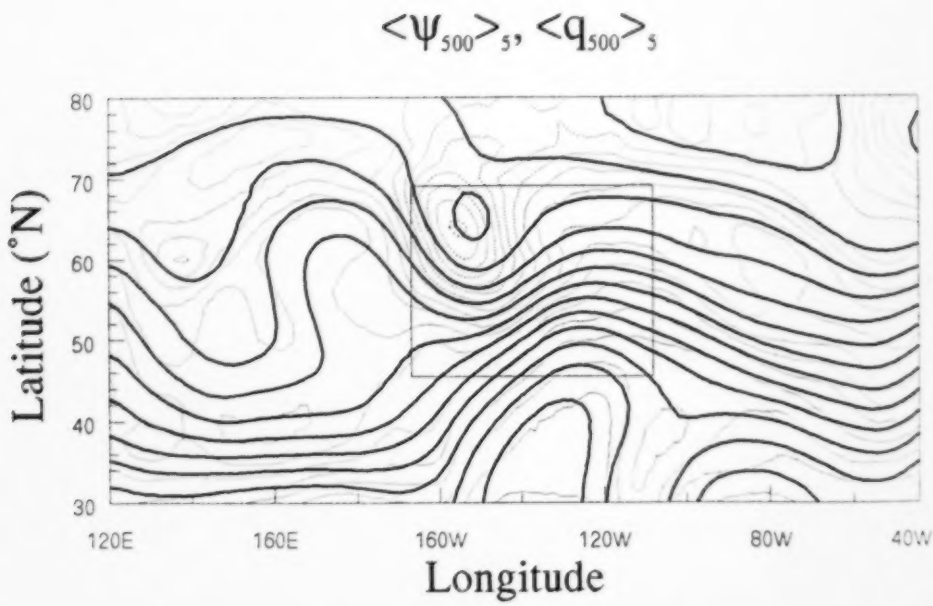
<ψ500>5, <q500>5
Latitude (°N)
80
70
60
50
40
30
120E
160E
160W
120W
80W
40W
Longitude

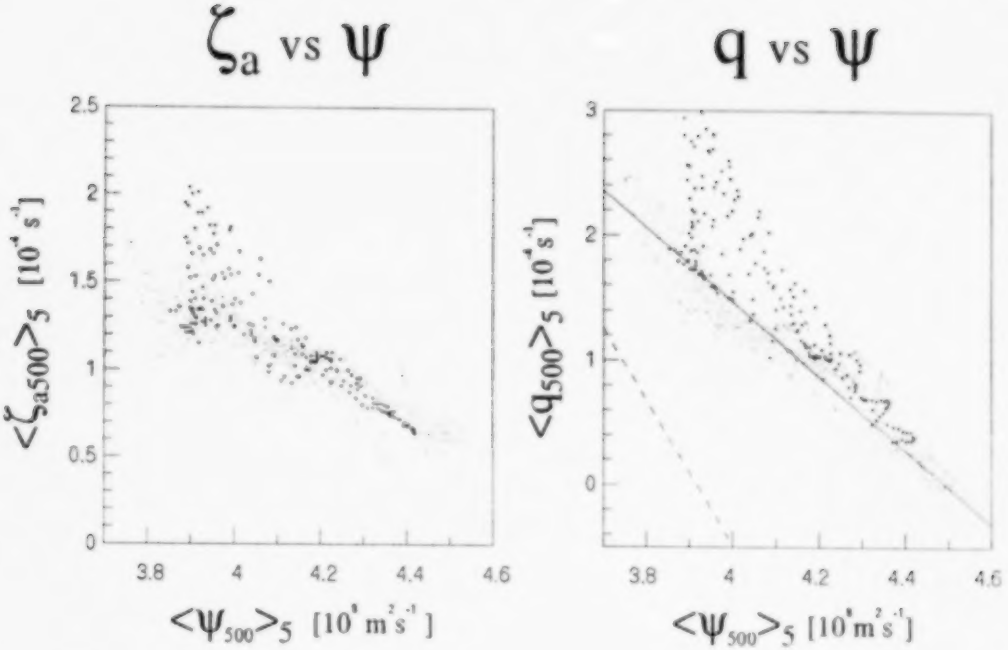
ζ_a vs ψ
q vs ψ
$<\zeta_{a500}>_5$ [10^{-4} s^{-1}]
$<q_{500}>_5$ [10^{-4} s^{-1}]
$<\psi_{500}>_5$ [10^6 $m^2 s^{-1}$]
$<\psi_{500}>_5$ [10^6 $m^2 s^{-1}$]

January 29

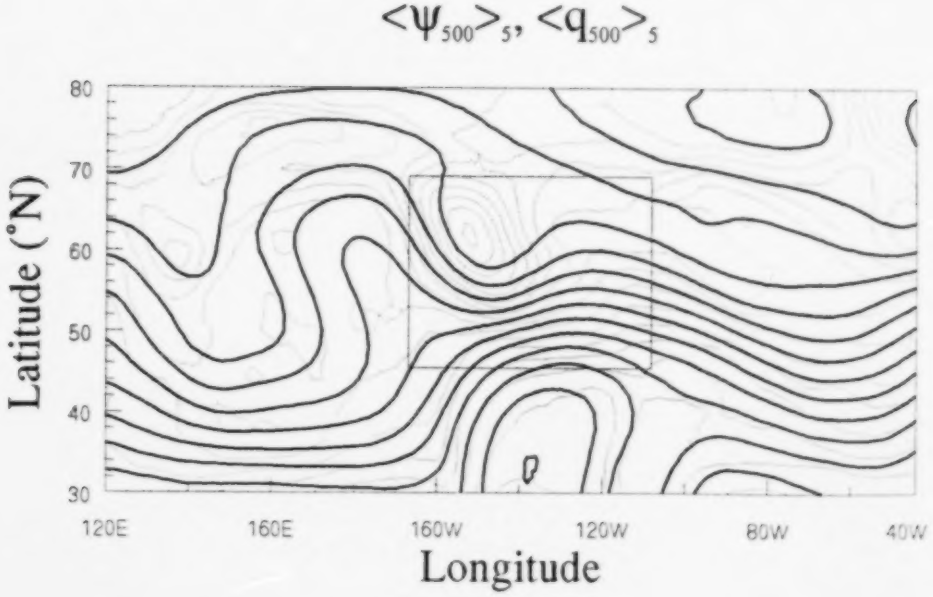
$<\psi_{500}>_5$, $<q_{500}>_5$
Latitude (°N)
Longitude
120E
160E
160W
120W
80W
40W

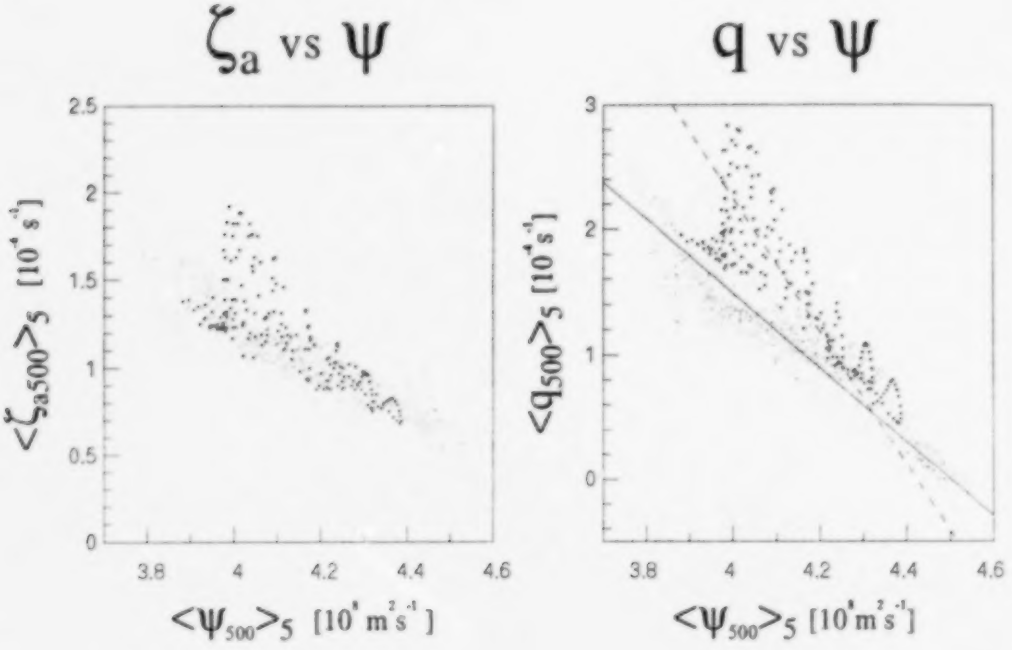
ζa vs ψ
q vs ψ
<ζa500>5 [10⁻⁶ s⁻¹]
<q500>5 [10⁻⁶ s⁻¹]
<ψ500>5 [10⁶ m² s⁻¹]
<ψ500>5 [10⁶ m² s⁻¹]

January 30

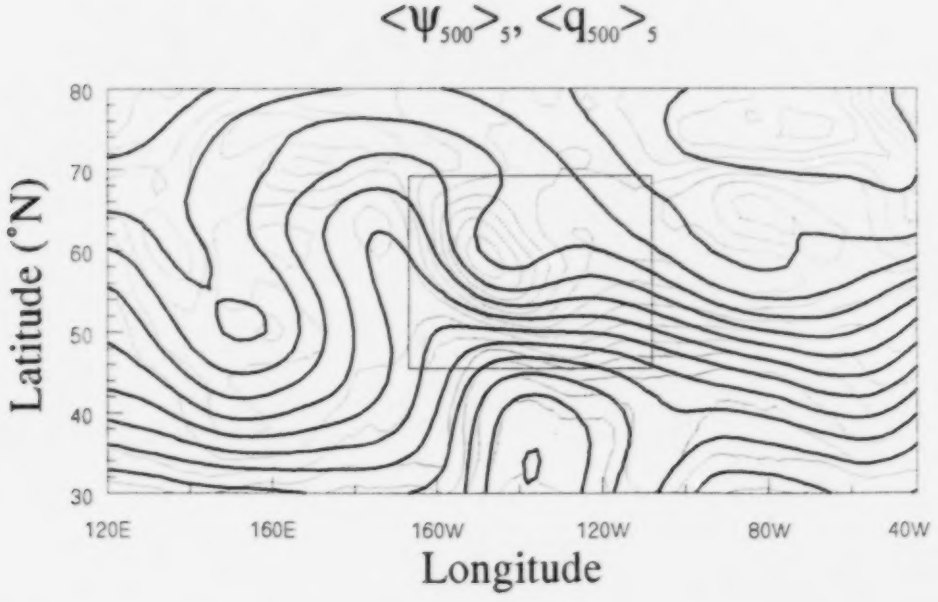
<ψ500>5, <q500>5
Latitude (°N)
Longitude
120E
160E
160W
120W
80W
40W

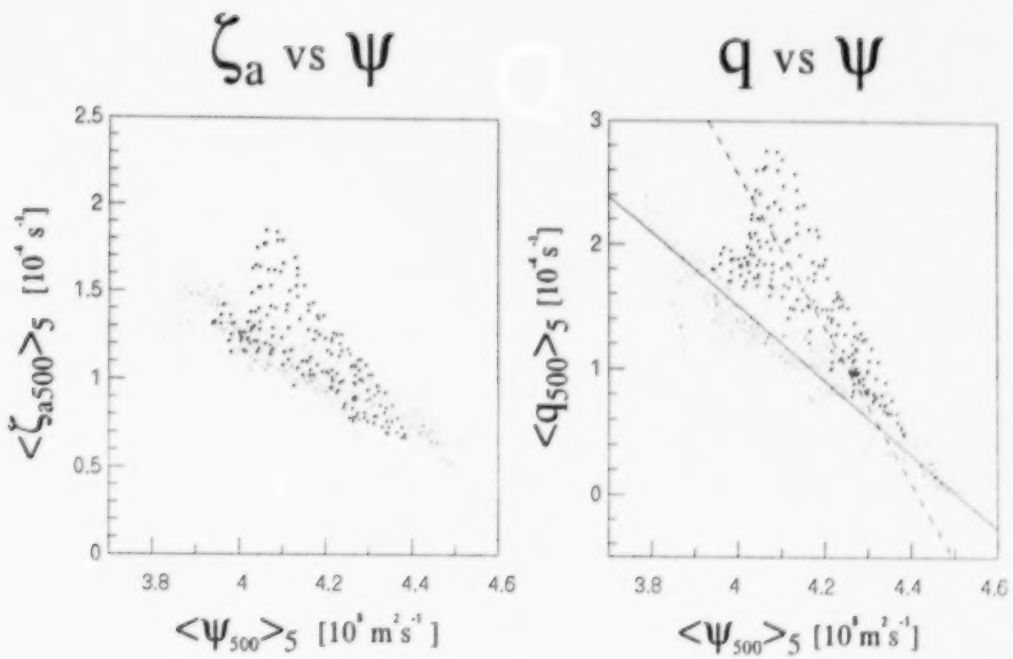
ζa vs ψ
q vs ψ
<ζa500>5 [10-4 s-1]
<q500>5 [10-4 s-1]
<ψ500>5 [10⁶ m²s-1]
<ψ500>5 [10⁶m²s-1]
2.5
2
1.5
1
0.5
0
3
3.8
4
4.2
4.4
4.6

January 31

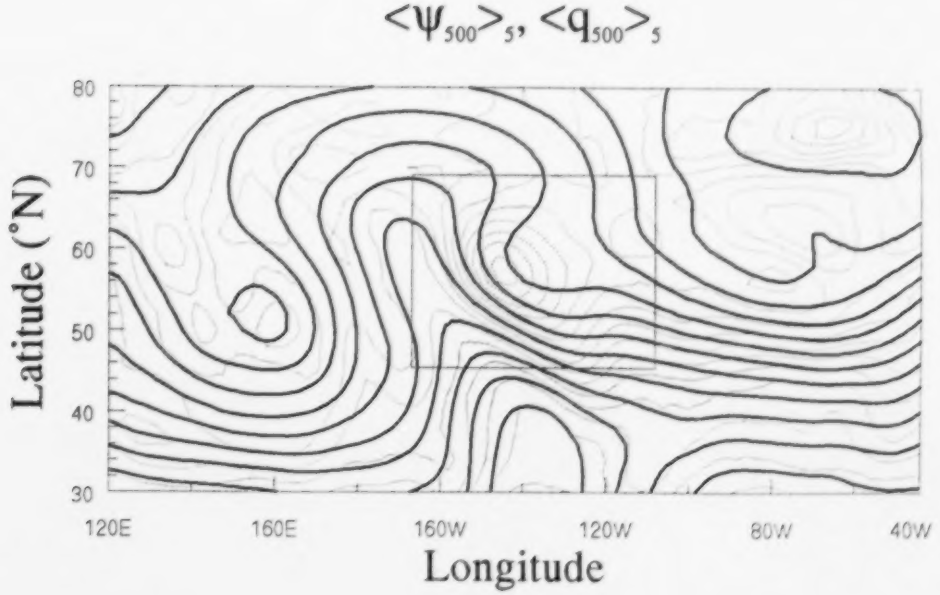
<ψ500>5, <q500>5
Latitude (°N)
80
70
60
50
40
30
120E
160E
160W
120W
80W
40W
Longitude

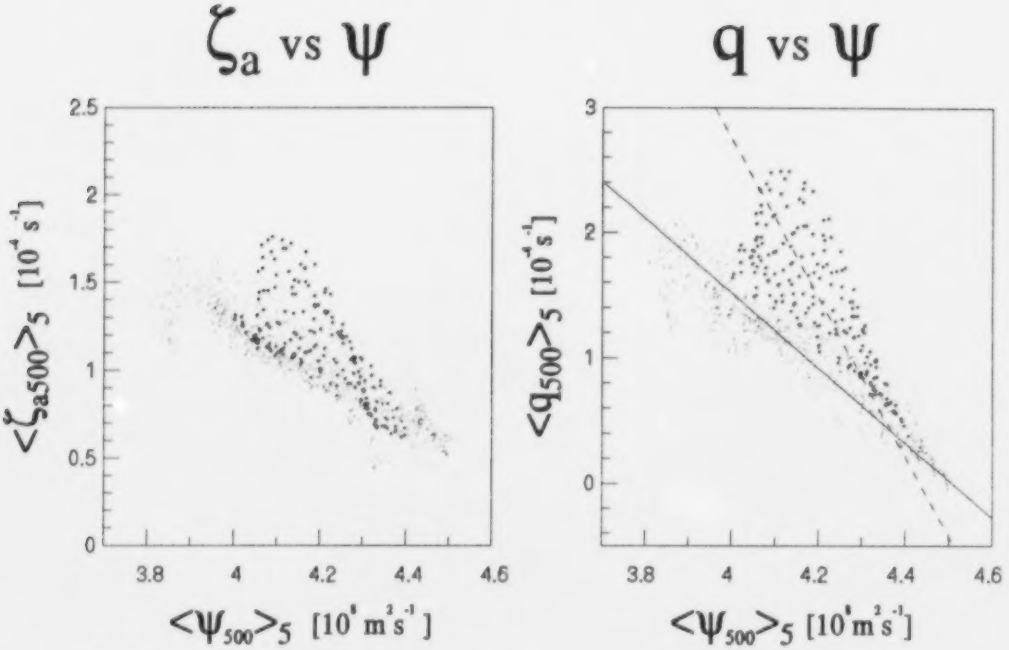
ζa vs ψ
q vs ψ
<ζa500>5 [10⁻⁴ s⁻¹]
<q500>5 [10⁻⁴ s⁻¹]
<ψ500>5 [10⁶ m² s⁻¹]
<ψ500>5 [10⁶ m² s⁻¹]
2.5
2
1.5
1
0.5
0
3
2
1
0
3.8
4
4.2
4.4
4.6

February 1

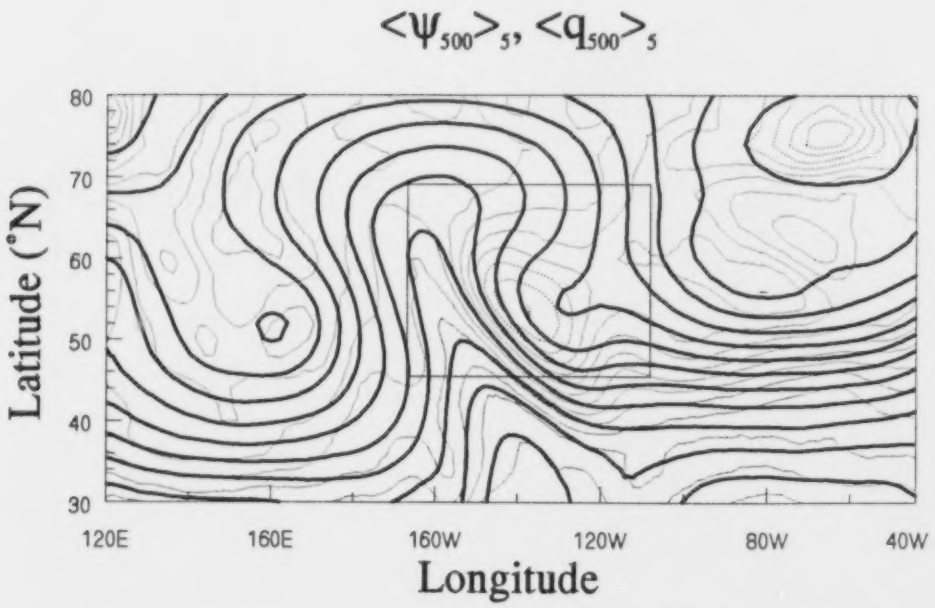
<ψ500>5, <q500>5
Latitude (°N)
80
70
60
50
40
30
120E
160E
160W
120W
80W
40W
Longitude

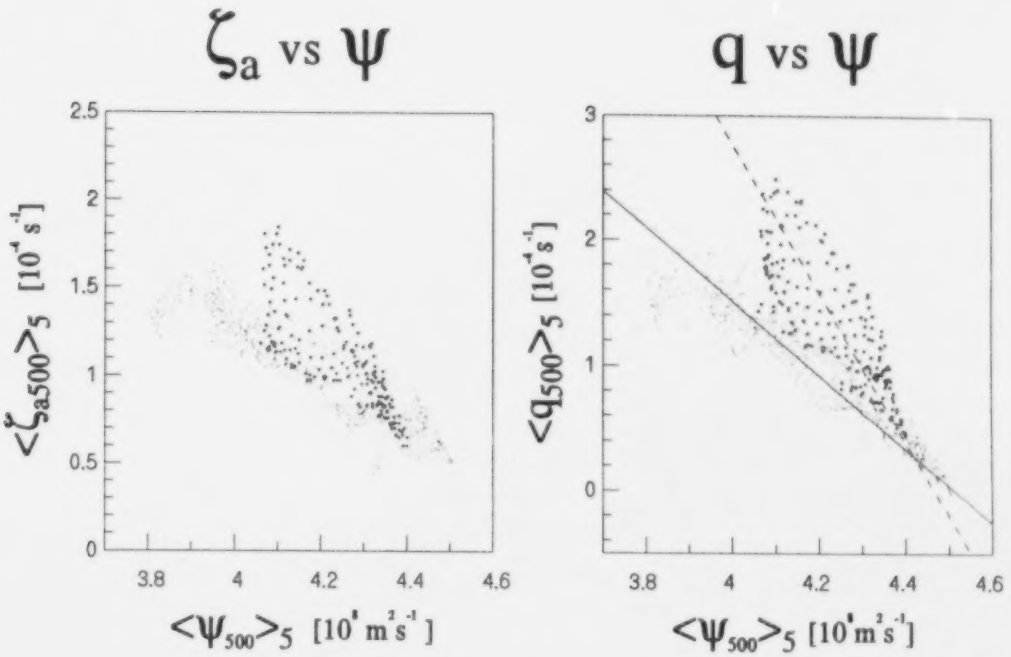
ζa vs ψ
q vs ψ
<ζa500>5 [10⁻⁴ s⁻¹]
<q500>5 [10⁻⁴ s⁻¹]
<ψ500>5 [10⁶ m² s⁻¹]
<ψ500>5 [10⁶ m² s⁻¹]
2.5
2
1.5
1
0.5
0
3
2
1
0
3.8
4
4.2
4.4
4.6

February 2

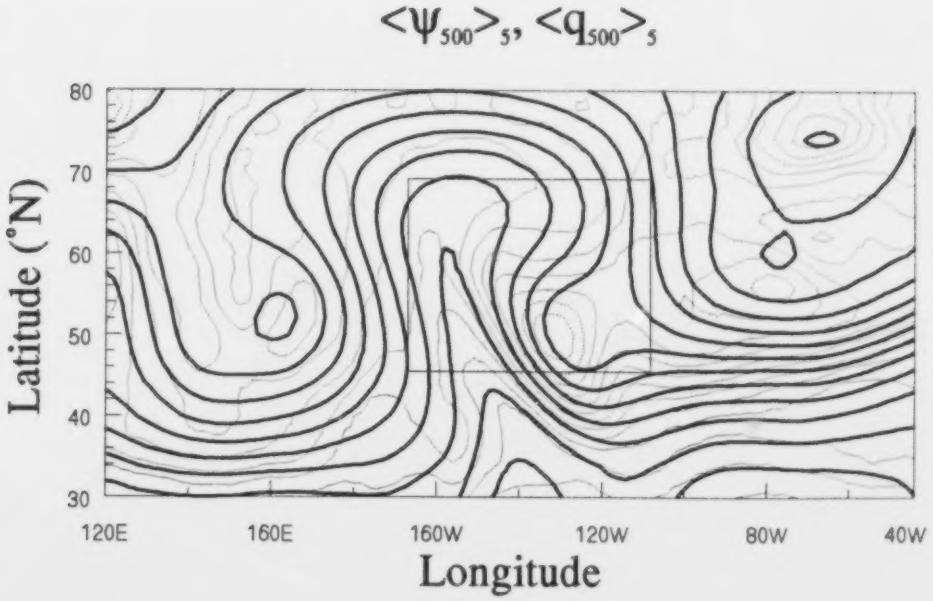
<ψ500>5, <q500>5
Latitude (°N)
80
70
60
50
40
30
120E
160E
160W
120W
80W
40W
Longitude

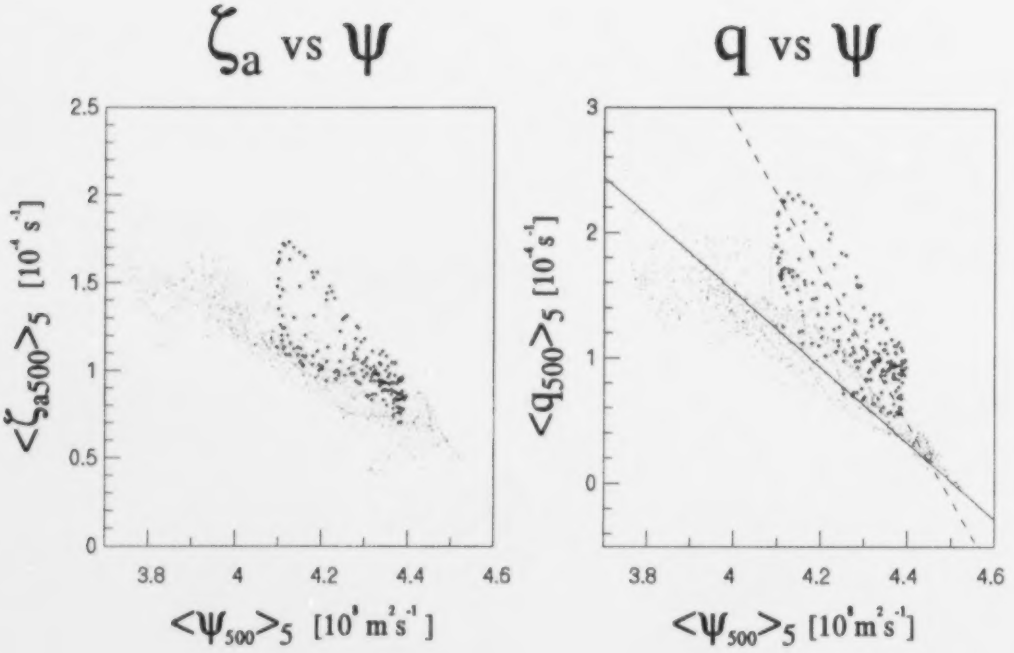
ζa vs ψ
q vs ψ
<ζa500>5 [10⁻⁴ s⁻¹]
<q500>5 [10⁻⁴ s⁻¹]
<ψ500>5 [10⁵ m² s⁻¹]
<ψ500>5 [10⁵ m² s⁻¹]
2.5
2
1.5
1
0.5
0
3
2
1
0
3.8
4
4.2
4.4
4.6

February 3

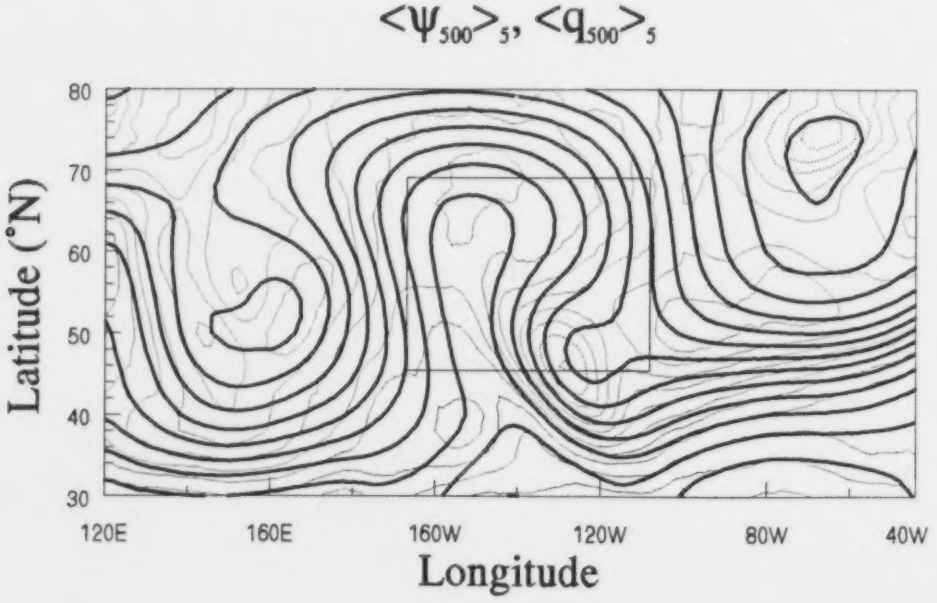
<ψ500>5, <q500>5
Latitude (°N)
80
70
60
50
40
30
120E
160E
160W
120W
80W
40W
Longitude

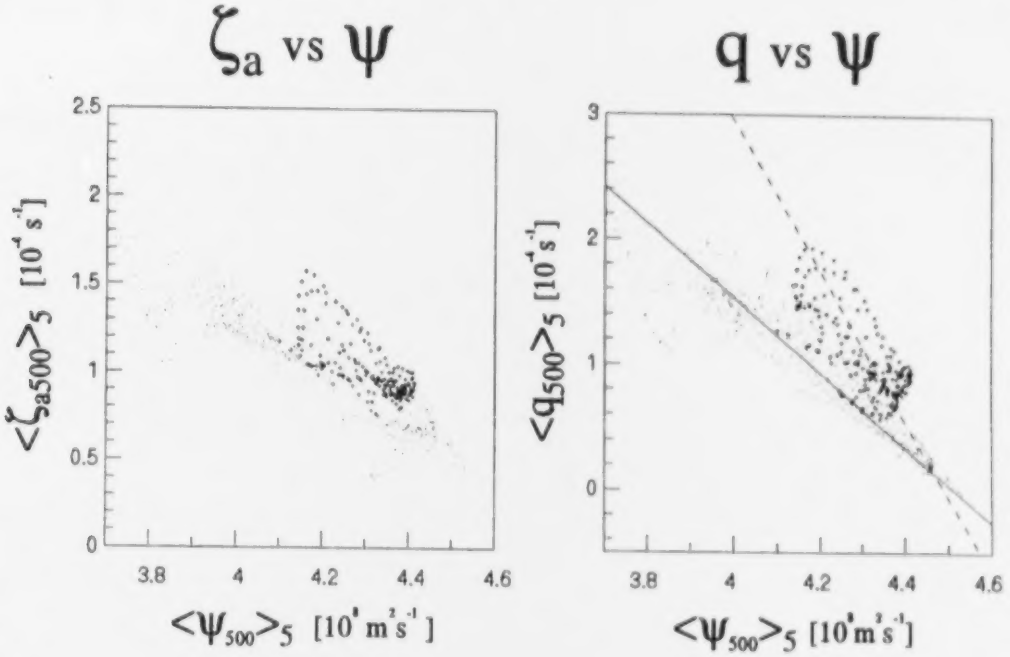
ζa vs ψ
q vs ψ
<ζa500>5 [10-4 s-1]
<q500>5 [10-4 s-1]
<ψ500>5 [10³ m² s-1]
<ψ500>5 [10³ m² s-1]
2.5
2
1.5
1
0.5
0
3
2
1
0
3.8
4
4.2
4.4
4.6

February 4

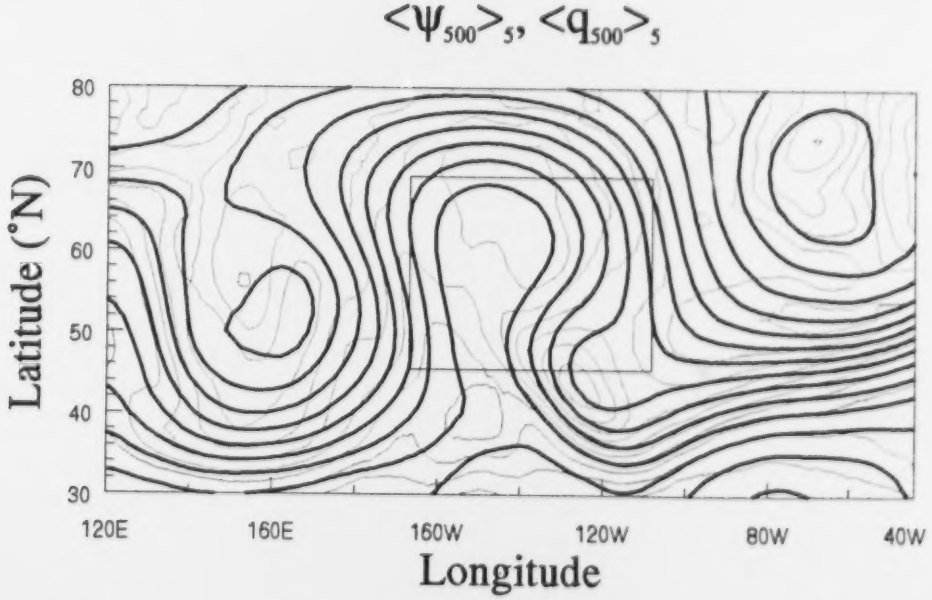
<ψ500>5, <q500>5
Latitude (°N)
80
70
60
50
40
30
120E
160E
160W
120W
80W
40W
Longitude

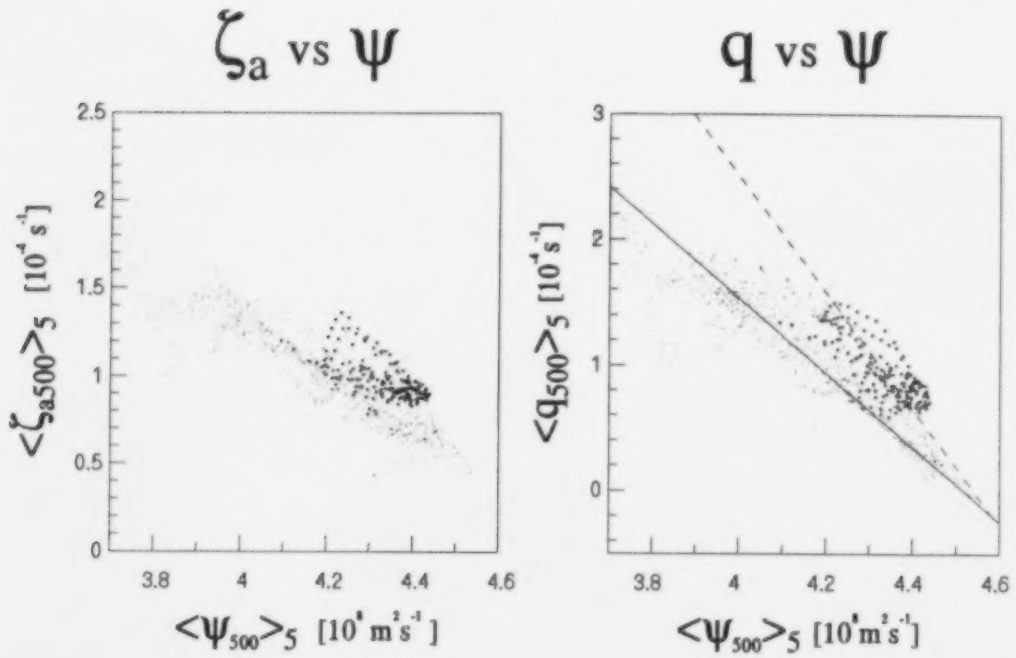
ζa vs ψ
q vs ψ
<ζa500>5 [10⁻⁴ s⁻¹]
<q500>5 [10⁻⁴ s⁻¹]
<ψ500>5 [10⁶ m² s⁻¹]
<ψ500>5 [10⁶ m² s⁻¹]
2.5
2
1.5
1
0.5
0
3
2
1
0
3.8
4
4.2
4.4
4.6

February 5

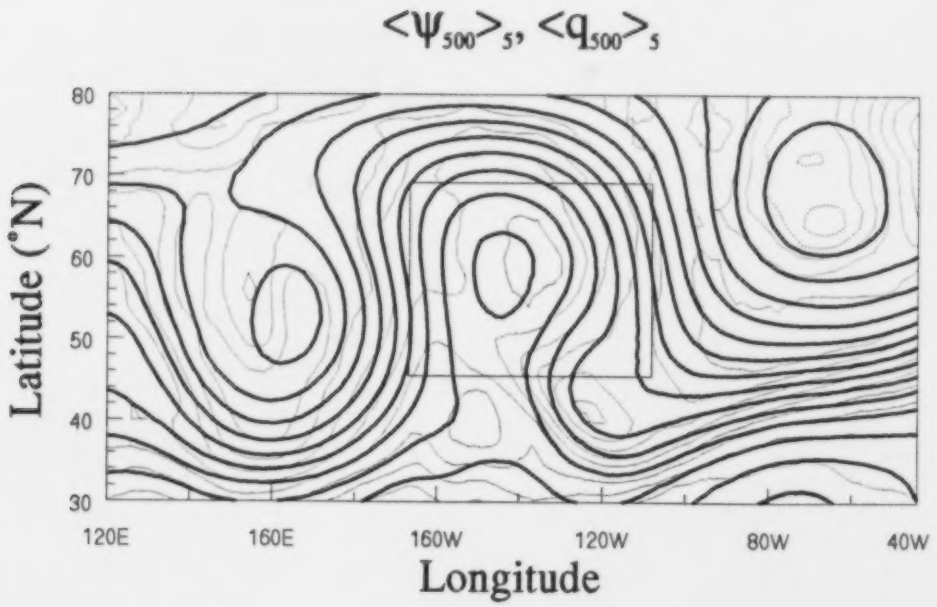
<ψ500>5, <q500>5
Latitude (°N)
80
70
60
50
40
30
120E
160E
160W
120W
80W
40W
Longitude

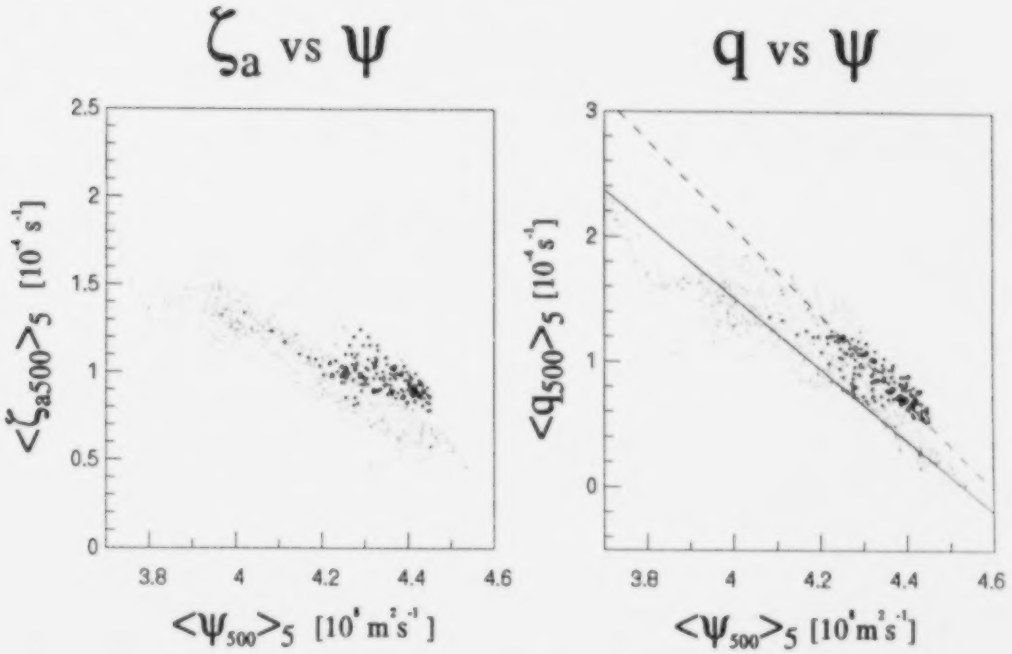
ζa vs ψ
q vs ψ
<ζa500>5 [10⁻⁴ s⁻¹]
<q500>5 [10⁻⁴ s⁻¹]
<ψ500>5 [10⁷ m² s⁻¹]
<ψ500>5 [10⁷ m² s⁻¹]
2.5
2
1.5
1
0.5
0
3
2
1
0
3.8
4
4.2
4.4
4.6

February 6

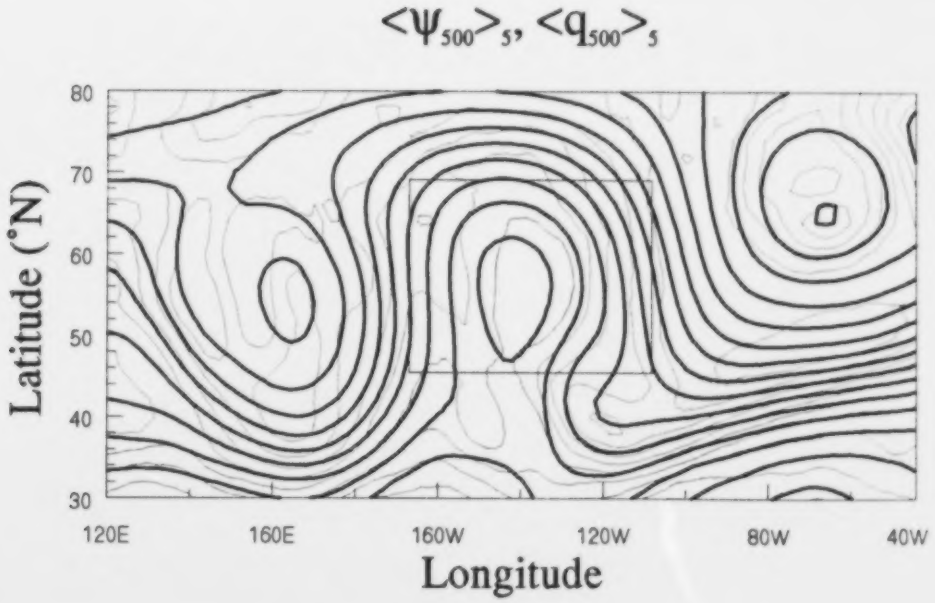
<ψ500>5, <q500>5
Latitude (°N)
80
70
60
50
40
30
120E
160E
160W
120W
80W
40W
Longitude

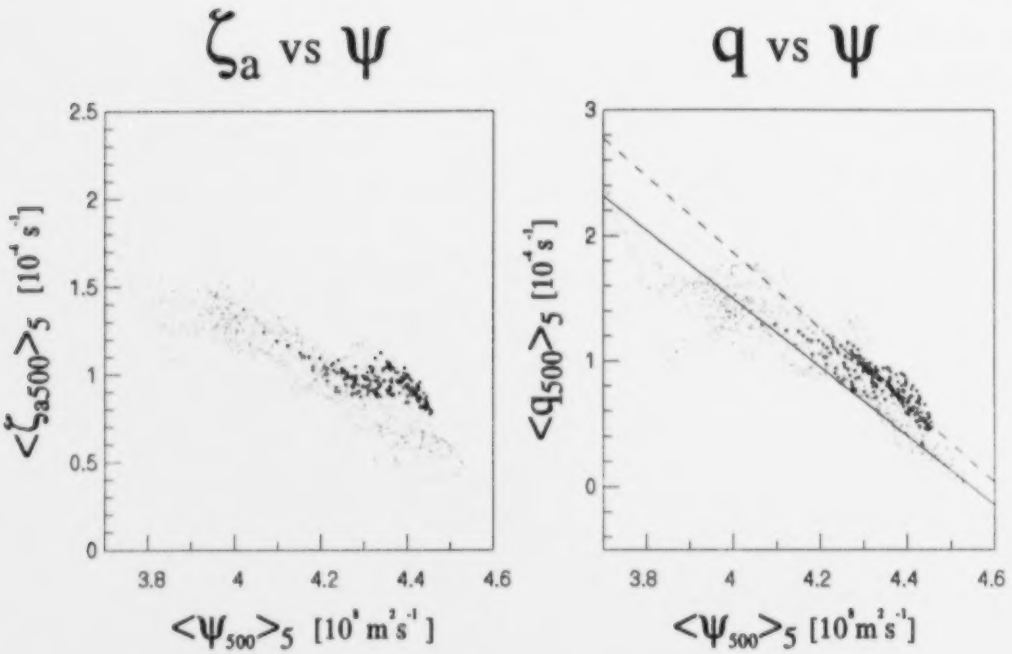
ζa vs ψ
q vs ψ
<ζa500>5 [10-4 s-1]
<q500>5 [10-4 s-1]
<ψ500>5 [10³ m² s-1]
<ψ500>5 [10³ m² s-1]
2.5
2
1.5
1
0.5
0
3
2
1
0
3.8
4
4.2
4.4
4.6

February 7

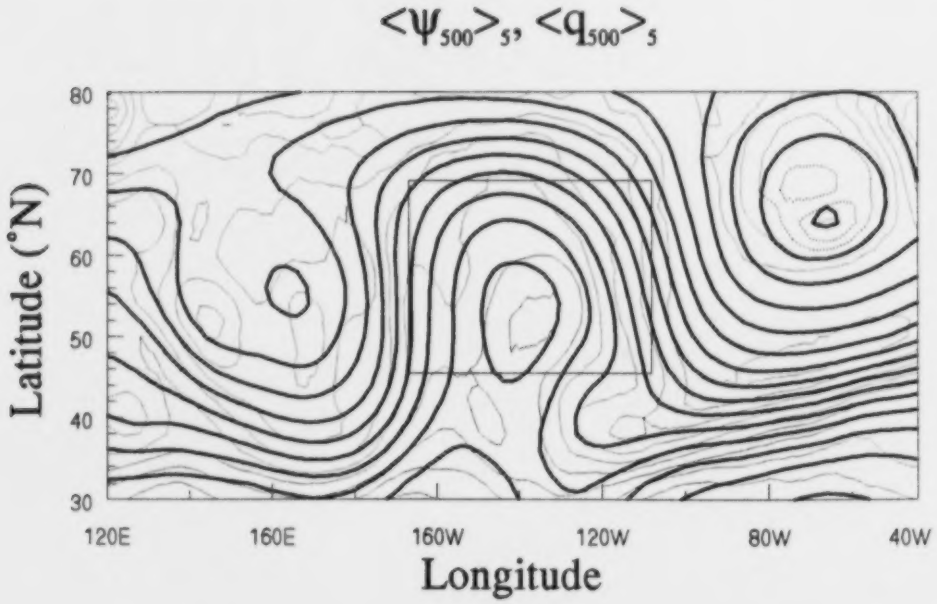
<ψ500>5, <q500>5
Latitude (°N)
80
70
60
50
40
30
120E
160E
160W
120W
80W
40W
Longitude

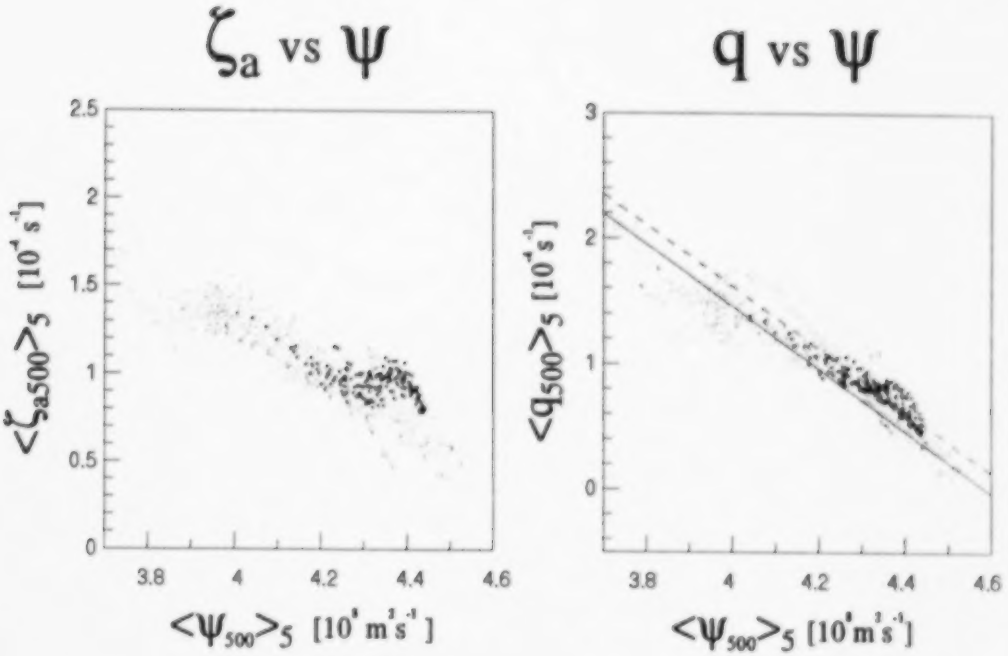
ζa vs ψ
q vs ψ
<ζa500>5 [10⁻⁴ s⁻¹]
<ψ500>5 [10⁴ m² s⁻¹]
<q500>5 [10⁻⁴ s⁻¹]
<ψ500>5 [10⁴ m² s⁻¹]

February 8

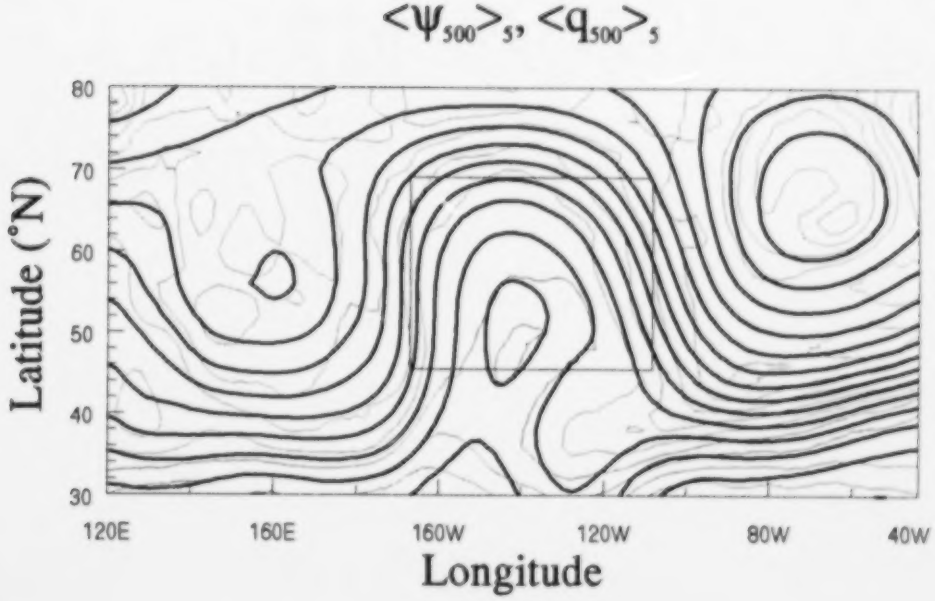
<ψ500>5, <q500>5
Latitude (°N)
Longitude
120E
160E
160W
120W
80W
40W

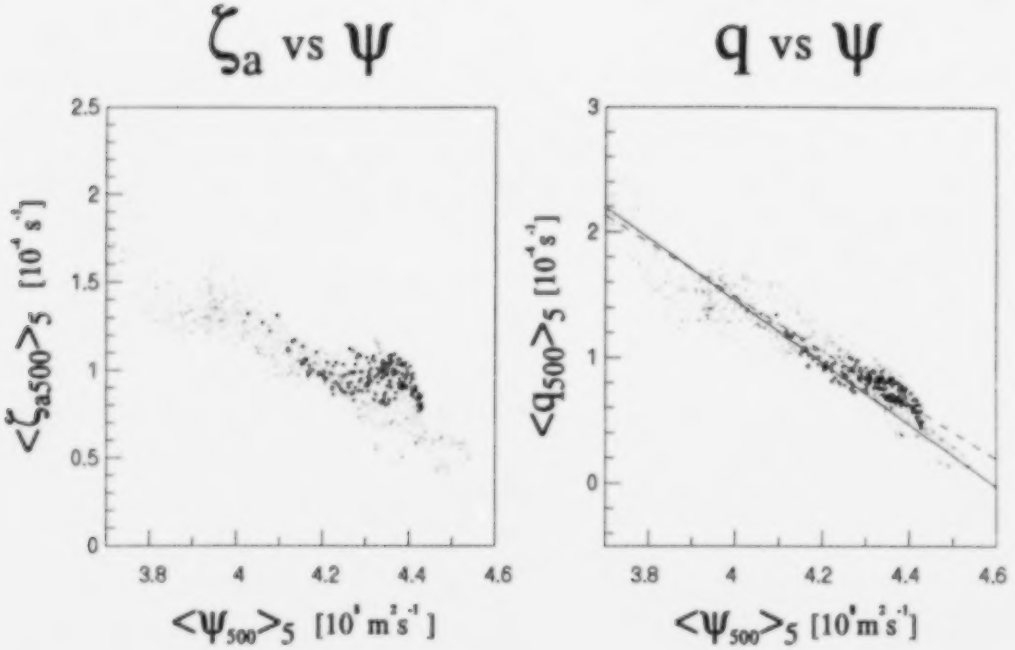
ζa vs ψ
q vs ψ
<ζa500>5 [10⁻⁴s⁻¹]
<q500>5 [10⁻⁴s⁻¹]
<ψ500>5 [10⁶m²s⁻¹]
<ψ500>5 [10⁶m²s⁻¹]
2.5
2
1.5
1
0.5
0
3
2
1
0
3.8
4
4.2
4.4
4.6

February 9

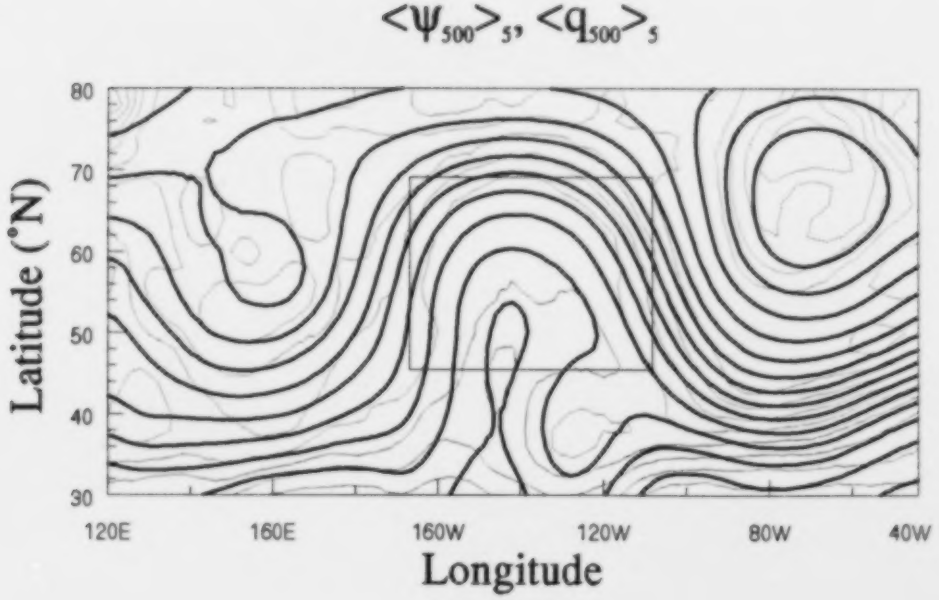
<ψ500>5, <q500>5
Latitude (°N)
80
70
60
50
40
30
120E
160E
160W
120W
80W
40W
Longitude

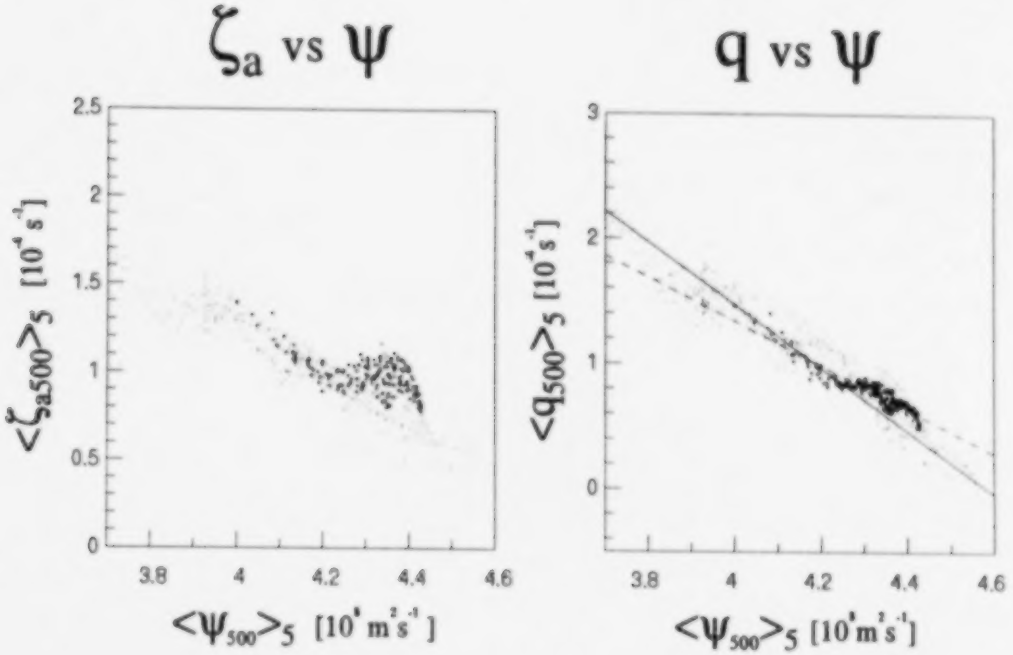
ζa vs ψ
q vs ψ
<ζa500>5 [10⁻⁵s⁻¹]
<q500>5 [10⁻⁵s⁻¹]
<ψ500>5 [10³m²s⁻¹]
<ψ500>5 [10³m²s⁻¹]
2.5
2
1.5
1
0.5
0
3
2
1
0
3.8
4
4.2
4.4
4.6

February 10

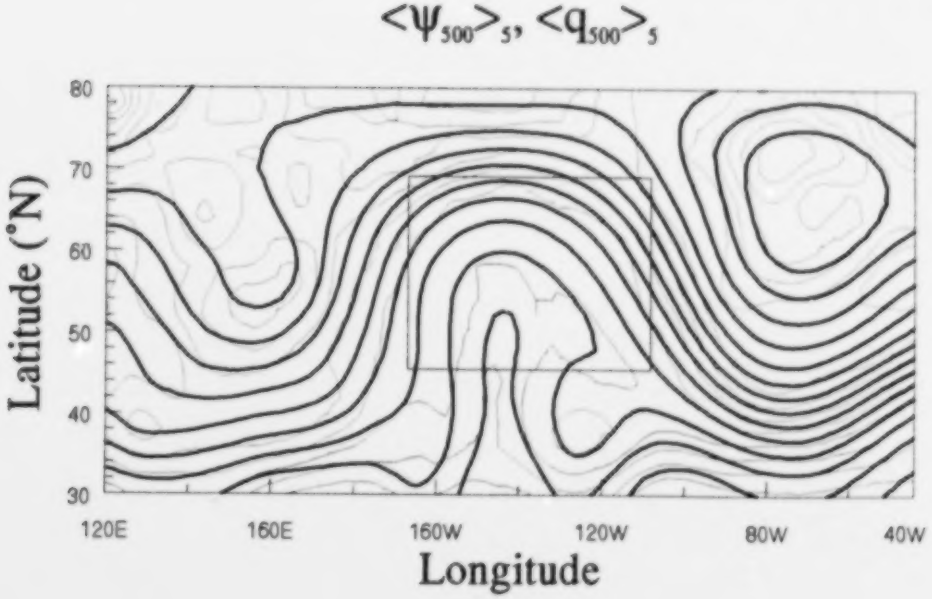
<ψ500>5, <q500>5
Latitude (°N)
80
70
60
50
40
30
120E
160E
160W
120W
80W
40W
Longitude

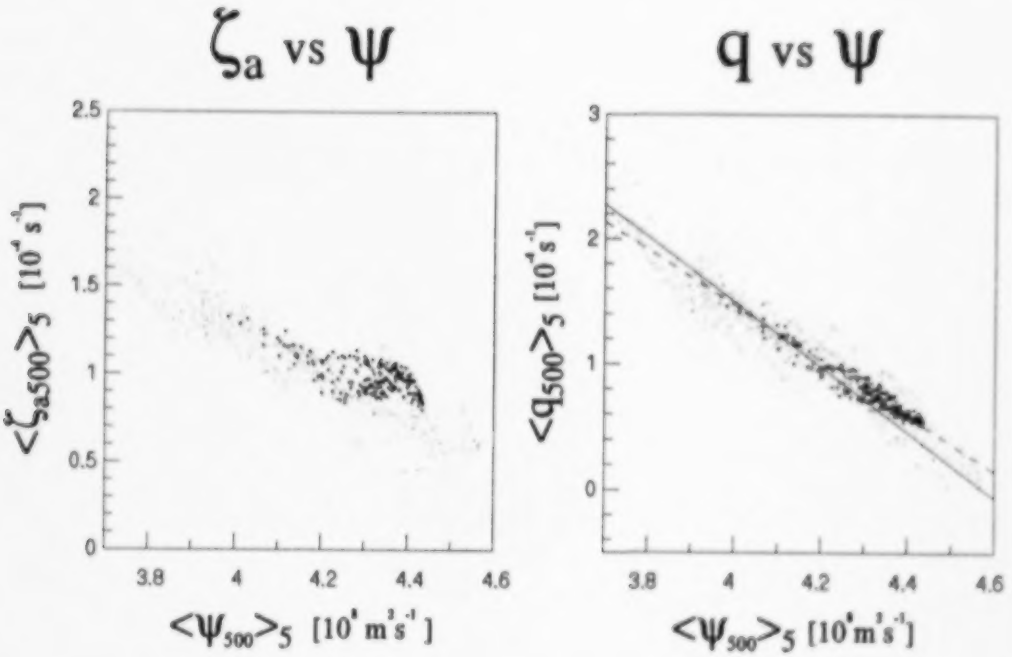
ζa vs ψ
q vs ψ
<ζa500>5 [10⁻⁶ s⁻¹]
<ψ500>5 [10³ m²s⁻¹]
<q500>5 [10⁻¹⁰ s⁻¹]
<ψ500>5 [10³m²s⁻¹]

February 11

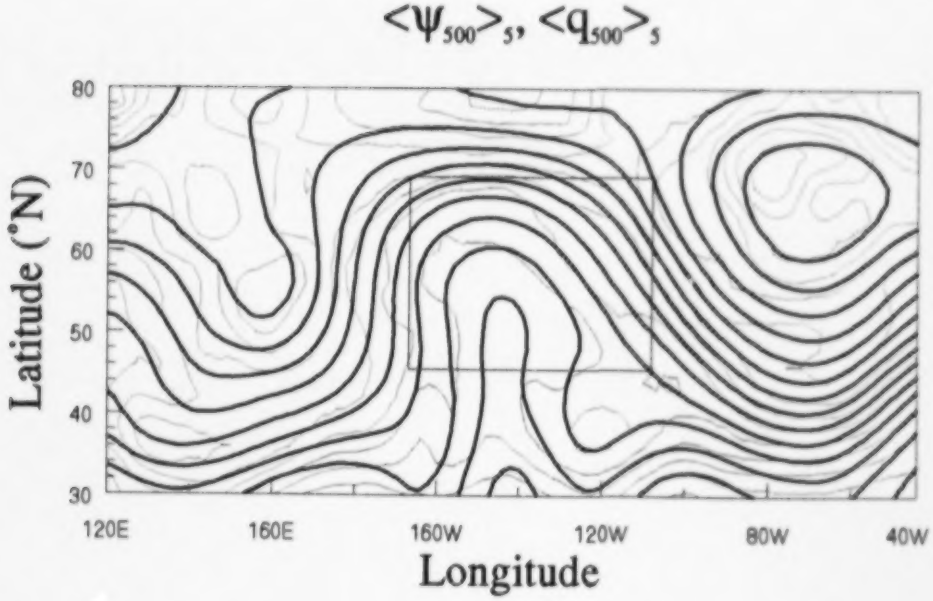
<ψ500>5, <q500>5
Latitude (°N)
Longitude
120E
160E
160W
120W
80W
40W

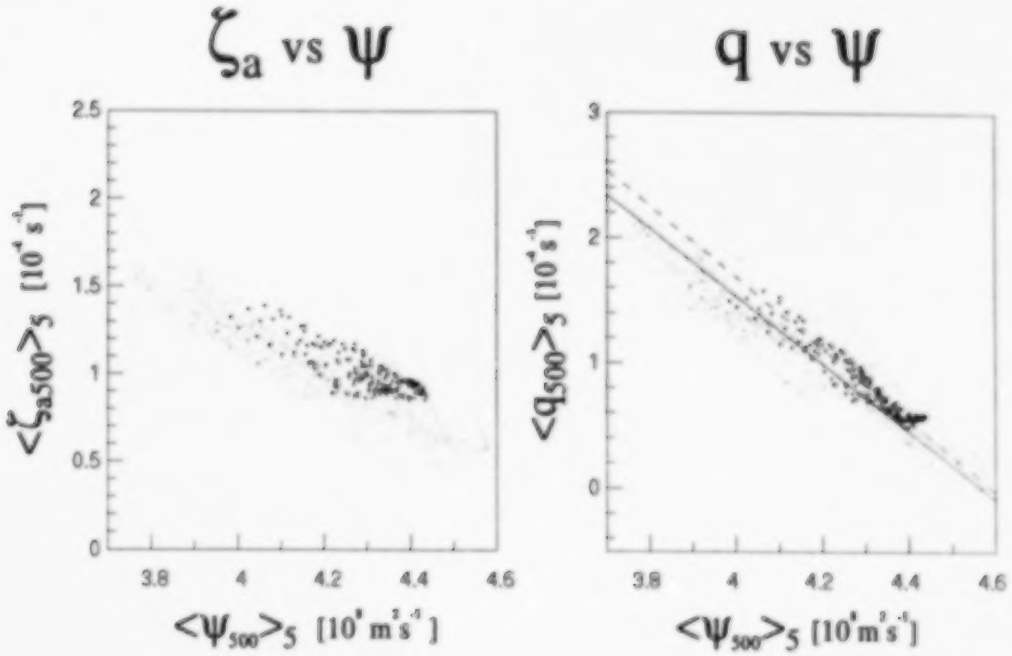
ζa vs ψ
q vs ψ
<ζa500>5 [10⁻⁵s⁻¹]
<q500>5 [10⁻⁵s⁻¹]
<ψ500>5 [10⁶m²s⁻¹]
<ψ500>5 [10⁶m²s⁻¹]

February 12

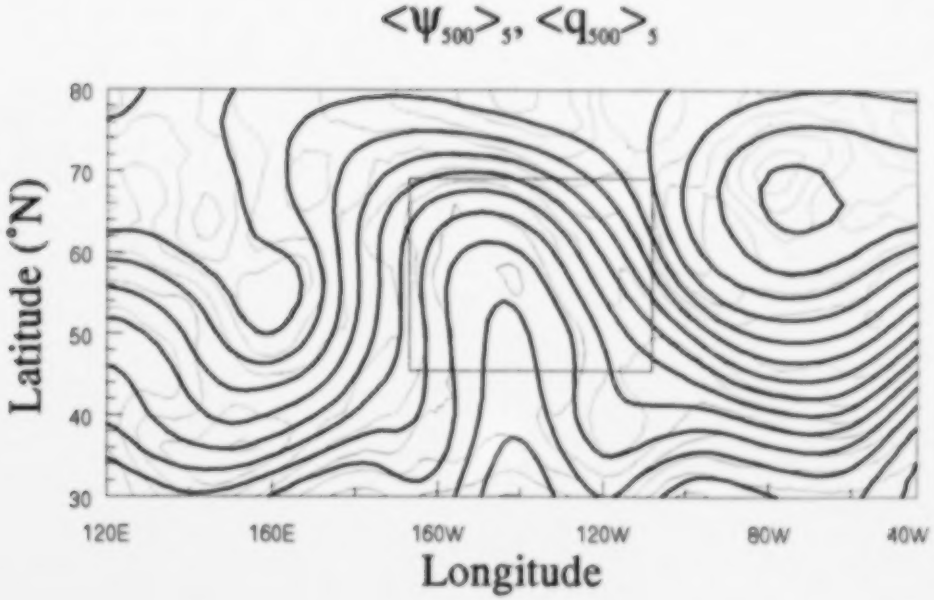
<ψ500>5, <q500>5
Latitude (°N)
Longitude
120E
160E
160W
120W
80W
40W

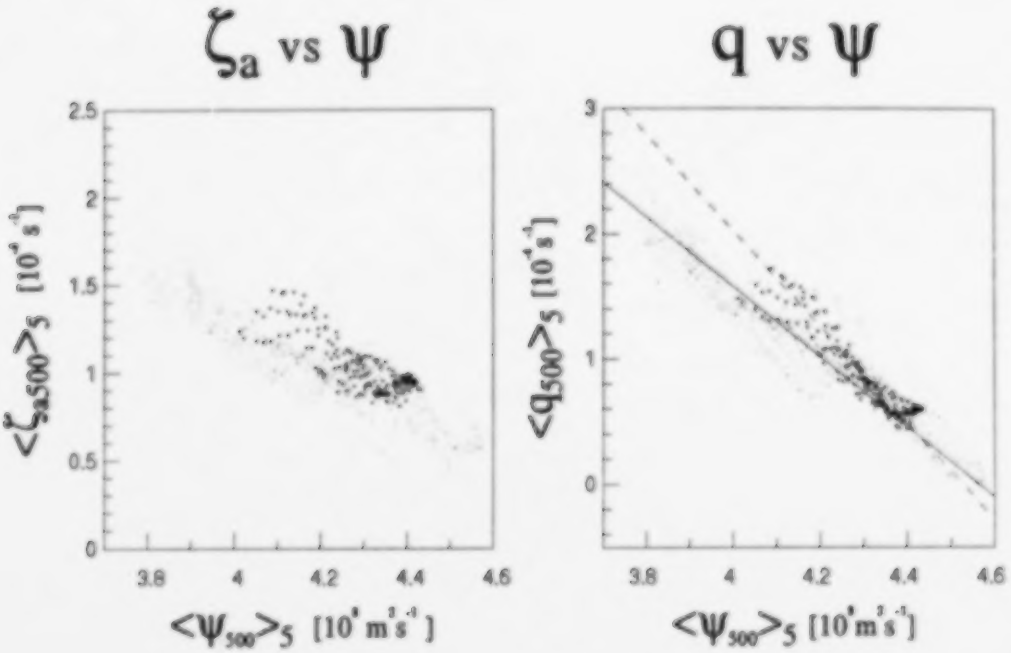
ζa vs ψ
q vs ψ
<ζa500>5 [10⁻⁵s⁻¹]
<q500>5 [10⁻⁵s⁻¹]
<ψ500>5 [10⁶m²s⁻¹]
<ψ500>5 [10⁶m²s⁻¹]

February 13

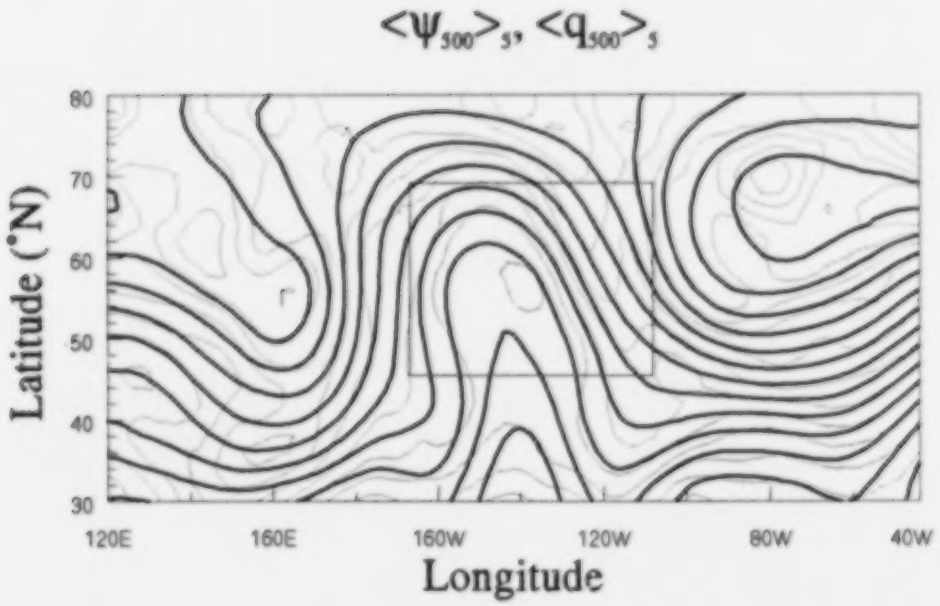
<ψ500>5, <q500>5
Latitude (°N)
Longitude
120E
160E
160W
120W
80W
40W

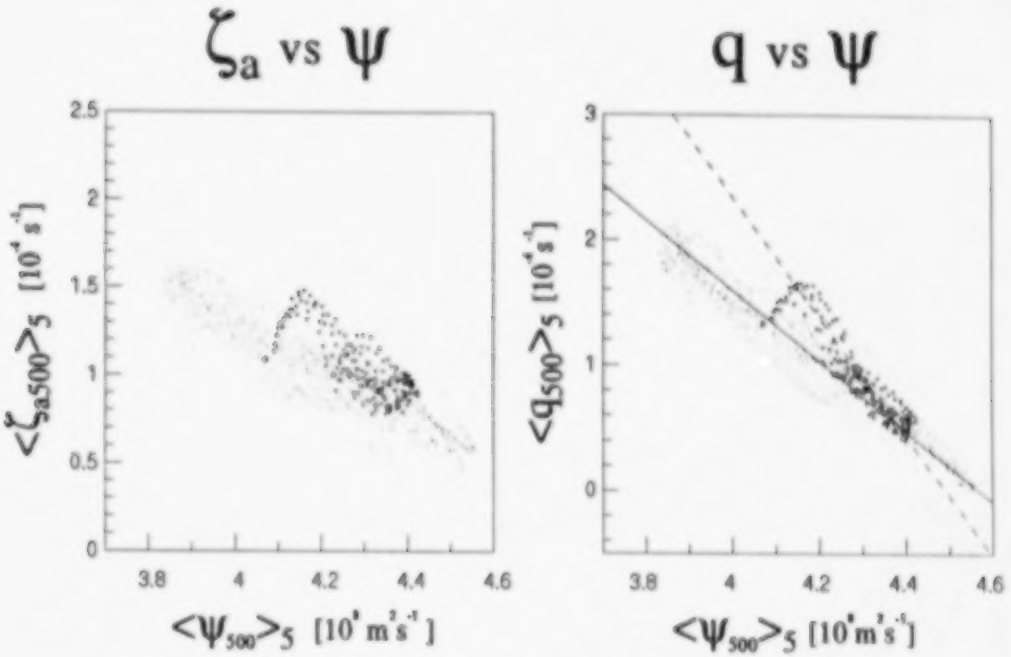
ζa vs ψ
q vs ψ
<ζa500>5 [10⁻⁵ s⁻¹]
<q500>5 [10⁻⁵ s⁻¹]
<ψ500>5 [10⁶ m²s⁻²]
<ψ500>5 [10⁶ m²s⁻²]
2.5
2
1.5
1
0.5
0
3
2
1
0
3.8
4
4.2
4.4
4.6

February 14

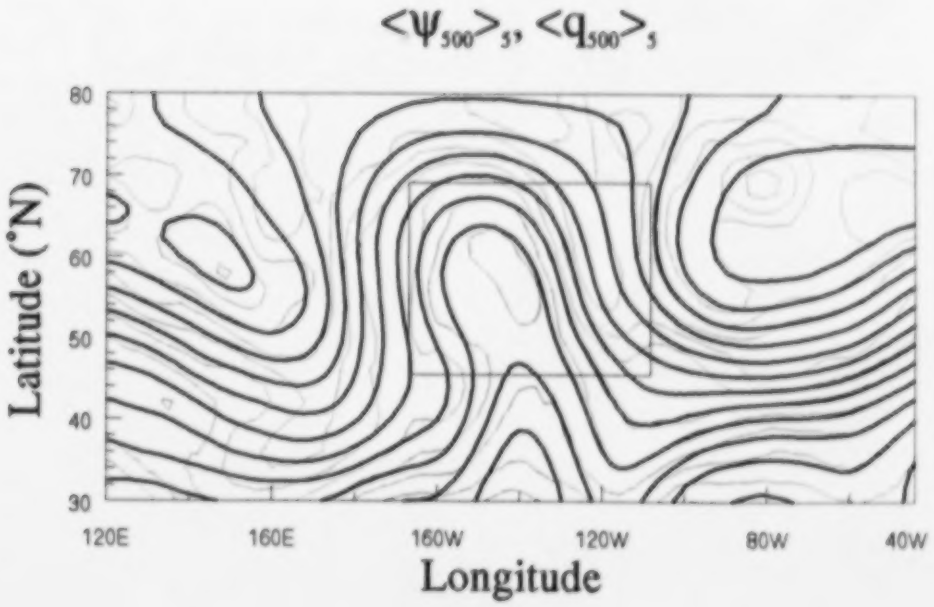
<ψ500>5, <q500>5
Latitude (°N)
80
70
60
50
40
30
120E
160E
160W
120W
80W
40W
Longitude

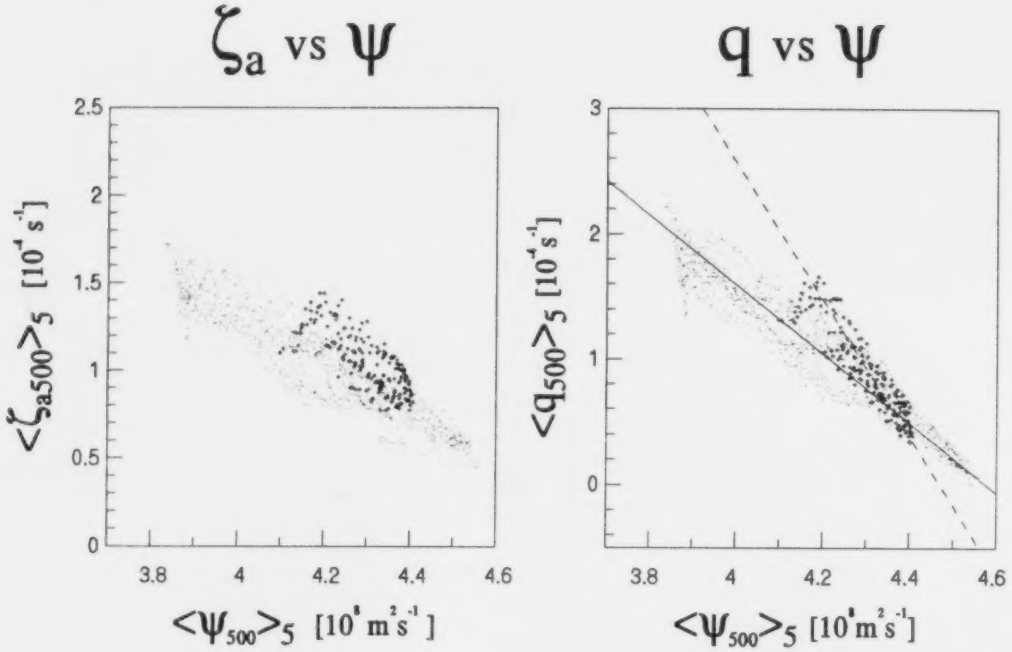
ζa vs ψ
q vs ψ
<ζa500>5 [10-4 s-1]
<q500>5 [10-4 s-1]
<ψ500>5 [10³ m² s-1]
<ψ500>5 [10³ m² s-1]
2.5
2
1.5
1
0.5
0
3
2
1
0
3.8
4
4.2
4.4
4.6

February 15

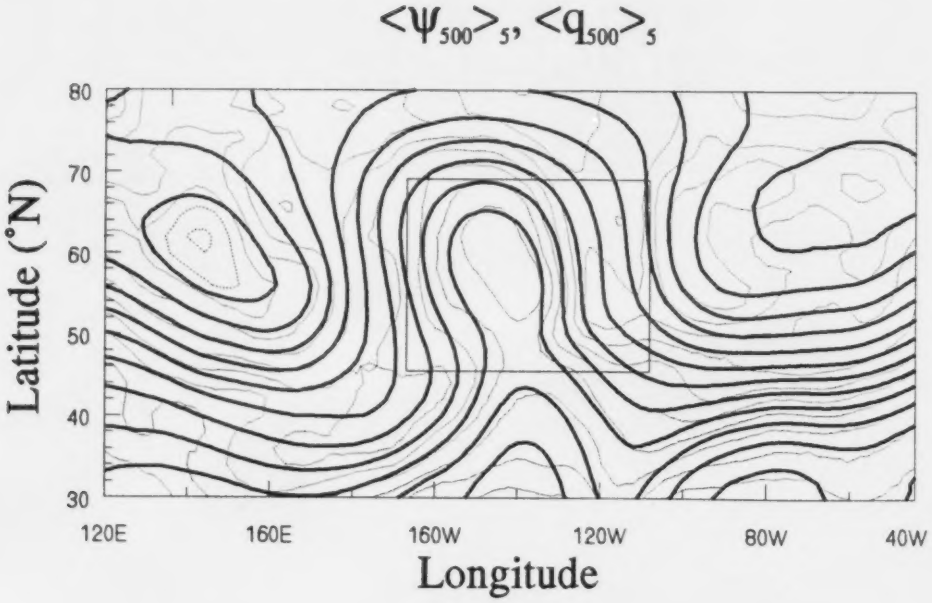
<ψ500>5, <q500>5
Latitude (°N)
80
70
60
50
40
30
120E
160E
160W
120W
80W
40W
Longitude

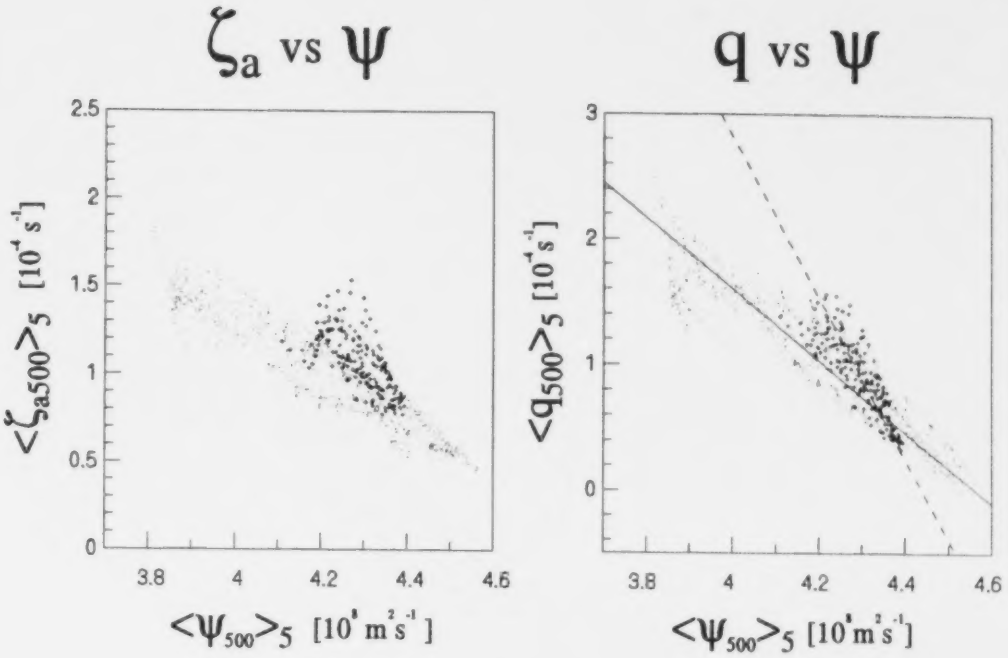
ζa vs ψ
q vs ψ
<ζa500>5 [10-4 s-1]
<q500>5 [10-4 s-1]
<ψ500>5 [10⁸ m² s-1]
<ψ500>5 [10⁸ m² s-1]
2.5
2
1.5
1
0.5
0
3
2
1
0
3.8
4
4.2
4.4
4.6

February 16

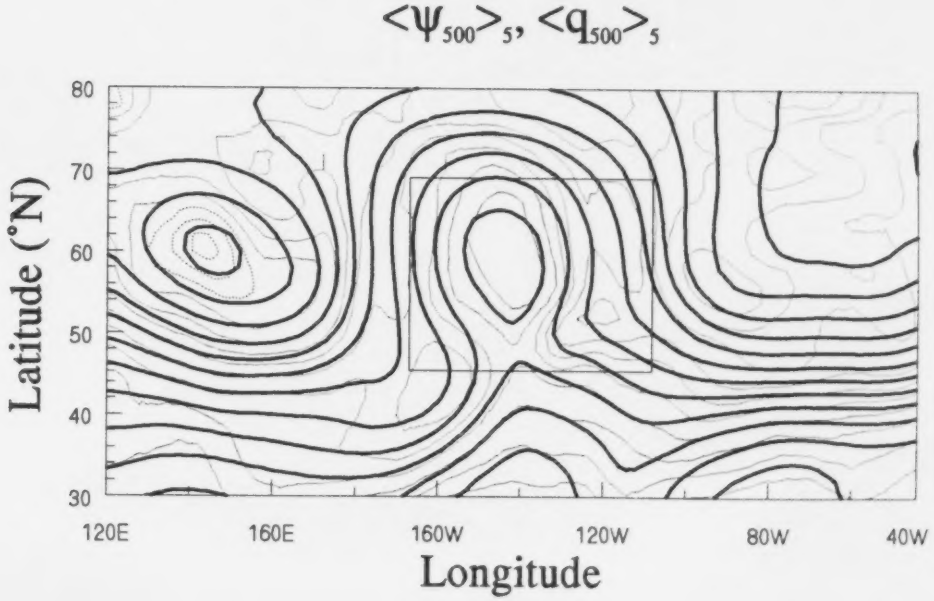
<ψ500>5, <q500>5
Latitude (°N)
80
70
60
50
40
30
120E
160E
160W
120W
80W
40W
Longitude

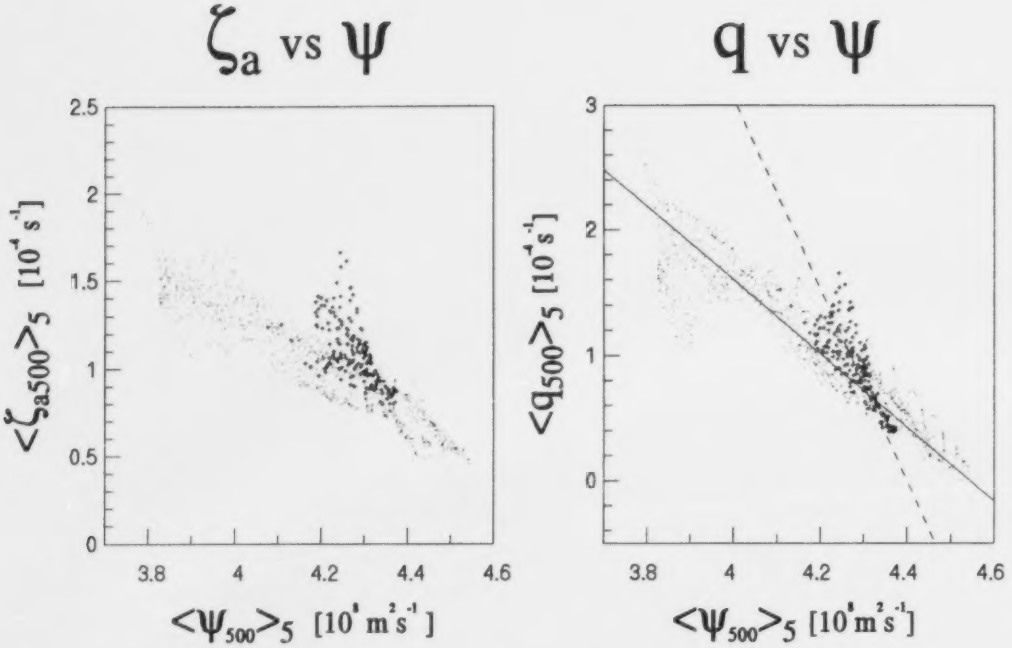
ζa vs ψ
q vs ψ
<ζa500>5 [10-4 s-1]
<q500>5 [10-4 s-1]
<ψ500>5 [10⁶ m²s-1]
<ψ500>5 [10⁶ m²s-1]
2.5
2
1.5
1
0.5
0
3
2
1
0
3.8
4
4.2
4.4
4.6

February 17

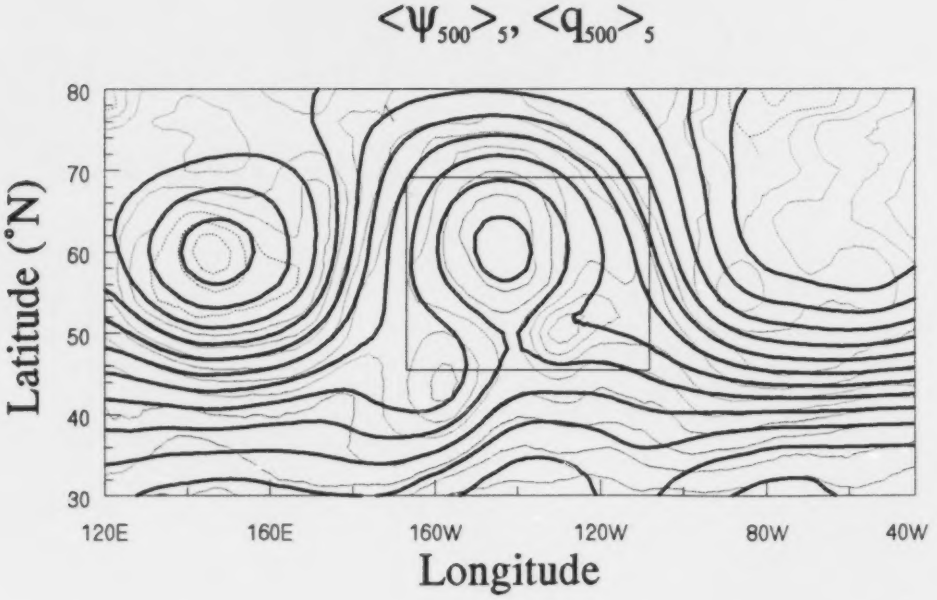
<ψ500>5, <q500>5
Latitude (°N)
80
70
60
50
40
30
120E
160E
160W
120W
80W
40W
Longitude

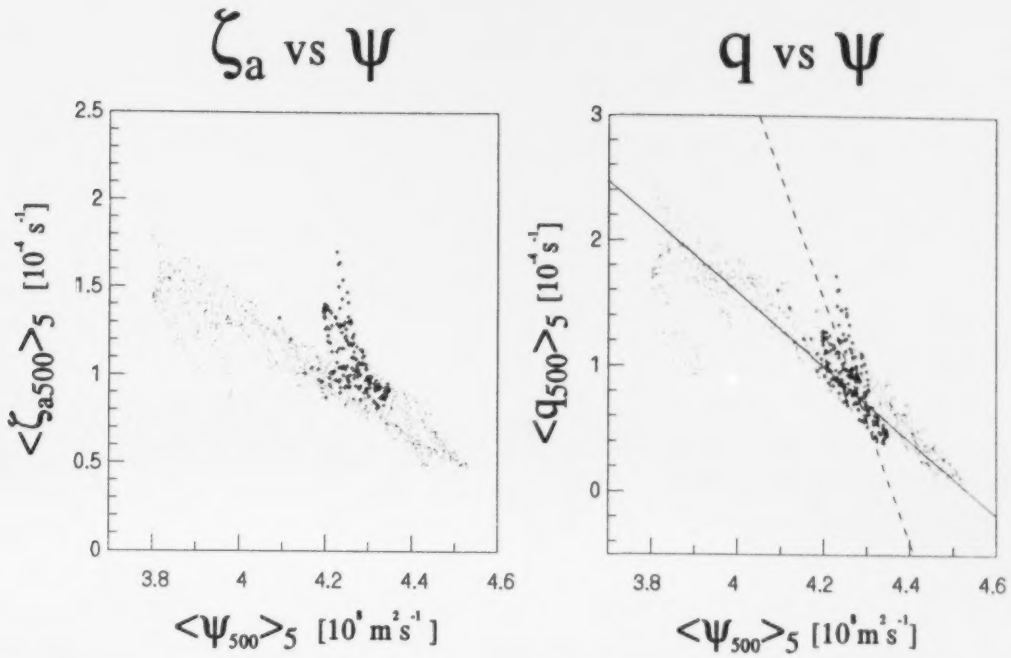
ζa vs ψ
q vs ψ
<ζa500>5 [10-4 s-1]
<q500>5 [10-4 s-1]
<ψ500>5 [10' m2s-1]
<ψ500>5 [10' m2s-1]
2.5
2
1.5
1
0.5
0
3
2
1
0
3.8
4
4.2
4.4
4.6

February 18

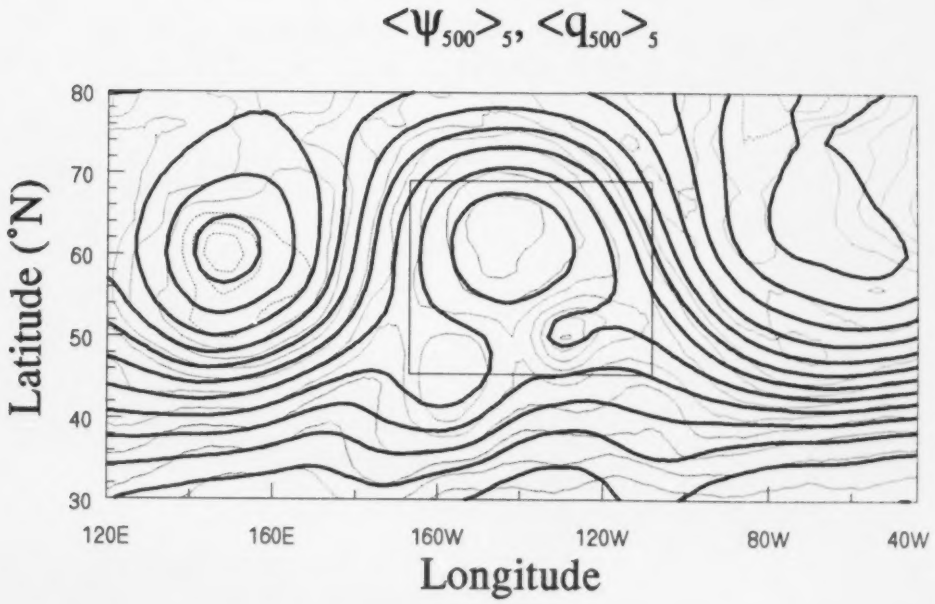
<ψ500>5, <q500>5
Latitude (°N)
80
70
60
50
40
30
120E
160E
160W
120W
80W
40W
Longitude

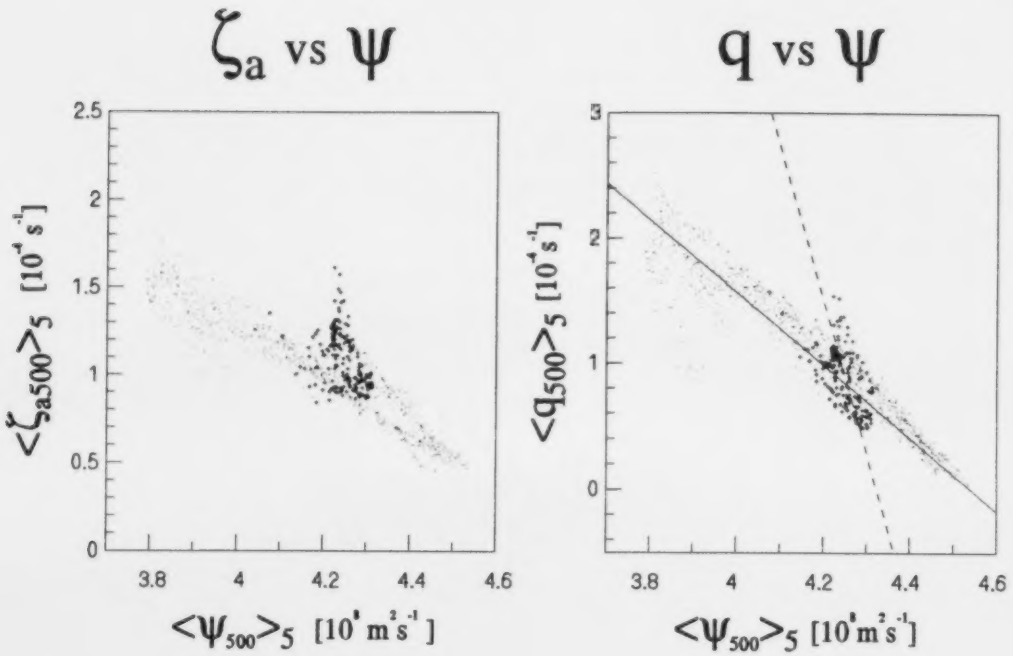
ζa vs ψ
q vs ψ
<ζa500>5 [10⁻⁵ s⁻¹]
<ψ500>5 [10⁵ m² s⁻¹]
<q500>5 [10⁻¹¹ m⁻¹ s⁻¹]
2.5
2
1.5
1
0.5
0
3
3.8
4
4.2
4.4
4.6

February 19

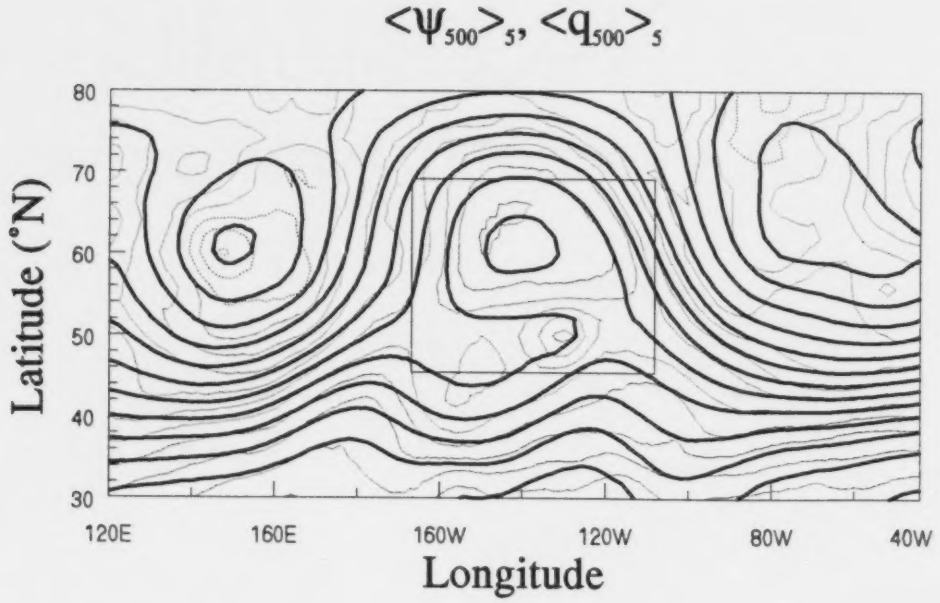
<ψ500>5, <q500>5
Latitude (°N)
80
70
60
50
40
30
120E
160E
160W
120W
80W
40W
Longitude

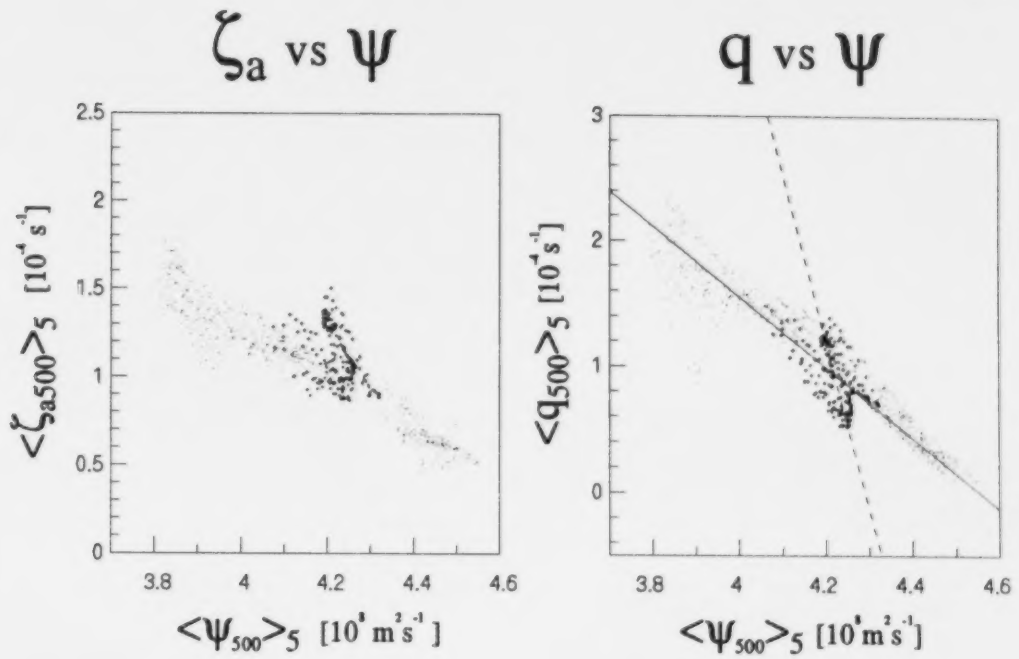
ζa vs ψ
q vs ψ
<ζa500>5 [10-4 s-1]
<q500>5 [10-4 s-1]
<ψ500>5 [10³ m² s-1]
<ψ500>5 [10³ m² s-1]
2.5
2
1.5
1
0.5
0
3
2
1
0
3.8
4
4.2
4.4
4.6

February 20

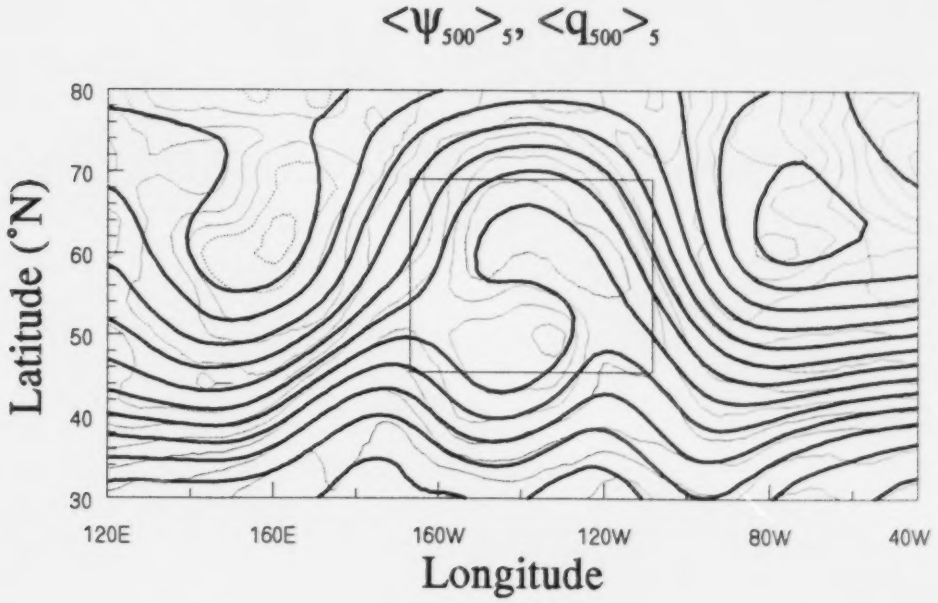
<ψ500>5, <q500>5
Latitude (°N)
80
70
60
50
40
30
120E
160E
160W
120W
80W
40W
Longitude

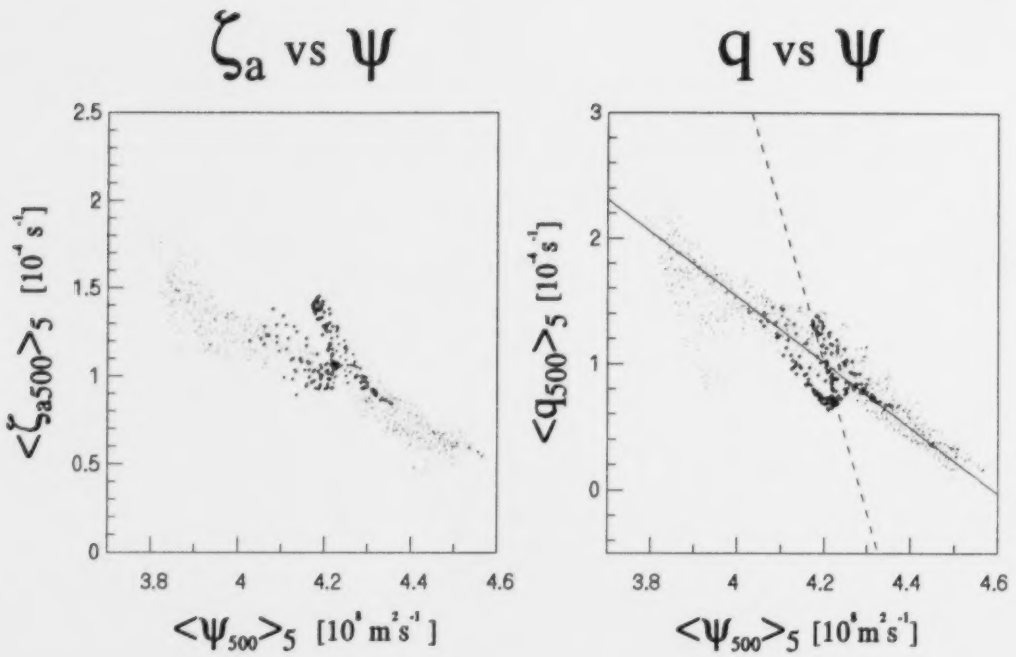
ζa vs ψ
q vs ψ
<ζa500>5 [10-4 s-1]
<q500>5 [10-4 s-1]
<ψ500>5 [10⁶ m²s-1]
<ψ500>5 [10⁶m²s-1]
2.5
2
1.5
1
0.5
0
3
2
1
0
3.8
4
4.2
4.4
4.6

February 21

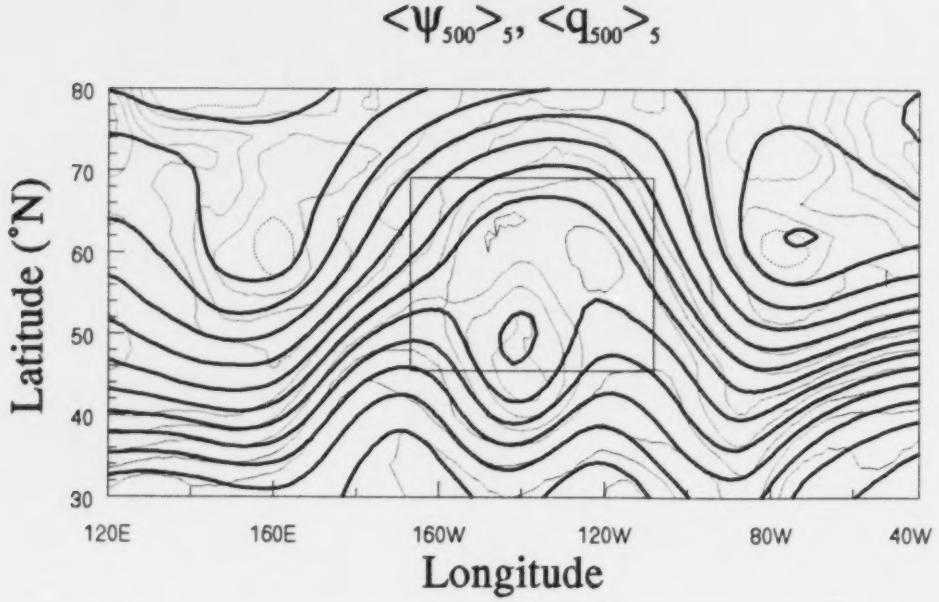
<ψ500>5, <q500>5
Latitude (°N)
80
70
60
50
40
30
120E
160E
160W
120W
80W
40W
Longitude

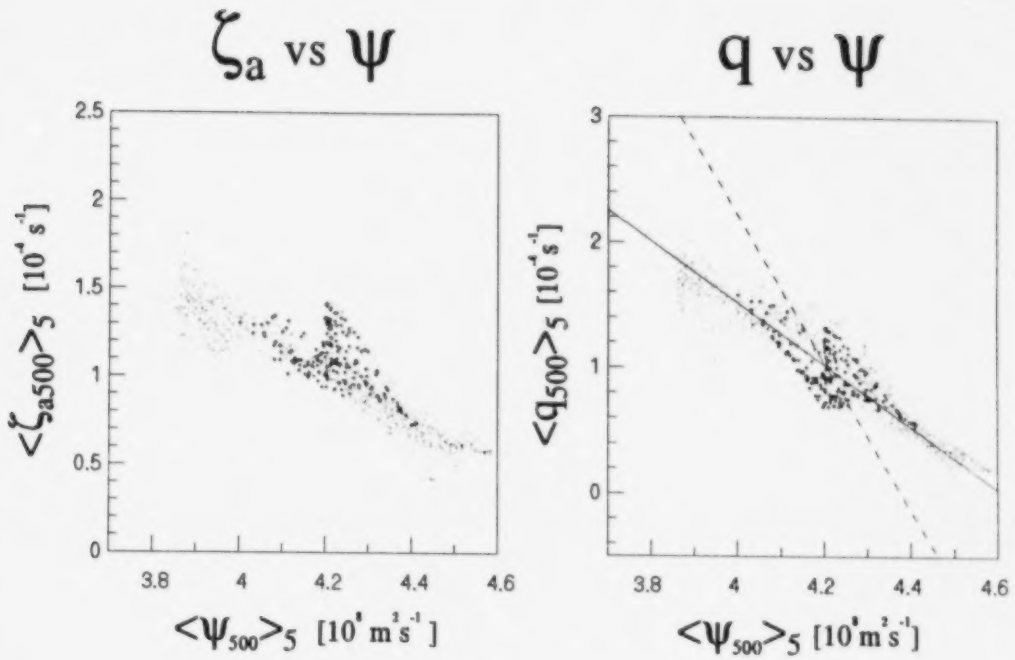
ζa vs ψ
q vs ψ
<ζa500>5 [10⁻⁴ s⁻¹]
<q500>5 [10⁻⁴ s⁻¹]
<ψ500>5 [10⁶ m² s⁻¹]
<ψ500>5 [10⁶ m² s⁻¹]

February 22

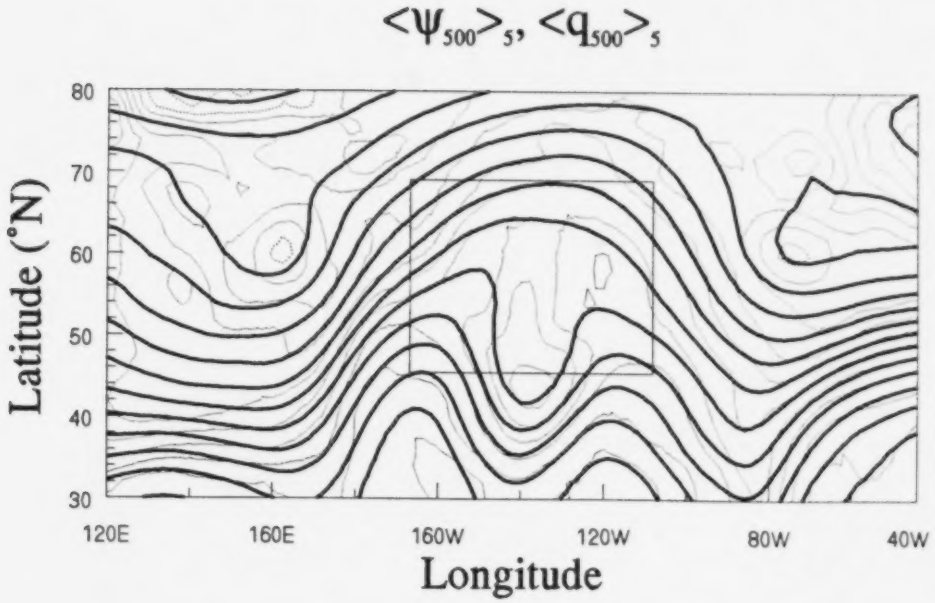
<ψ500>5, <q500>5
Latitude (°N)
Longitude
120E
160E
160W
120W
80W
40W

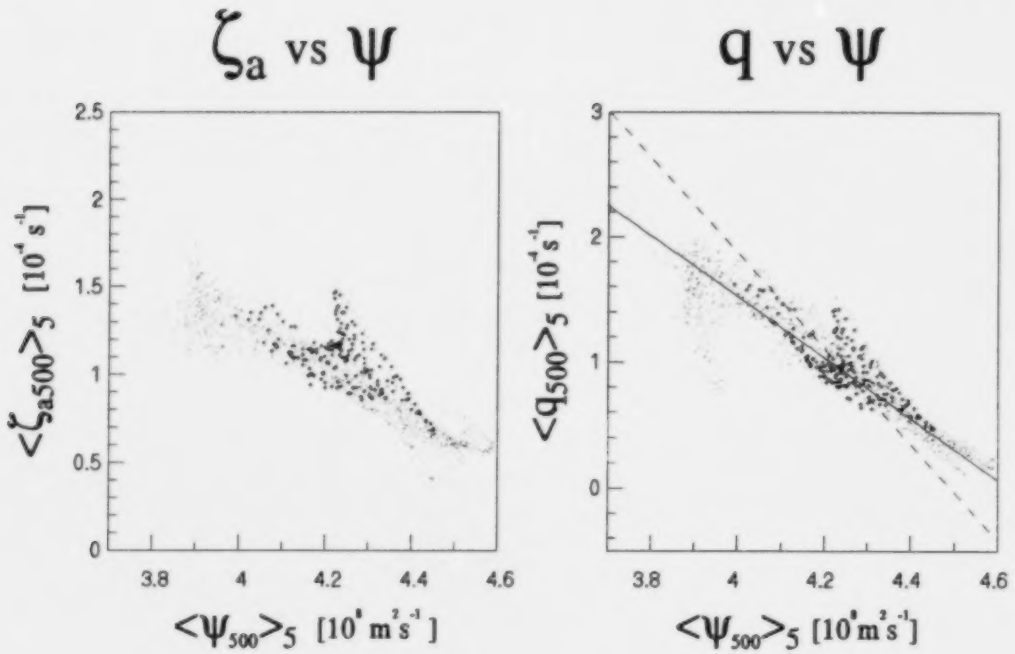
ζa vs ψ
q vs ψ
<ζa500>5 [10-4 s-1]
<q500>5 [10-4 s-1]
<ψ500>5 [10³ m²s-1]
<ψ500>5 [10³m²s-1]
2.5
2
1.5
1
0.5
0
3
2
1
0
3.8
4
4.2
4.4
4.6

February 23

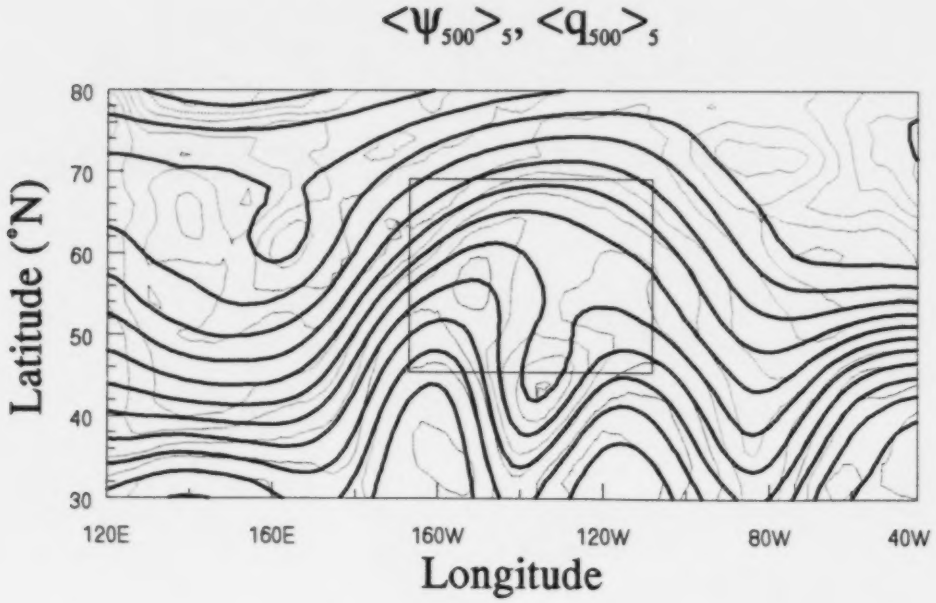
<ψ500>5, <q500>5
Latitude (°N)
80
70
60
50
40
30
120E
160E
160W
120W
80W
40W
Longitude

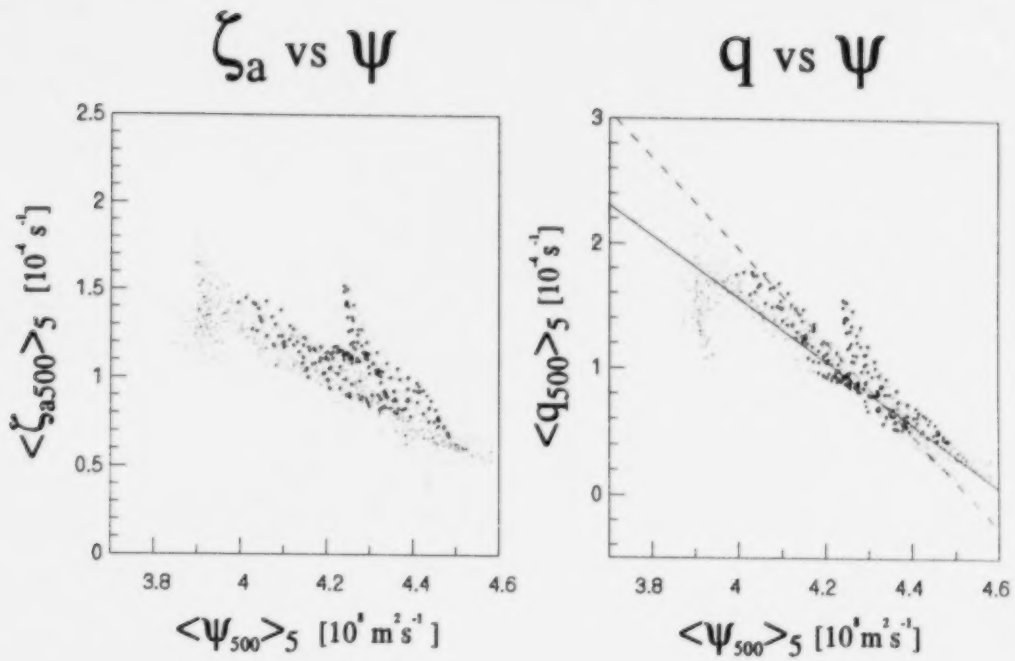
ζa vs ψ
q vs ψ
<ζa500>5 [10-4 s-1]
<q500>5 [10-4 s-1]
<ψ500>5 [10³ m² s-1]
<ψ500>5 [10³ m² s-1]
2.5
2
1.5
1
0.5
0
3
2
1
0
3.8
4
4.2
4.4
4.6

February 24

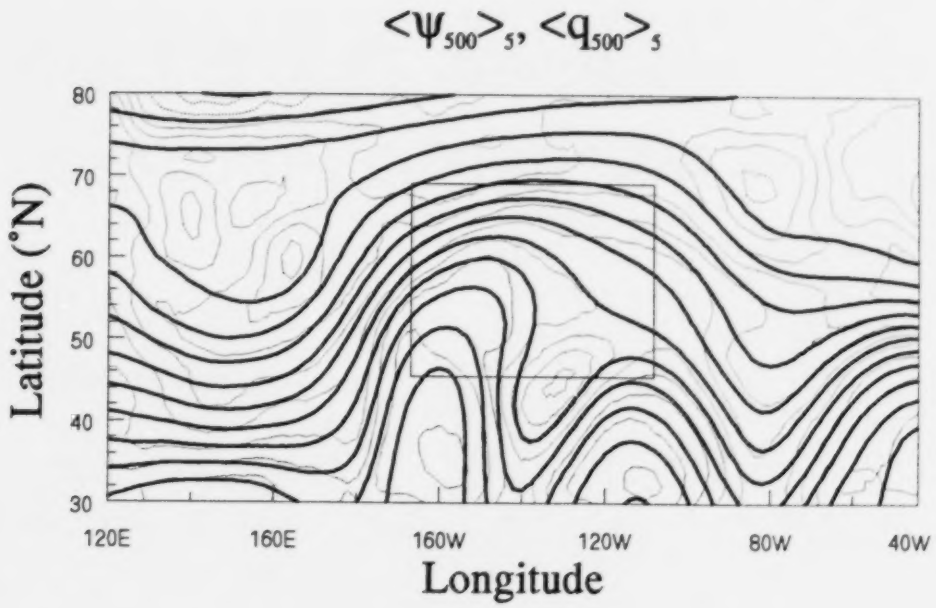
<ψ500>5, <q500>5
Latitude (°N)
80
70
60
50
40
30
120E
160E
160W
120W
80W
40W
Longitude

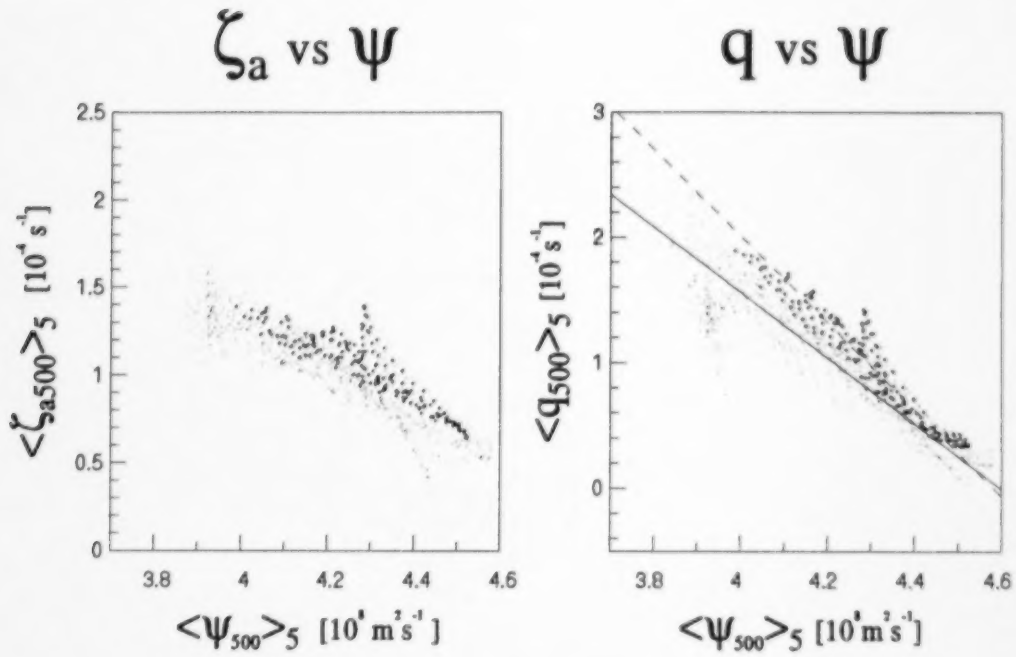
ζ_a vs ψ
q vs ψ
$<\zeta_{a500}>_5$ [10^{-5} s^{-1}]
$<q_{500}>_5$ [10^{-11} s^{-1}]
$<\psi_{500}>_5$ [10^3 m^2 s^{-1}]
$<\psi_{500}>_5$ [10^3 m^2 s^{-1}]

February 25

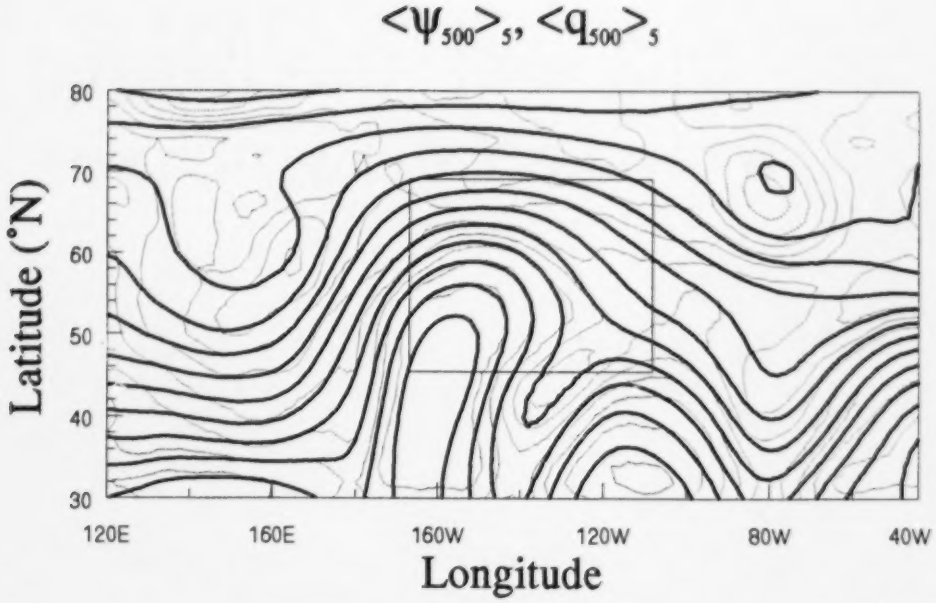
$<\psi_{500}>_5$, $<q_{500}>_5$
Latitude (°N)
Longitude
120E
160E
160W
120W
80W
40W

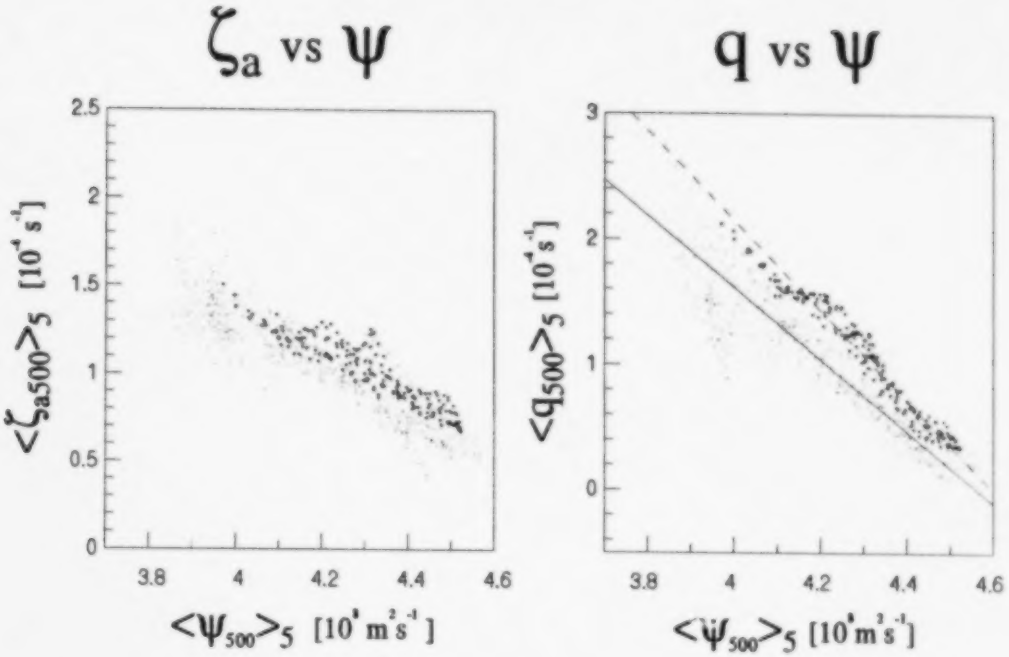
ζa vs ψ
q vs ψ
<ζa500>5 [10⁻⁴ s⁻¹]
<ψ500>5 [10⁶ m²s⁻¹]
<q500>5 [10⁻⁴ s⁻¹]
<ψ500>5 [10⁶m²s⁻¹]

February 26

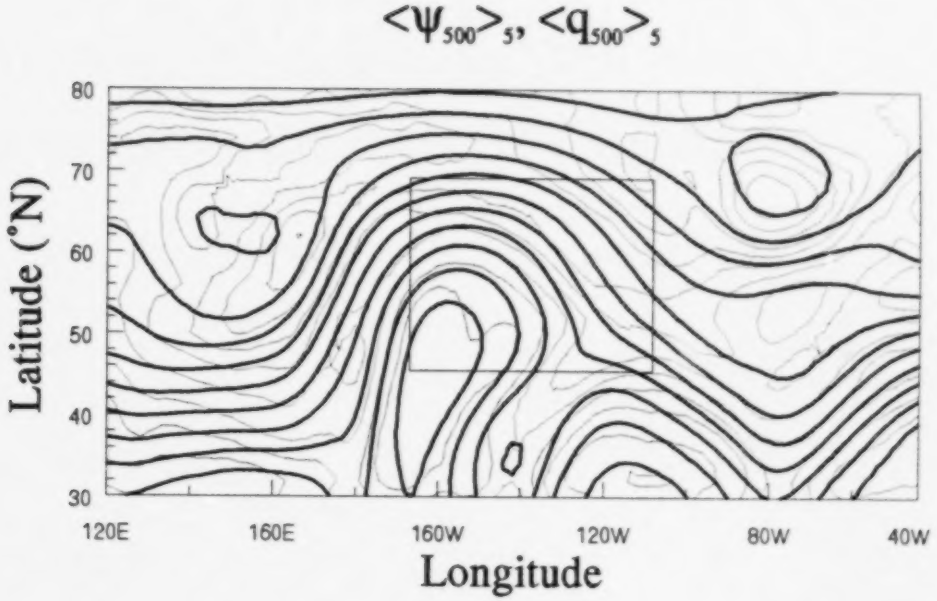
<ψ500>5, <q500>5
Latitude (°N)
Longitude
120E
160E
160W
120W
80W
40W